



Title	High-Pressure Synthesis, Crystal Structures, and Magnetic Properties of Perovskite-Related Os and Ir Oxides
Author(s)	袁, 亞華
Citation	北海道大学. 博士(理学) 甲第12038号
Issue Date	2015-09-25
DOI	10.14943/doctoral.k12038
Doc URL	http://hdl.handle.net/2115/59990
Type	theses (doctoral)
File Information	Yuan_Yahua.pdf



[Instructions for use](#)

High-Pressure Synthesis, Crystal Structures,
and Magnetic Properties of Perovskite-Related
Os and Ir Oxides

A Thesis

Submitted by

YUAN Yahua

In fulfillment for the award of the degree of

Doctor of Science

Graduate School of Chemical Sciences and Engineering,

Hokkaido University

2015

Abstract

Over the past quarter century, oxides and compound containing $5d$ transition metal ions, *e.g.* Ir and Os, have attracted considerable attention with solid-state physicists because of various unconventional physical phenomena. Due to the competition between localization and itinerancy of d electron, there were a lot of interesting and unusual properties with different crystal structures reported, such as, metal-insulator transitions, topological phases and frustrated magnetism. In this study, we used high pressure method to synthesize the $5d$ oxides and researched their crystal structures and magnetic properties.

$5d$ Solid-state oxides $\text{K}_{0.84}\text{OsO}_3$ ($\text{Os}^{5.16+}$; $5d^{2.84}$) and $\text{Bi}_{2.93}\text{Os}_3\text{O}_{11}$ ($\text{Os}^{4.40+}$; $5d^{3.60}$) were synthesized under high-pressure and high-temperature conditions (6 GPa and 1500-1700 °C). Their crystal structures were determined by synchrotron x-ray diffraction and their $5d$ electronic properties and tunnel-like structure motifs were investigated. A KSbO_3 -type structure with a space group of $Im-3$ and $Pn-3$ was determined for $\text{K}_{0.84}\text{OsO}_3$ and $\text{Bi}_{2.93}\text{Os}_3\text{O}_{11}$, respectively. The magnetic and electronic transport properties of the polycrystalline compounds were compared with those obtained theoretically. It was revealed that the $5d$ tunnel-like structures were paramagnetic with metallic charge conduction at temperatures above 2 K. This was similar to what was observed for structurally relevant $5d$ oxides, including $\text{Bi}_3\text{Re}_3\text{O}_{11}$ ($\text{Re}^{4.33+}$; $5d^{2.66}$) and $\text{Ba}_2\text{Ir}_3\text{O}_9$ ($\text{Ir}^{4.66+}$; $5d^{4.33}$). The absence of long-range magnetic order seemed to be common among $5d$ KSbO_3 -like oxides, regardless of the number of $5d$ electrons (between 2.6 and 4.3 per $5d$ atom).

Double-perovskite oxides $\text{Ca}_2\text{MgOsO}_6$ and $\text{Sr}_2\text{MgOsO}_6$ have been synthesized under high-pressure and high-temperature conditions (6 GPa and 1500 °C). Their crystal structures and magnetic properties were studied by a synchrotron X-ray diffraction experiment and by magnetic susceptibility, specific heat, isothermal magnetization, and

electrical resistivity measurements. $\text{Ca}_2\text{MgOsO}_6$ and $\text{Sr}_2\text{MgOsO}_6$ crystallized in monoclinic ($P2_1/n$) and tetragonal ($I4/m$) double-perovskite structures, respectively; the degree of order of the Os and Mg arrangement was 96% or higher. Although $\text{Ca}_2\text{MgOsO}_6$ and $\text{Sr}_2\text{MgOsO}_6$ were isoelectric, a magnetic-glass transition was observed for $\text{Ca}_2\text{MgOsO}_6$ at 19 K, while $\text{Sr}_2\text{MgOsO}_6$ showed an antiferromagnetic transition at 110 K. The antiferromagnetic-transition temperature was the highest in the family. A first-principle density functional approach revealed that $\text{Ca}_2\text{MgOsO}_6$ and $\text{Sr}_2\text{MgOsO}_6$ were likely to be antiferromagnetic Mott insulators in which the band gaps open, with Coulomb correlations of $\sim 1.8\text{-}3.0$ eV. These compounds offered a better opportunity for the clarification of the basis of 5d magnetic sublattices, with regard to the possible use of perovskite related oxides in multifunctional devices.

Double perovskite containing $\text{Ir}^{6+}/\text{Ir}^{5+}$ with formula $\text{Ca}_2\text{NiIrO}_6$ was synthesized using a high pressure synthesis technique. Its electronic state was studied through magnetic susceptibility, heat capacity and electrical resistivity measurement. It was found that $\text{Ca}_2\text{NiIrO}_6$ crystallized in space group $P2_1/n$ with lattice parameters $a = 7.6456(2)$ Å, $b = 5.5343(1)$ Å, $c = 9.3287(4)$ Å, $\beta = 144.870(5)^\circ$. Magnetic susceptibility measurement indicated that $\text{Ca}_2\text{NiIrO}_6$ orders in a canted antiferromagnetic state at about 72 K. $\text{Ca}_2\text{NiIrO}_6$ exhibited semiconductor like behavior. Double perovskites containing Ir^{6+} were rarely reported. In particular, we observed the extraordinary large coercivity at 10 K, compared with other canted antiferromagnetic iridium oxides.

Keywords:

5d oxides, High-pressure synthesis, Crystal structure, Magnetic property.

List of Abbreviations

MPMS	Magnetic property measurement system
PPMS	Physical property measurement system
XRD	X-ray diffraction
SXRD	Synchrotron X-ray diffraction
FC	Field cooling
ZFC	Zero field cooling
T_C	Curie temperature
T_N	Neel temperature
DOS	Density of states
AF	Antiferromagnetic
FM	Ferromagnetic
E_a	Activation energy
NN	Nearest neighbor
t	Tolerance factor
θ	Weiss temperature
C	Curie constant
μ_{eff}	Effective magnetic moment
μ_S	Spin only magnetic moment
μ_{S+L}	Magnetic moment from full spin and orbital motion
BVS	Bond valance sum
Θ_D	Debye temperature
γ	Electronic specific heat coefficient
C_p	Heat capacity
C_{lat}	Heat capacity of lattice contribution

NIMS	National Institute for Materials Science
SO	Spin-orbit
E_F	Fermi energy
J	Nearest-neighbor exchange constant
DFT	Density functional theory
MIT	Metal-insulator transition
λ	Spin-orbit coupling constant
2D	Two-dimensional
χ	Magnetic susceptibility
ρ	Electrical resistivity

High-Pressure Synthesis, Crystal Structures, and Magnetic Properties of Perovskite-Related Os and Ir Oxides

Contents

Chapter 1. Introduction	1
1.1 <i>5d</i> Transition metal oxides.....	1
1.2 Crystal structure.....	2
1.2.1 Perovskite and double perovskite structure.....	2
1.2.2. KSbO ₃ -type structure.....	5
1.3 Electronic structure.....	5
1.3.1. Crystal field environment.....	5
1.3.2. The Jahn-Teller effect.....	8
1.4 Magnetism.....	9
1.4.1 Origin of paramagnetic moments	9
1.4.2 Spin-orbit coupling.....	10
1.4.3. Magnetic susceptibility and Currie-Weiss law.....	12
1.4.4. Classes of magnetic materials.....	13
1.4.5. Antiferromagnetism and canted-antiferromagnetism.....	15
1.5. Exchange interactions.....	16
1.5.1. Superexchange	17
1.5.2. Anisotropic exchange interaction.....	20
1.6. Overview for the <i>5d</i> oxides' application.....	21
1.7. Structure of this thesis.....	22
References in chapter 1.....	24
Chapter 2. Experimental methods.....	30
2.1. Sample synthesis: high-pressure method.....	30

2.2. X-ray diffraction.....	32
2.2.1. Powder X-ray diffraction.....	32
2.2.2. Synchrotron X-ray diffraction.....	33
2.2.3. Rietveld program: RIETAN.....	34
2.3. Magnetic properties measurement.....	35
2.4. Electrical properties measurement.....	36
2.5. Heat capacity measurement.....	37
References in chapter 2.....	38
Chapter 3. Crystal structure, and magnetic properties of KSbO_3 -type $5d$ oxides $\text{K}_{0.84}\text{OsO}_3$ and $\text{Bi}_{2.93}\text{Os}_3\text{O}_{11}$	40
3.1 KSbO_3 -type family overview.....	40
3.2 Experimental details.....	41
3.3 Crystal structure.....	43
3.4 Electrical properties.....	47
3.5 Magnetic properties.....	48
3.6 Heat capacity.....	49
3.7 Theoretical calculation.....	52
3.8 Conclusions.....	53
References in chapter 3.....	54
Chapter 4. Crystal structures, and magnetic properties of $5d$ double-perovskite oxides $\text{Ca}_2\text{MgOsO}_6$ and $\text{Sr}_2\text{MgOsO}_6$	59
4.1 Background knowledge.....	59
4.1.1 Double perovskite overview.....	59
4.1.2 Double perovskite with a single magnetic sublattice.....	60
4.2 Experimental details.....	64
4.3 Crystal structures.....	65
4.4 Electrical properties.....	73
4.5 Magnetic properties.....	74

4.5.1 Susceptibility.....	74
4.5.2 Isothermal magnetization.....	76
4.6 Heat capacity	77
4.7 Discussion.....	80
4.8 Theoretical calculation.....	81
4.9 Conclusion.....	85
References in chapter 4.....	86
Chapter 5 Crystal structures, and magnetic properties of double-perovskite oxides	
$\text{Ca}_2\text{NiIrO}_6$	92
5.1 Iridium oxides containing Ir^{6+}	92
5.2 Experimental details.....	92
5.3 Crystal structure.....	93
5.4 Magnetic properties.....	97
5.5 Heat capacity.....	100
5.6 Electronic properties.....	103
5.7 Conclusion.....	103
References in chapter 5.....	104
Chapter 6 General conclusions and future prospects.....	107
6.1 General conclusion.....	107
6.2 Future prospects.....	109
References in chapter 6.....	110
List of appended publications.....	112
Acknowledgement.....	116

Chapter 1. Introduction

1.1 *5d* Transition metal oxides

The extraordinary range of properties of transition metal oxides (TMO) were worthy of special attention in the past decades [1]. In olden days some properties like magnetism and colors were the natural power of some objects and substances. In recent years, like high-temperature superconductivity and topological insulator had been studied. The unique nature of the outer *d*-electrons was clearly at the core of the unusual properties of TMO. The valence electrons of *d*-orbitals in these transition metals could form a lot of different oxidation states. The metal-oxygen bond could change from ionic to metallic. As a result, the multiplicity of electronic properties of TMO varied from insulating to metallic.

In TMOs, there were two different kinds of competing forces among *d* electrons: Coulomb repulsion made the individual electrons localize at atomic lattice sites, while hybridization between the oxygen *p* electron state and *d* electron state lead to delocalize the electrons. The strong electron-electron correlation had resulted in a lot of striking phenomena in *3d* transition-metal system, such as Giant magnetoresistance and high-temperature superconductivity. However, *5d* TMOs had more extended orbitals compared with the *3d* and *4d* counterparts, as shown in **Fig. 1.1**. Therefore, the extended nature of the *5d* orbitals preferred much more overlaps of the nearest-neighbor ions, which lead to a broader bandwidth. It was commonly expected that these *5d* oxides were more metallic and less magnetic than their *3d* and *4d* counterparts. In fact, some *5d* oxides went beyond the expectation; for instance, both of Sr_2IrO_4 and $\text{Ca}_3\text{LiOsO}_6$ were magnetic Mott insulators [2]. The underlying physics was not as simple as that of *3d* TMOs. Because of spatially extended orbitals in *5d* oxides, the spin-orbit interaction increased. Thus, in *5d* TMOs, there were a lot of different characteristic energy scales, such as the interplay between spin-orbit interaction, on-site

repulsion, crystal-field splitting, and intersite hopping. They competed with each other, which made figuring out the mechanism in the *5d* TMOs complicatedly. For now, *5d* TMOs was a less explored domain, but as it attracted more attention of the researchers the tantalizing new phenomena had already been glimpsed.

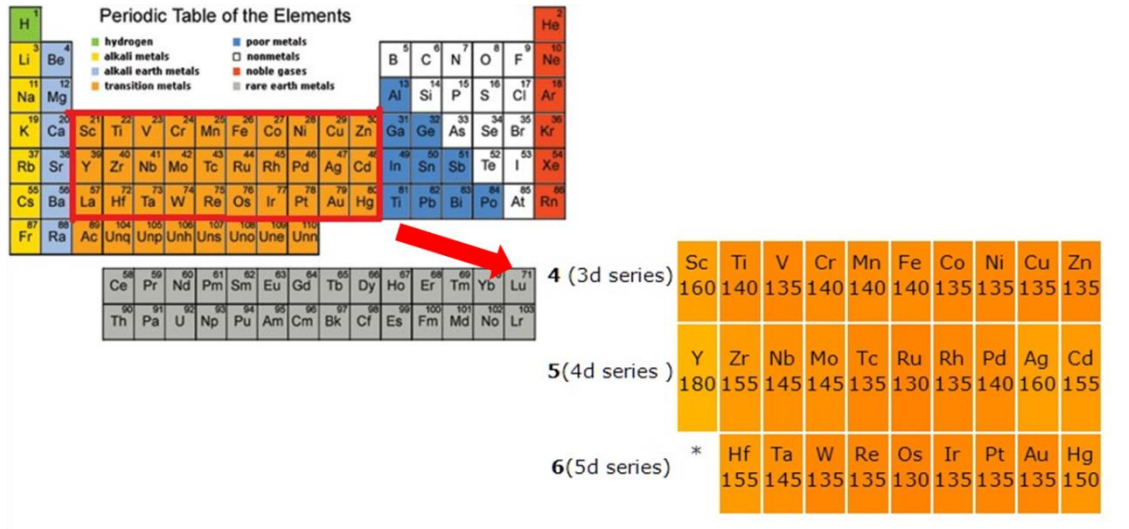


Figure 1.1. Periodic table. The enlarge part is transition elements of d-block, which are divided into *3d*, *4d* and *5d* series depending on the increasing number of d orbital [3].

1.2 Crystal structure

1.2.1 Perovskite and double perovskite structure

The perovskite (CaTiO_3) was named after a Russian mineralogist, L. A. Perovski. Since then, the perovskite family had attracted a lot of attentions, such as perovskite solar cell [4], dielectric resonator materials [5]. The perovskite structure generally crystallized in stoichiometry ABX_3 , where A and B were cations while X was an anion. The structure of a standard cubic perovskite was shown in **Fig. 1.2**, where one B cation with six X cations forming an octahedron, and the A cation was located at the center of eight octahedra. The structure was in terms of the BX_6 octahedra which share corners infinitely in all three dimensions. The space group for the ideal cubic perovskite was $Pm\bar{3}m$. Goldschmidt's tolerance factor was used as described perovskite structure by

formula $(r_A+r_X) = t\sqrt{2}(r_B+r_X)$. The perovskite structure was stable when $0.89 \leq t \leq 1.06$ (taking $r_X = 0.14$ nm). Ideal cubic structure only was observed at room temperature when t was close to 1. If A ions were small, $t < 1$, and tetragonal, orthorhombic and rhombohedral deformations of structure due to rotation and tilting of the BX_6 octahedra were observed. Other types of deformations were induced by the appearance of spontaneous polarization in ferroelectric perovskites [6].

However, with decreasing of A cation's size, the B-X-B attended to be bent slightly. Therefore, the tilting the BX_6 octahedra would bring some anions into A site cations. To describe this distortion [7], a tolerance factor, t , was introduced to the equation $(r_A+r_X) = t\sqrt{2}(r_B+r_X)$, where, r_A , r_B and r_X were the relative ionic radii of the A and B cations and the X ion, respectively.

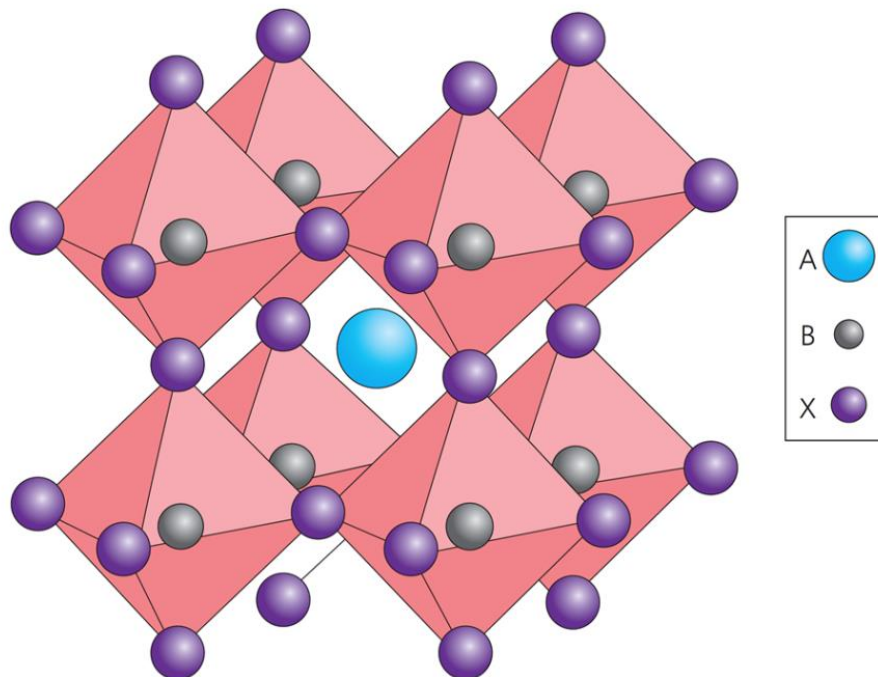


Figure 1.2. The illustration of an ideal ABX_3 perovskite structure [8].

It was called double perovskite structure because its unit cell was double of the perovskite. For investigating of the double perovskite oxides, it should trace back to

first Re-based double perovskites which reported by Longo and Ward [9]. There was no fast progress until the publication of $\text{Sr}_2\text{FeMoO}_6$ with half-metallic properties [10]. Possible spin-electronics application arising from the electronic structure caused a rapid progress in the field of the double perovskites. This involved the interplay of the crystallographic structure and both electronic and magnetic properties.

Double perovskites belonged to a large family of oxides with general formula $\text{A}_2\text{BB}'\text{O}_6$, where A being a large divalent or trivalent alkaline earth ion, B and B' being transition metal ions. The configuration was shown in **Fig. 1.3**. B and B' atoms were placed in the center of the oxygen octahedra. According to the significant size and valence of B and B' ions, they occupied the alternating crystallographic sites. B atoms had only B' atom neighbors and vice versa. BO_6 and $\text{B}'\text{O}_6$ octahedra were arranged in two interleaving fcc sublattices.

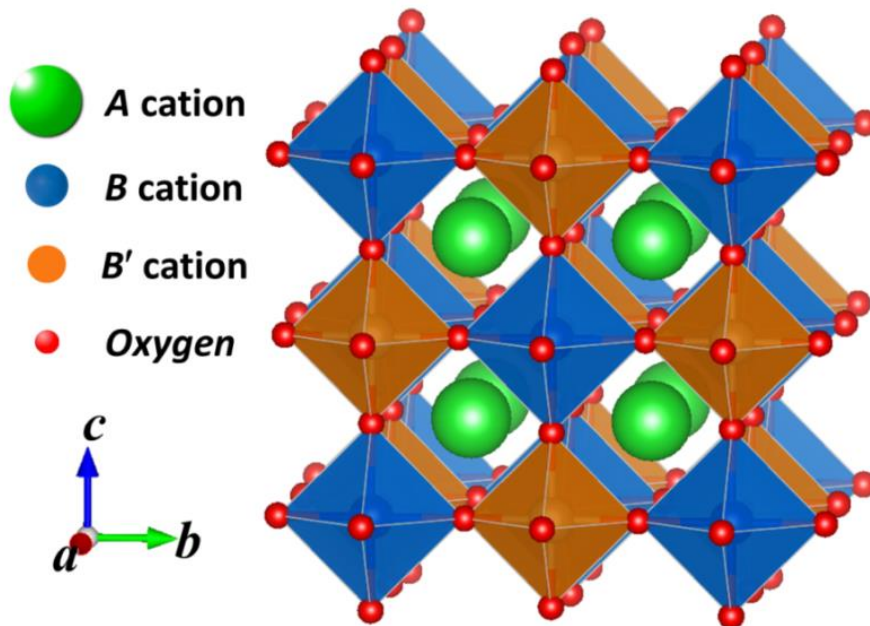


Figure 1.3. The illustration of an ideal $\text{A}_2\text{BB}'\text{O}_6$ double perovskite structure with rock-salt B-sites ordering [11].

The ideal double perovskite structure being a cubic one could be described in terms of the $Fm\bar{3}m$ space group (see **Fig. 1.2**). As in the case of the simple perovskite, a tolerance factor of the double perovskite could be defined in formula

$t = (r_A + r_O)/\sqrt{2}(\frac{r_{B^+}+r_{B^-}}{2} + r_O)$ [11]. It could be given as a general rule valid for whole double perovskite family that $f > 1.05$ required a hexagonal structure, for $1.05 > f > 1.00$, the cubic structure with $Fm\bar{3}m$ space group was the most likely one; for $1.00 > f > 0.97$, the compound had a tetragonal structure with $I4/m$ space group; and finally for $0.97 > f$, the compound became monoclinic having $P2_1/n$ space group or orthorhombic.

1.2.2 KSbO₃-type structure

Except for the perovskite structure mentioned above, there was the other three-dimensional mixed framework, KSbO₃-type structure, worthy for attention. Although, no interesting physical properties has been discovered by the scientists. Standing at structural point, this structure was interesting as a result of tunnel-like framework [12] with the composition vary from ABO₃ (KSbO₃ and KIrO₃) [13] to ABO_{3.667} (Bi₃GaSb₂O₁₁, Bi₃AlSb₂O₁₁, Bi₂NaSb₃O₁₁, Bi₃Ru₃O₁₁, and La₃Ru₃O₁₁) [14], [15].

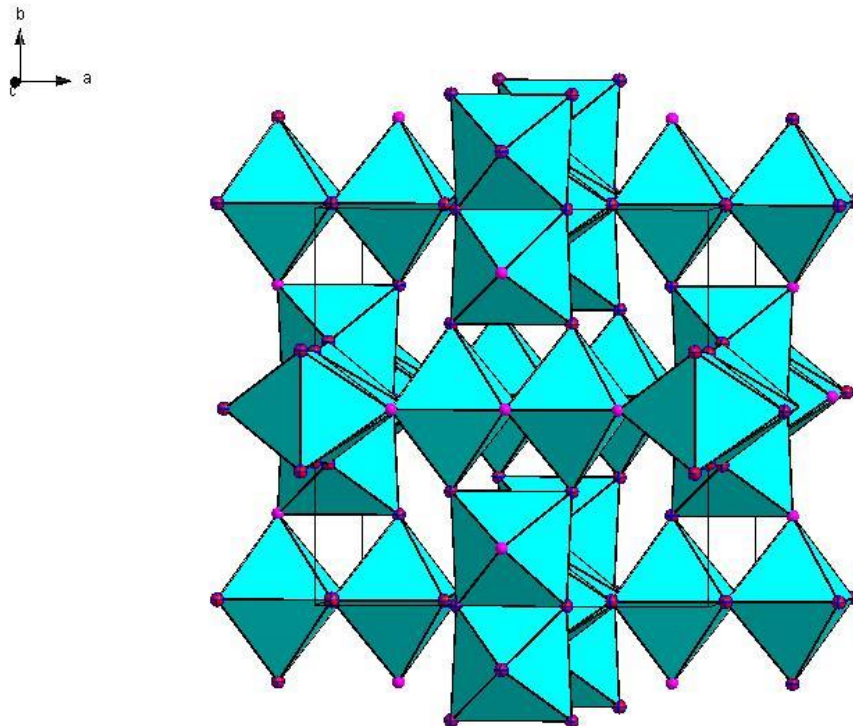


Figure 1.4 The illustration shows the connections between MnO₆ octahedra in KSbO₃.

In KSbO_3 -type structures, one BO_3 octahedron connected to the other one with sharing one edge, this pair of octahedra linked to the other one via a corner oxygen atom. These pairs extend to 3 dimension framework shown in **Fig. 1.4**. A cation could be inserted into this framework. For example, in cubic KSbO_3 , K^+ cations experienced with the SbO_3^- framework.

1.3 Electronic structure

1.3.1 Crystal field environment

For understanding the interaction of the metal ion with its environment it was necessary to consider the shapes of atomic orbital. We focused on the d -orbital (**Fig. 1.4**), because it played an important role in many transition metal compounds. The d -orbitals fall into two classes, the t_{2g} orbitals (pointing between the x , y and z axes) and e_g orbitals (pointing along the axes of coordinates in Cartesian frame). In the free atom model, the d -orbitals could be energetically degenerated owing to the spherically symmetric external environment. However, the energy levels of the atom would be modified by the field, due to the influence of neighboring atoms in a crystal environment. In other words, the atom was affected by the crystal field. In sum, crystal field theory described the electronic structures of transition metal ions in ligands, which were composed of metal ions and oxide ions or other anions. The interaction between these different ions could produce an electrostatic field with symmetry according to the crystal structure [16].

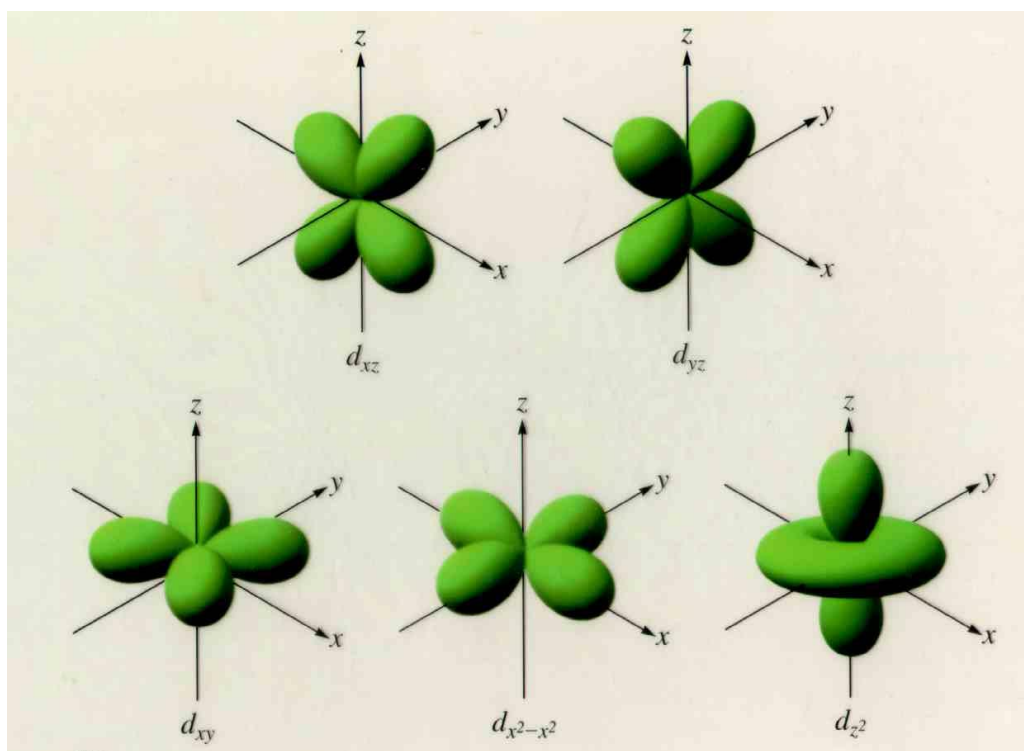


Figure 1.4. The illustration of angular distribution of the d-orbitals [17].

In oxides, the environment was the arrangement of the O^{2-} surrounding the transition metal atom. The most common case was octahedral environment as shown in **Fig. 1.5**. In octahedral coordination, a cation containing some *d*-electrons was located in the center of the octahedra, surrounded by 6 oxygen ions. Overlapping of the electron orbitals resulted in the crystal field potential, which hindering the rotation of the electrons and quenching the orbital angular momentum by introducing the splitting of the *d* orbitals. Namely, the two-fold e_g levels ($d_{x^2-y^2}$ and d_{z^2}) were raised in energy because of strongly overlapping between the d-orbitals and p-orbitals, and the three-fold t_{2g} levels were lowered in energy (see **Fig. 1.5**). The difference of resulting energy was identified as Δ_o (*o* for octahedral) [16], [18], and the exact value of the Δ_o strongly depended on configuration of the crystal field.

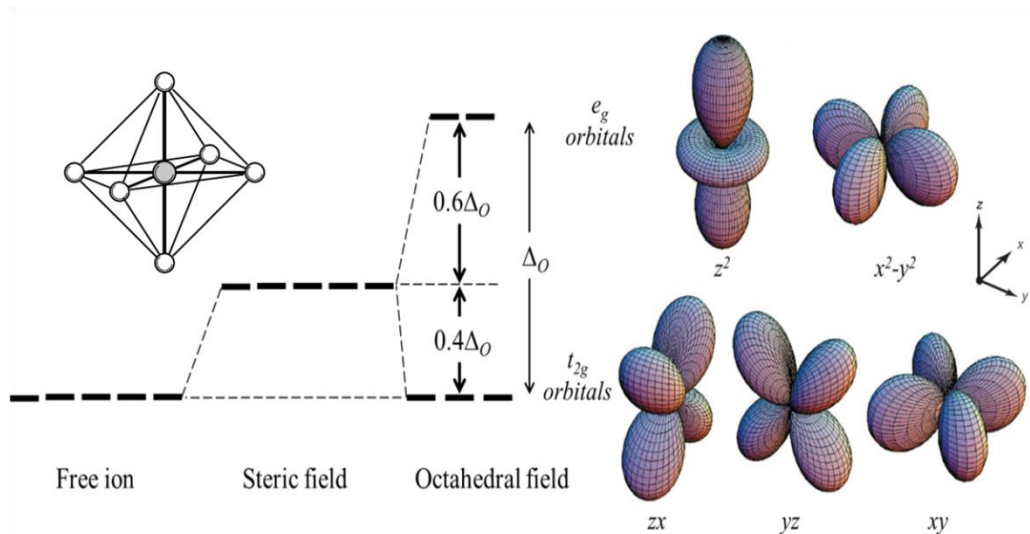


Figure 1.5. The d orbital splitting in octahedral field conditions [16], [18].

1.3.2 The Jahn-Teller effect

The crystal field was not always described in highly symmetric octahedral environment. There were so many factors which may lead to additional distortion of the environment, such as alternative valence, defects of crystal structure and external uniaxial pressure. The symmetry-breaking associated with displacement of the atoms would remove the electronic degeneracy. In **Fig. 1.6**, the distortion of octahedra resulted in splitting of the t_{2g} and e_g levels. The energy saving came from the lowering of the single-occupied e_g level. The energy for rising of the d_{xy} level was balanced by the lowering of the d_{xz} and d_{yz} . Such a phenomenon of the crystal structure's distortion was known as the Jahn-Teller effect. There were three different kinds of Jahn-Teller effect. Static Jahn-Teller effect: spontaneously occurred distortion was fixed on a particular axis of an octahedron and was permanently present in a crystal. Dynamic Jahn-Teller effect: originated from the special coupling to vibrational modes and low frequency electronic motion. The distortion occurred along different axes depending on temperature and may involve rapid hopping of the distortion from site to site (for materials involving ions with mixed valence). Cooperative Jahn-Teller distortion: spontaneous transition throughout the crystal at certain temperature. Because the

Jahn-Teller effect occurred due to lattice orbital coupling only, it was independent of spin and spin ordering temperatures, and the cooperative distortion may exhibit a thermal hysteresis [19]. For example, complexes of Cr^{2+} (d^4), high-spin Mn^{3+} (d^4), and Cu^{2+} (d^9) could produce the significant Jahn-Teller effects [20]–[23].

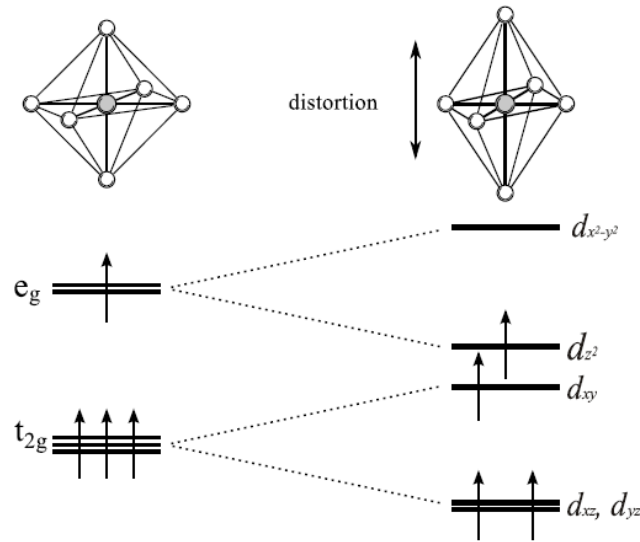


Figure 1.6. The schematic of the Jahn-Teller effect on example of Mn^{3+} [24].

1.4 Magnetism

1.4.1 Origin of paramagnetic moments

Normally, paramagnetism was defined as the magnetic state of an atom with one or more unpaired electrons. Most of the solids in the nature were considered as “non-magnetic” unless they were applied external field to develop a magnetic moment. Ordinarily these magnetic effects were weak and disappear once the magnetic field was removed. In a simplistic picture, an electron was driven by magnetic field to travel in a closed path around a nucleus. The moving charges could affect the magnetic effects of solids in two different aspects. First, electron could possess a spin, whose magnetic moment could interact with the external field. Secondly, the bound charges produced an

orbital momentum reacting to external field, either reinforcing it (paramagnetism) or fighting against it (diamagnetism).

For exploring the magnetic properties of the compound, a simple method was determining a magnetic moment in absence of a strong magnetic field. To predict the magnetic moment based on the electron quantum number, S , we could use the spin-only formula $\mu_s = [4S(S+1)]^{1/2}\mu_B$. However, we should start to think about orbital contributions to the magnetic moment. The magnetic moment could different from spin-only value μ_{so} and had a large effective moment called μ_{eff} . μ_{eff} could be quantified to incorporate spin (S) and orbital angular momentum (L), $\mu_{eff} = [L(L+1)+4S(S+1)]^{1/2}$. Normally, the measured magnetic moments were different from predict spin-only values (shown in **Table 1.1**). Every metal ion except for d^1 , d^2 , low spin $3d^5$ and high spin $3d^6$ followed spin-only (μ_{so}) prediction, as result of spin orbital coupling.

Table 1.1. Calculated and experimentally measured magnetic moments for $3d$ TMO in octahedra [25].

Ion	d^n	S	Magnetic moment (μ/μ_B)	
			Calculated	Experiment
Ti (III)	$d^1(t_{2g}^1)$	1/2	1.73	1.7-1.8
V(III)	$d^2(t_{2g}^2)$	1	2.83	2.8-3.1
Cr(III)	$d^3(t_{2g}^3)$	3/2	3.87	3.7-3.9
Fe(III)	d^5 high spin ($t_{2g}^3 e_g^2$)	5/2	5.92	5.7-6.0
Fe(III)	d^5 low spin (t_{2g}^5)	1/2	1.73	2.30
Fe(II)	d^6 high spin ($t_{2g}^4 e_g^2$)	2	4.9	5.0-5.6
Co(II)	$d^3(t_{2g}^3)$	3/2	3.87	4.3-5.2

1.4.2 Spin-orbit coupling

The spin-orbit interaction was a significant phenomenon which caused a rising of degeneracy of electronic energy levels in the complexes. The definition of spin-orbital coupling was kind of interaction of an electrons orbital angular momentum and its spin angular momentum, which leading a magnetic moment. The premise of occurrence of spin-orbital coupling was a half-filled or empty orbital for holding the unpaired electrons. In addition, the nearby symmetry related orbital did not contain an electron

with same spin as the first electron based on Hund's rule. Therefore, the electron in this orbital could utilize this nearby orbital vacancy to surround the center of the complex and produce orbital momentum (μ_L).

The value of spin-orbit interaction was proportional to Z_{eff}^4 (the effective atomic number) [26]. The data of spin-orbit coupling constant (λ) were shown in **Table 1.2**, which indicated the increasing with Z_{eff}^4 (from $3d$ to $5d$). So it played an important role in the properties of TMOs. In $3d$ TMOs, the energy magnitude of spin-orbit coupling was regularly smaller than that of on-site Coulomb repulsion energy and crystal field splitting. In $4d$ and $5d$ compounds, spin-orbital coupling could be compared with crystal field splitting, which resulted in complicated interplay of properties and unexpected ground states. For example, moment value of Os^{4+} (t_{2g}^4) complexes was usually $1.2 \mu_B$ or less [27], [28], which was totally different from the prediction in spin-only formula.

Table 1.2. Spin-orbit coupling constant (λ) for $4d$ and $5d$ shell ions [29]–[33].

4d shell ions							
ions	Ru ³⁺	Rh ²⁺	Rh ³⁺	Pd ²⁺	Ag ²⁺	Ag ³⁺	Cd ³⁺
λ [cm ⁻¹]	1180	1220	1400	1600	1840	1930	2325
5d shell ions							
ions	Os ⁴⁺	Os ⁵⁺	Os ⁶⁺	Ir ²⁺	Ir ⁴⁺	Ir ⁵⁺	
λ [cm ⁻¹]	3600	4500	5000	3450	4814	8760	

The other instance was shown in **Fig. 1.7**. The effective magnetic moment of a t_{2g}^4 configuration not only depend spin-orbit coupling constant λ but also related to the thermal energy kT . Although the λ value of Mn^{3+} and Cr^{2+} were much less than that of Os^{4+} . μ_{eff} of Mn^{3+} and Cr^{2+} were far greater than that of Os^{4+} . Therefore, octahedral Os^{4+} compounds exhibited a strong temperature dependence of magnetic moments [28].

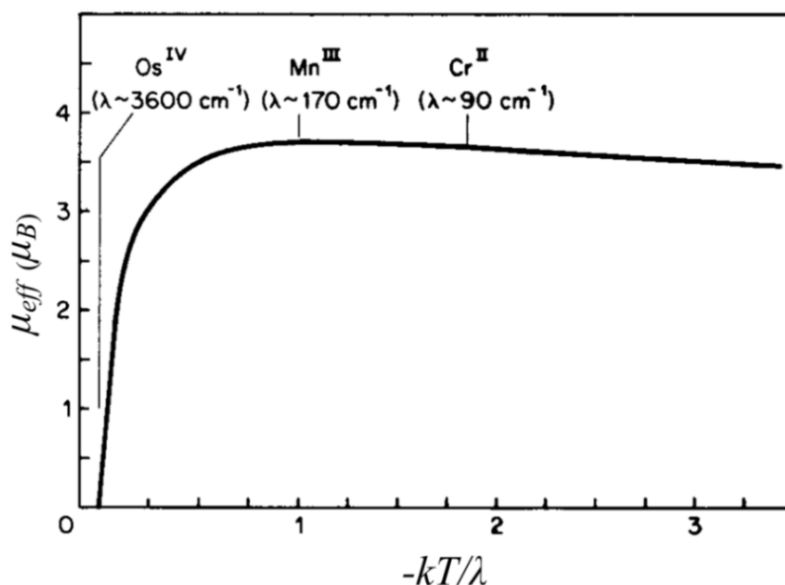


Figure 1.7. Schematic of the dependence on temperature and on the spin-orbit coupling constant λ of the effective magnetic moment of a d^4 ion in octahedral coordination[28].

1.4.3 Magnetic susceptibility and Currie-Weiss law

When the magnetic field H was applied to a solid, a relationship was found that the magnetization M was proportional to H : $M = \chi H$. The proportional constant χ was magnetic susceptibility of sample. When $\chi < 0$ meant diamagnetic, there was no unpaired electron orbital or spin angular momentum. If $\chi > 0$, it meant paramagnetic which kind of materials with unpaired electrons had a very strong temperature dependence [34]. Curie's law was proposed by Pierre Curie to study the relationship between paramagnetic susceptibilities and temperature [35]. Curie's law: $\chi = C / T$, where T was temperature, and C was Curie constant. On the one hand, the magnetic field would be apt to arrange the moments of atoms to one fix direction in paramagnetic materials. One the other hand, the thermal agitation would disturb the tendency of these moments' alignment [28].

Paramagnetic solids obeyed Curie law. However, when solids with the magnetic ordering (ferromagnet or antiferromagnet) obeyed Curie-Weiss law: $\chi = C / T - \theta$, where θ was Weiss constant. θ was indicative of intermolecular interactions among the moments.

$\theta > 0$ meant ferromagnetic interactions, while $\theta < 0$ indicated antiferromagnetic interactions (see in **Fig. 1.8**). As a result of some spontaneous interaction between nearby spins, Curie-Weiss Law was applied in the high temperature part, especially for above magnetic transition temperature. We could calculate the effective moment from Curie constant based on Curie-Weiss law, by using the equation $\mu_{\text{eff}} = 2.84\sqrt{\chi(T - \theta)} = 2.84\sqrt{C}$ [35].

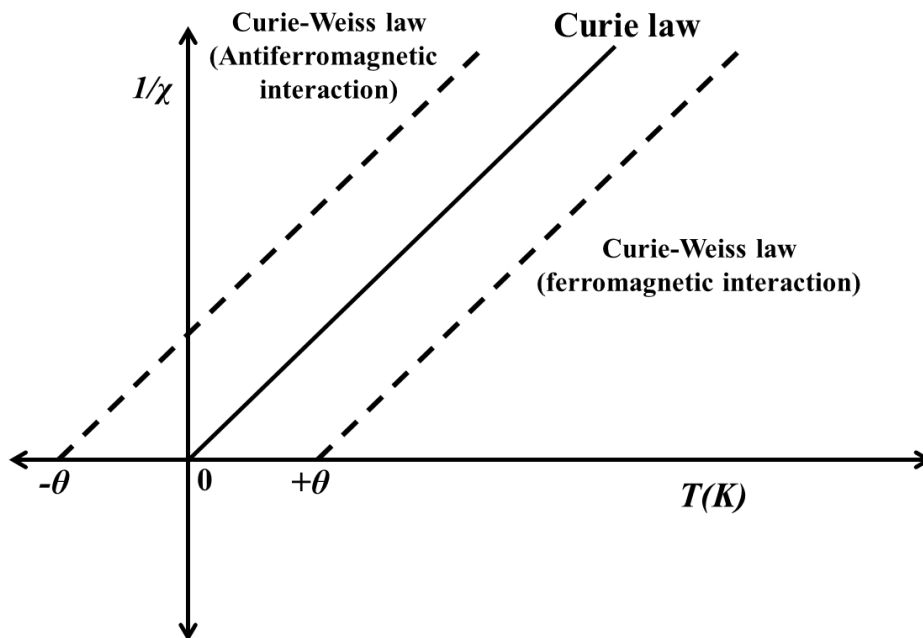


Figure 1.8. The illustration of Curie’s law and Curie-Weiss law [35].

1.4.4 Classes of magnetic materials

Unlike the paramagnetic materials, the parallel or antiparallel alignment of atomic moments could produce a very strong magnetic interaction in the materials. Magnetic ordering of ferromagnetic materials was that the adjacent spins were parallel to each other, lead to a larger net magnetization even in the absence of external magnetic field. In antiferromagnetic materials, the intrinsic magnetic moments of neighboring electrons were antialigned. So antiferromagnet had a zero net magnetization. Besides, the more complicated magnetic ordering could be presented due to the crystal structures. One of

them was called ferromagnetic ordering. **Fig. 1.9** showed four different types of spin arrangements.

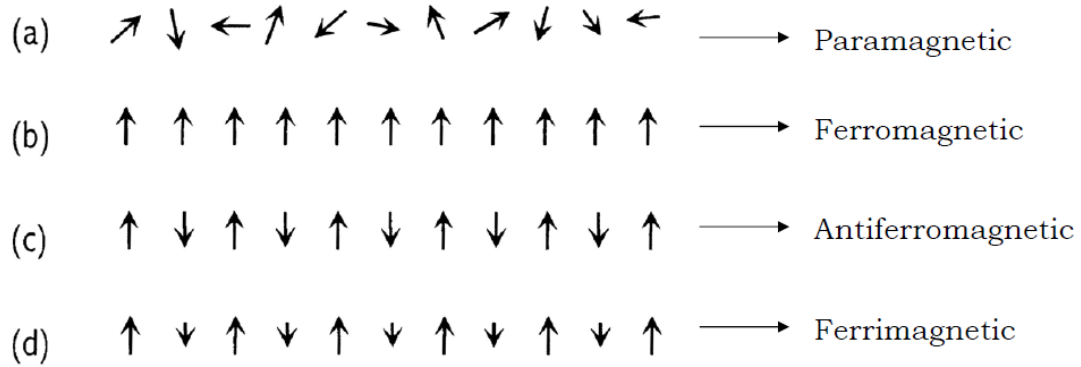


Figure 1.9. Diagrammatic sketches of (a) paramagnetic, (b) ferromagnetic, (c) antiferromagnetic and ferrimagnetic order arrangement.

In the magnetic solids, the spontaneous magnetization disappeared above at certain temperature. It was named Curie temperature T_c in ferromagnetic materials, and Neel temperature T_N in antiferromagnetic materials. Besides, in the experiment, T_c were often found to be a bit smaller than Weiss temperature, because of the neglecting influences of short-range order above T_c in the simple molecular-field treatment [36].

Except for characteristic Curie temperature and the saturation magnetization, ferromagnetic materials could keep the spin orientation even removing the external field. This phenomenon was named hysteresis. The schematic drawing of the magnetization dependence with the magnetic field was called hysteresis loop shown in **Fig. 1.10**. The intercept of the hysteresis loop on x-axis was the coercivity H_c . The materials with a large coercivity was usually called hard magnet and H_{ci} was defined as the reverse field that reduces the magnetization to zero [35].

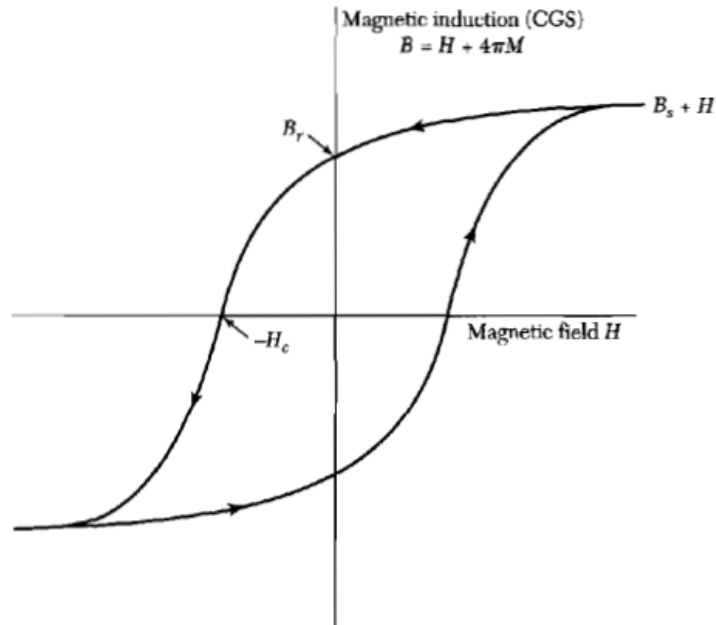


Figure 1.10 The technical magnetization curve (or hysteresis loop). The coercivity H_c is the reverse field that reduces B to zero: a related coercivity H_{ci} reduces M or $B-H$ to zero. The remanence B_r is the value of B at $H=0$. The saturation induction B_s is the limit of $B-H$ at large H , and the saturation magnetization $M_s = B_s/4\pi$ [35].

1.4.5 Antiferromagnetism and canted-antiferromagnetism

Many antiferromagnetic solid were TMOs. The spin direction between two nearest atoms was antiparallel in the antiferromagnetic materials, and the antiferromagnet had zero net moment (see **Fig. 1.9(a)**) below Neel temperature (T_N). In theory, the total net magnetization of antiferromagnetic materials was zero at absolute zero. But a small net magnetization is caused by the canted spins, such as hematite [37]. This phenomenon was called spin-canted antiferromagnetism. Spin-canted antiferromagnetism was an exceptional circumstance where the antiparallel magnetic moments were deflected from the antiferromagnetic plane, leading to a weak net magnetization (**Fig. 1.11**). The sufficiently strong magnetic field was applied to overturn the magnetization vectors, giving rising to field-induced reorientation affects. This kind of spin-flop transition was called the Morin transition. [37]

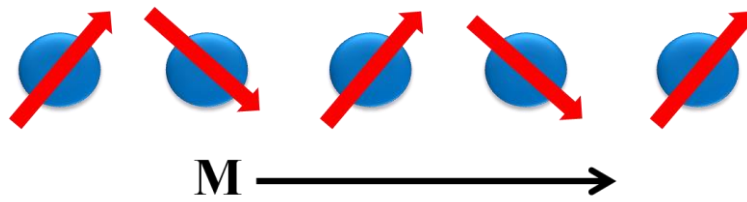


Figure 1.11. Ordered arrangement of electron spin in canted antiferromagnet

1.5 Exchange interactions

The discrete magnetic moments interacted mutually through a quantum mechanical force, that was, exchange interaction. The exchange interaction originated in the core of phenomenon of long range magnetic order. In the all different types of magnetic solids, the thermal excitations decreased with the temperature and spontaneous cooperative magnetic order was stable below a certain point. The quantum-mechanical couplings could be classified in different ways as shown in **Fig. 1.12**. In order to produce the long range magnetic order, the magnetic moments of individual ions needed to interact with each other.

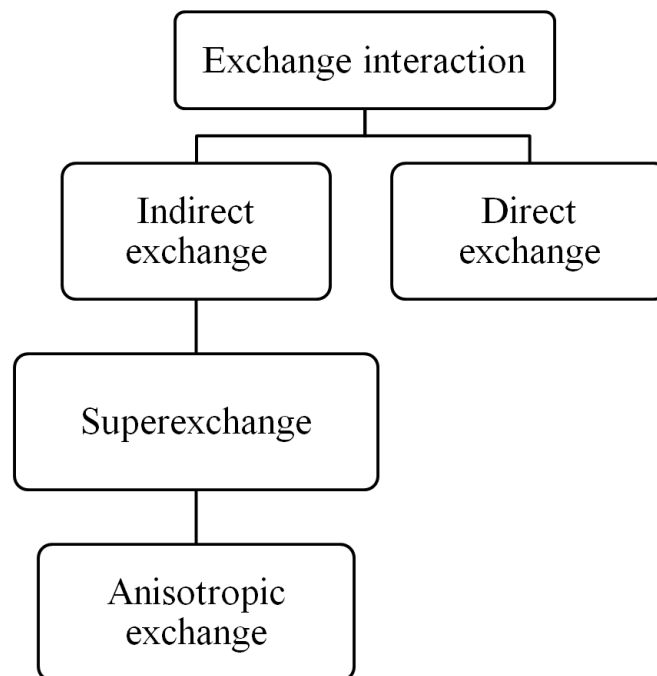


Figure 1.12. Hierarchy of exchange coupling.

1.5.1 Superexchange

The direct coupling through the chemical bonding between two magnetic atoms that were close enough to have significant overlap of their wave functions was called a direct exchange interaction. However, a coupling between two magnetic ions which were too far apart could be also mediated by a non-magnetic ion, which in case of the oxides is oxygen. First suggested by Kramers [38], such indirect exchange interaction was called superexchange. The excited states were the result of the electron removal from an oxygen ion and placing it on in an empty or half-filled cation orbital [39]. Depending on the mutual configuration and the types of orbitals involved in the process, several models of superexchange were described.

Anderson's mechanism described an interaction between the electron on p -shell of the anion and d -shell of the cation. This type of interaction was the strongest when the cation-anion-cation bond was aligned on $\sim 180^\circ$ (see **Fig. 1.13 (a)** and **(b)**). The type of the coupling, resulting from such interaction depended both on the sign of J (exchange integral) and the "sign of the bond". The latter term was a conventional characteristic and was determined by the initial occupancy of the d -orbital of the cation. The sign of the bond was defined by the following rule:

Negative bond: the cation d -orbital was less than half-filled and the electron transferred from the anion's (p or s) orbital aligns its spin orientation parallel to the spin of all the electrons, which was obvious result from the first Hund's rule, as shown in **Fig. 1.14 (a)**.

Positive bond: the d -orbital was more than half-filled. The transferred electron must align antiparallel to the cation spin because of the Pauli principle, as **Fig. 1.14 (b)**.

Depending on the product of these two factors the superexchange interaction could produce either antiferromagnetic (classical examples: CaMnO_3 , LaCrO_3 , LaFeO_3 , NiO) or much more rarely ferromagnetic interaction (theoretical example is $\text{Ni}^{2+}\text{-O}^{2-}\text{-V}^{2+}$) [40]. As a generalization of this mechanism, the antiferromagnetic interaction was expected between the cations of the same type. If the interaction took place between the

cations with different populations of the d -orbitals (i.e. more-than-half versus less-than-half-filled) the preferable coupling would be ferromagnetic [40].

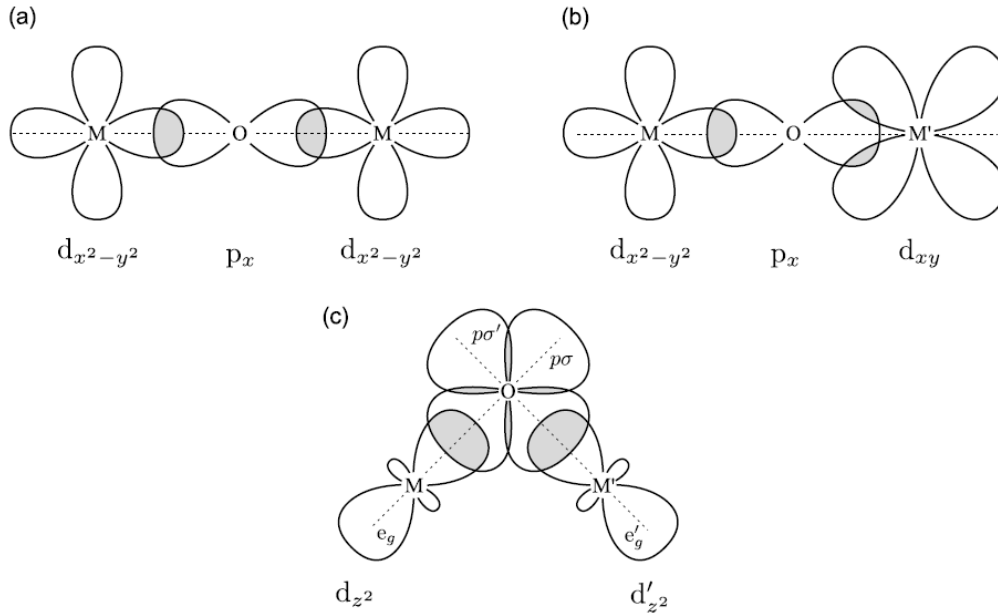


Figure 1.13: The illustrations of the in-line and orthogonal orientation of cation-anion-cation chain. Here, 180° case is for (a) same type ions, (b) different type ions and (c) is 90° coordination. M and M' are the ions of different type, thus different d -orbitals take part in interaction [35].

Another model was the Slater's mechanism, which considered the exchange interaction of the electron clouds between the anions and cations. The product of two simultaneous polarizations and “-” sign could determine the net sign of superexchange interaction, where “-” sign was a result of the Pauli principle within the intervening anion orbital [40]. A variation of this was the Goodenough's mechanism, which considered about the simultaneous partial bond formation of the anion with the cations on both sides. The calculation method of net sign in this Goodenough's mechanism was same to Slater's mechanism [39], [40].

The models described above are also applicable to the 90° interaction between magnetic ions (**Fig. 1.13 (c)**), although the situation and resulting coupling was quite different from 180° case. The formation of two partial covalent bonds $p\sigma$ - d_{z^2} and $p\sigma'$ - d'_{z^2} occurred simultaneously [41]. The sign of these was determined by same rule as

described in the Anderson's model. The $p\sigma$ and $p\sigma'$ orbitals interacted through direct exchange, and because these orbitals were mutually orthogonal the sign of interaction was positive, therefore they were ferromagnetically coupled. However, contrary to the 180° case, here the antiferromagnetic interaction was expected between a cation with a less-than-half filled d -shell and a cation with more-than-half filled d -shell. Similarly, the superexchange interaction between identical cations through 90° angle resulted in the ferromagnetic coupling, quite opposite to 180° case. Thus, using the symmetry relations and electron occupancy of the overlapping atomic orbitals plus the Pauli exclusion principle a series of semi-empirical principles were developed in the 1950s by Goodenough and Kanamori [39], [40], [42], naturally referred nowadays as the Goodenough-Kanamori rule. This rule could describe the magnetic properties successfully among a lot of materials. However in a number of cases the situation developed beyond these rules for an obvious reason. Among those were the cases when various types of exchange mechanisms compete with one another (i.e. exchange through the second nearest neighbor), when the bond coordination deviated from strict inline or orthogonal case, in case of dynamical electron orbital occupancy, or when a strong spin-orbit coupling took place.

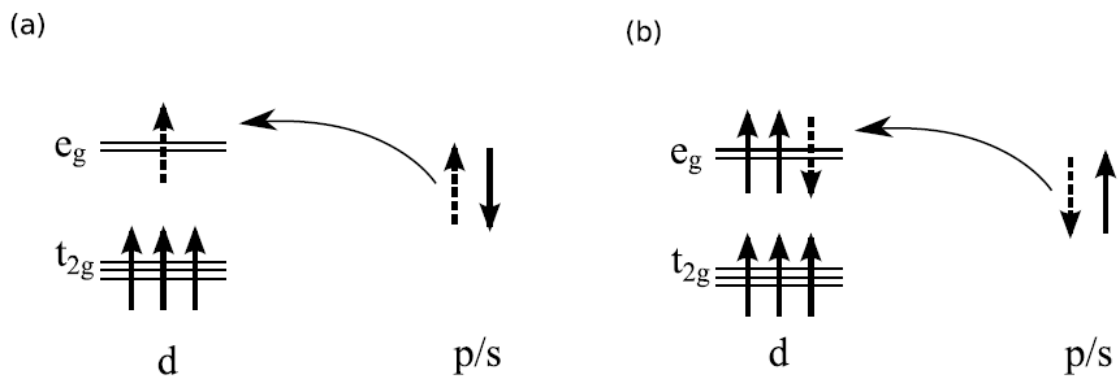


Figure 1.14: Formation of the negative (a) and positive (b) bonds at admixture of excited states with the ground state [39].

In the superexchange theory, both the correlation and the delocalization superexchange values decreased when two cations are separated by a pair of anions,

whose value scale was probably an order smaller than M -O- M' superexchange interaction [36]. But there were still some exceptions existed. For example, in $\text{Ca}_3\text{LiOsO}_6$, the original superexchange magnetic path Os-O-Os was disappeared. However, the extended superexchange path (Os-O)-(O-Os) could be expected to be responsible for the high transition temperature [43].

1.5.2 Anisotropic exchange interaction

This type of interaction led to arousal of a weak ferromagnetic component perpendicular to the spin-axis in initially antiferromagnetic material. Initially predicted purely on the ground of symmetry, the Dzyaloshinsky-Moriya (DM) [44]–[46] interaction arose from a combined effect of a strong relativistic spin-orbit coupling of the cations and the superexchange interaction. The interaction between the DM vector \mathbf{D} (which is proportional to the strength of spin-orbit interaction) and two spins on lattice bond with no inversion center made the spins cant by a small angle. The additional term that appeared in the Hamiltonian at this interaction $\hat{H}_{\text{DM}} = \mathbf{D} \cdot [\mathbf{S}_1 \times \mathbf{S}_2]$. The form of the interaction was such that it favored the spins \mathbf{S}_1 and \mathbf{S}_2 to be at right angles to the plane perpendicular to the vector \mathbf{D} , in such an orientation to ensure that the energy was negative. The moments \mathbf{S}_1 and \mathbf{S}_2 form separated sublattices with antiferromagnetic alignment, which were equivalent but not exactly antiparallel, resulting in a net magnetic moment. As mentioned above, the crystal symmetry was of particular importance for the anisotropic interaction. For the case of line AB with the midpoint C joining two magnetic cations i and j (see **Fig. 1.15**), the following rules described the direction of \mathbf{D} [36]:

- $\mathbf{D} = 0$ if a center of inversion symmetry was located at C ;
- $\mathbf{D} \perp AB$ if a mirror plane perpendicular to AB passed through C ;
- $\mathbf{D} \perp$ mirror plane if the mirror plane included AB ;
- $\mathbf{D} \perp$ two-fold axis if the two-fold rotation axis was perpendicular to AB at C ;
- $\mathbf{D} // AB$ if AB was an n -fold rotation axis ($n \geq 2$).

Simultaneously, \hat{H}_{DM} was opposed by a strong tendency towards ferromagnetic or

antiferromagnetic alignment from superexchange interaction; therefore in the typical real life systems the angles were small. However in the systems where the conflict is not strong, the canting angle could be up to $\pi = 2$ as was reported for β -MnS [47]. The classical example of this interaction was a weak ferromagnetic order arising in MnCO_3 , CoCO_3 and α - Fe_2O_3 compounds [44], [46]. More recently it had been proposed that this interaction also lead to a weak ferromagnetism existing in antiferromagnetic layers of La_2CuO_4 — the parent compound of high-temperature superconductors [48], [49]. DM interaction was considered to be the main motive force behind the most promising multiferroic materials, where noncollinearly coupled magnetic moments through the electron-lattice interaction displace the oxygen cations located between them [50].

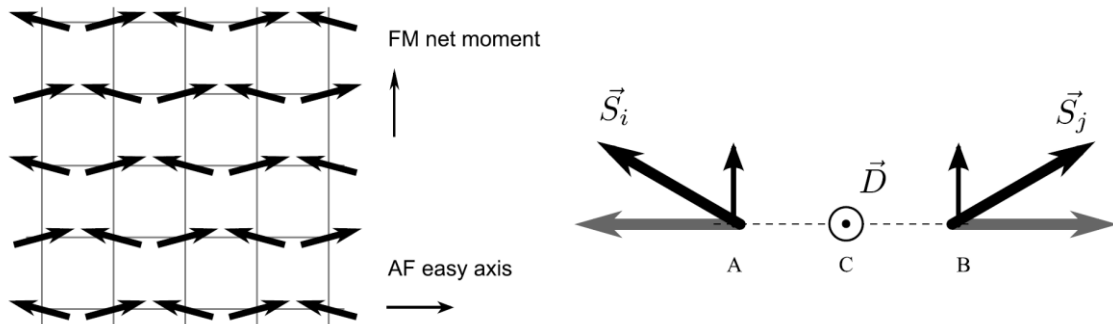


Figure 1.15. The illustration of the spin canting due to the Dzyaloshinsky-Moriya interaction. Weak ferromagnetic (FM) component arose perpendicularly to the spin-axis in initially antiferromagnetic (AF) materials [45].

1.6 Overview for the 5d oxides' application

As we mentioned above, 5d TMOs had strong spin orbit coupling, which lead to very interesting spin effects for electronics application. In the past decades, the theoretical scientists produced a number of predictions for 5d materials. These predictions included possible topological insulator, unconventional high temperature superconductivity, and spin liquid states which as-yet undiscovered emergent excitations called Majorana fermions. The more exotic anticipated examples were a

topological Mott insulator [51], [52] and a Weyl semimetal [53]. High T_c superconductors were widely studied materials. Yunoki and his colleagues reported an iridium oxide Sr_2IrO_4 which had similar layer structure to high T_c superconductor copper oxide. To resolve this issue, some theoretical studies investigated the superconducting properties in both electron and hole doping Sr_2IrO_4 [54]–[56]. In contrast to copper oxides, the extra electrons were predicted as the cause of the superconductivity in Sr_2IrO_4 . Experimentally metallic ferrimagnet $\text{Sr}_2\text{CrOsO}_6$ exhibited extraordinarily high T_c (725 K) for promising spintronic application [57]. Takagi and his colleagues proposed *5d* iridium oxide could be used as a material for spin-current detector [58]. Due to the strong SOC, the resistivity of *5d* Iridium TMOs such as IrO_2 and SrIrO_3 at ambient temperature were at least one order of magnitude higher than that of normal s metals. Because the sensitive detection of spin current could be achieved in materials with large resistivity, *5d* TMOs could be the good candidates for spin detection in spintronics devices. In overall, the area of *5d* transition metal oxides, and osmium and iridium oxides in particular, still remained largely unexplored and promises a great deal of exciting technological discoveries.

1.7 Structure of this thesis

In this thesis, I tried to synthesize the new *5d* oxides by high pressure method, and discussed the crystal structure and magnetic properties of these *5d* oxides. As a result of strong correlations between the charge carriers and strong spin-orbit interaction these compounds exhibited rather unconventional transport properties.

The thesis consists of six chapters. A brief introduction to crystal structure, electronic structure and magnetism was given in **Chapter 1**. The concise description of the high pressure experimental techniques and used in this work for characterization of the properties was presented in **Chapter 2**. These included X-ray diffraction, magnetization, electrical transport and thermodynamic properties measurements. I

reported two new *5d* oxide KOsO_3 and $\text{Bi}_3\text{Os}_3\text{O}_{11}$ in **Chapter 3**. The synthesis of KOsO_3 made the integrity of AOsO_3 (A =Alkali metal). In particular, the magnetic property of KOsO_3 was totally different from those of other members (Li/Na/Sr/BaOsO₃) [27], [59], [60]. Double perovskite oxides $A_2BB'O_6$ (*B* is nonmagnetic ion, *B'* is *4d/5d* transition metal ion) had attracted considerable attention recently due to the observation of a series of exotic magnetic states [61]. To explore notable magnetic behavior in osmium double perovskite oxides, two osmium containing double-perovskite oxides $\text{Ca}_2\text{MgOsO}_6$ and $\text{Sr}_2\text{MgOsO}_6$ were synthesized by using high pressure method. The detailed crystal structure and magnetic properties of these oxides would be discussed in **Chapter 4**. In **Chapter 5**, I presented a new iridate $\text{Ca}_2\text{NiIrO}_6$ with largest coercivity, compared with the existing canted antiferromagnetic iridium oxides. In **Chapter 6** revealed a general conclusion and outlines some prospects for follow-up research.

References in chapter 1

- [1] C. N. Rao and B. Raveau, *Transition Metal Oxides: Structure, Properties, and Synthesis of Ceramic Oxides, 2nd Edition*, 2nd ed. John Wiley & Sons, 1998.
- [2] B. J. Kim, H. Ohsumi, T. Komesu, S. Sakai, T. Morita, H. Takagi, and T. Arima, “Phase-Sensitive Observation of a Spin-Orbital Mott State in Sr_2IrO_4 ,” *Science*, vol. 323, no. 5919, pp. 1329–1332, Mar. 2009.
- [3] “<http://images.tutorvista.com/cms/images/101/transition-elements.png>.”
- [4] A. Kojima, K. Teshima, Y. Shirai, and T. Miyasaka, “Organometal Halide Perovskites as Visible-Light Sensitizers for Photovoltaic Cells,” *J. Am. Chem. Soc.*, vol. 131, no. 17, pp. 6050–6051, May 2009.
- [5] H. Tamura, T. Konoike, Y. Sakabe, and K. Wakino, “Improved High-Q Dielectric Resonator with Complex Perovskite Structure,” *J. Am. Ceram. Soc.*, vol. 67, no. 4, pp. c59–c61, Apr. 1984.
- [6] D. D. Fong, G. B. Stephenson, S. K. Streiffer, J. A. Eastman, O. Auciello, P. H. Fuoss, and C. Thompson, “Ferroelectricity in Ultrathin Perovskite Films,” *Science*, vol. 304, no. 5677, pp. 1650–1653, Jun. 2004.
- [7] P. K. Davies, H. Wu, A. Y. Borisevich, I. E. Molodetsky, and L. Farber, “Crystal Chemistry of Complex Perovskites: New Cation-Ordered Dielectric Oxides,” *Annu. Rev. Mater. Res.*, vol. 38, no. 1, pp. 369–401, 2008.
- [8] M. A. Green, A. Ho-Baillie, and H. J. Snaith, “The emergence of perovskite solar cells,” *Nat. Photonics*, vol. 8, no. 7, pp. 506–514, Jul. 2014.
- [9] A. W. Sleight, J. Longo, and R. Ward, “Compounds of Osmium and Rhenium with the Ordered Perovskite Structure,” *Inorg. Chem.*, vol. 1, no. 2, pp. 245–250, May 1962.
- [10] K.-I. Kobayashi, T. Kimura, H. Sawada, K. Terakura, and Y. Tokura, “Room-temperature magnetoresistance in an oxide material with an ordered double-perovskite structure,” *Nature*, vol. 395, no. 6703, pp. 677–680, Oct. 1998.

- [11] M. T. Anderson, K. B. Greenwood, G. A. Taylor, and K. R. Poeppelmeier, “B-cation arrangements in double perovskites,” *Prog. Solid State Chem.*, vol. 22, no. 3, pp. 197–233, 1993.
- [12] A. W. Sleight and R. J. Bouchard, “New cubic potassium antimony oxide derivative structure with interpenetrating networks. Crystal structure of bismuth gallium antimony oxide,” *Inorg. Chem.*, vol. 12, no. 10, pp. 2314–2316, Oct. 1973.
- [13] R. Hoppe and K. Claes, “Information on KIrO_3 ,” *Journal of the less-common metals*, vol. 43, no. 1, pp. 129–142, 1975.
- [14] K., Ismunandar Brendan J. and B. A. Hunter, “Temperature dependent neutron powder diffraction study of $\text{Bi}_3(\text{GaSb}_2)\text{O}_{11}$,” *Solid State Commun.*, vol. 108, no. 9, pp. 649–654, Nov. 1998.
- [15] F. Abraham, J. Trehoux, and D. Thomas, “METAL-METAL BONDS IN $\text{M}_{12}\text{O}_{36}$ CLUSTERS. 2. PREPARATION AND STRUCTURAL STUDY OF $\text{LA}_3\text{RU}_3\text{O}_{11}$ PHASE,” *Mater. Res. Bull.*, vol. 13, no. 8, pp. 805–810, 1978.
- [16] G. L. Miessler and D. A. Tarr, *Inorganic Chemistry*. Pearson Education, 2004.
- [17] S. S. Zumdahl and S. A. Zumdahl, *Chemistry*, 9th ed. Brooks Cole, 2013.
- [18] Y. Tokura and N. Nagaosa, “Orbital Physics in Transition-Metal Oxides,” *Science*, vol. 288, no. 5465, pp. 462–468, Apr. 2000.
- [19] B. Halperin and R. Engelman, “Cooperative Dynamic Jahn-Teller Effect. II. Crystal Distortion in Perovskites,” *Phys. Rev. B*, vol. 3, no. 5, pp. 1698–1708, Mar. 1971.
- [20] J. T. Vallin and G. D. Watkins, “The Jahn-teller effect for Cr^{2+} in II–VI crystals,” *Solid State Commun.*, vol. 9, no. 13, pp. 953–956, Jul. 1971.
- [21] J. A. Alonso, M. J. Martínez-Lope, M. T. Casais, and M. T. Fernández-Dáz, “Evolution of the Jahn–Teller Distortion of MnO_6 Octahedra in RMnO_3 Perovskites ($\text{R} = \text{Pr}, \text{Nd}, \text{Dy}, \text{Tb}, \text{Ho}, \text{Er}, \text{Y}$): A Neutron Diffraction Study,” *Inorg. Chem.*, vol. 39, no. 5, pp. 917–923, Mar. 2000.
- [22] M. W. Lufaso, W. R. Gemmill, S. J. Mugavero III, S.-J. Kim, Y. Lee, T. Vogt, and H.-C. zur Loye, “Synthesis, structure, magnetic properties and structural distortion

- under high pressure of a new osmate, $\text{Sr}_2\text{CuOsO}_6$,” *J. Solid State Chem.*, vol. 181, no. 3, pp. 623–627, Mar. 2008.
- [23] M. P. Attfield, P. D. Battle, S. K. Bollen, S. H. Kim, A. V. Powell, and M. Workman, “Structural and electrical studies of mixed copper/ruthenium oxides and related compounds of zinc and antimony,” *J. Solid State Chem.*, vol. 96, no. 2, pp. 344–359, Feb. 1992.
- [24] S. Blundell, *Magnetism in Condensed Matter*, vol. Oxford master series in condensed matter physics, 4 vols. Oxford University Press, 2001.
- [25] J. S. Griffith, *The theory of transition-metal ions*. Cambridge: Cambridge university press, 1961.
- [26] P. Atkins and J. de Paula, *Physical Chemistry*, 9th ed. New York: W. H. Freeman and Company, 2010.
- [27] Y. Shi, Y. Guo, X. Wang, A. J. Princep, D. Khalyavin, P. Manuel, Y. Michiue, A. Sato, K. Tsuda, S. Yu, M. Arai, Y. Shirako, M. Akaogi, N. Wang, K. Yamaura, and A. T. Boothroyd, “A ferroelectric-like structural transition in a metal,” *Nat. Mater.*, vol. 12, no. 11, pp. 1024–1027, Nov. 2013.
- [28] F. A. Cotton and G. Wilkinson, *Advanced Inorganic Chemistry*. John Wiley & Sons, 1980.
- [29] K. M. Mogare, W. Klein, H. Schilder, H. Lueken, and M. Jansen, “Synthesis, Crystal Structure and Magnetic Properties of Na_3OsO_5 ,” *Z. Für Anorg. Allg. Chem.*, vol. 632, no. 15, pp. 2389–2394, Nov. 2006.
- [30] M. Blume, A. J. Freeman, and R. E. Watson, “Theory of Spin-Orbit Coupling in Atoms. III,” *Phys. Rev.*, vol. 134, no. 2A, pp. A320–A327, Apr. 1964.
- [31] S.-R. Z. Wen-Chen Zheng, “Spin-Hamiltonian parameters and off-center displacements for Rh^{4+} and Ir^{4+} ions in rhombohedral BaTiO_3 ,” *Radiat. Eff. Defects Solids - RADIAT EFF DEFECT SOLID*, vol. 164, no. 3, pp. 178–182, 2009.
- [32] N. V. Vugman and S. R. Nogueira, “Spin,-orbit coupling constant in divalent

- iridium,” *Revista Brasileira de Física*, vol. 19, no. 4, 1989.
- [33] J. G. Zhao, L. X. Yang, Y. Yu, F. Y. Li, R. C. Yu, and C. Q. Jin, “Structural and physical properties of 1:2 B-site-ordered perovskite $\text{Ba}_3\text{CaIr}_2\text{O}_9$,” *J. Solid State Chem.*, vol. 182, no. 2, pp. 327–330, Feb. 2009.
- [34] L. Bornstein, *Numerical Data and Functional Relationships in Science and Technology*, vol. New Series. Heidelberg: Springer-Verlag, 1986.
- [35] C. Kittel, *Introduction to solid state physics*, 8th ed. Wiley, 2004.
- [36] J. B. Goodenough, *Magnetism and the chemical bond*, vol. Interscience monographs on chemistry: Inorganic chemistry section, 1 vols. Interscience, 1963.
- [37] R. C. Nininger Jr. and D. Schroerer, “Mössbauer studies of the morin transition in bulk and microcrystalline $\alpha\text{-Fe}_2\text{O}_3$,” *J. Phys. Chem. Solids*, vol. 39, no. 2, pp. 137–144, 1978.
- [38] H. A. Kramers, “L’interaction Entre les Atomes Magnétogènes dans un Cristal Paramagnétique,” *Physica*, vol. 1, pp. 182–192, 1934.
- [39] J. B. Goodenough and A. L. Loeb, “Theory of Ionic Ordering, Crystal Distortion, and Magnetic Exchange Due to Covalent Forces in Spinels,” *Phys. Rev.*, vol. 98, no. 2, pp. 391–408, Apr. 1955.
- [40] J. Kanamori, “Superexchange interaction and symmetry properties of electron orbitals,” *J. Phys. Chem. Solids*, vol. 10, no. 2–3, pp. 87–98, Jul. 1959.
- [41] T. N. Casselman and F. Keffer, “Right-Angled Superexchange,” *Phys. Rev. Lett.*, vol. 4, no. 10, pp. 498–500, May 1960.
- [42] J. B. Goodenough, “Theory of the Role of Covalence in the Perovskite-Type Manganites $[\text{La}, \text{M}(\text{II})]\text{MnO}_3$,” *Phys. Rev.*, vol. 100, no. 2, pp. 564–573, Oct. 1955.
- [43] Y. Shi, Y. Guo, S. Yu, M. Arai, A. Sato, A. A. Belik, K. Yamaura, and E. Takayama-Muromachi, “Crystal Growth and Structure and Magnetic Properties of the 5d Oxide $\text{Ca}_3\text{LiOsO}_6$: Extended Superexchange Magnetic Interaction in Oxide,” *J. Am. Chem. Soc.*, vol. 132, no. 24, pp. 8474–8483, Jun. 2010.

- [44] I. Dzyaloshinsky, “A thermodynamic theory of ‘weak’ ferromagnetism of antiferromagnetics,” *J. Phys. Chem. Solids*, vol. 4, no. 4, pp. 241–255, 1958.
- [45] T. Moriya, “New Mechanism of Anisotropic Superexchange Interaction,” *Phys. Rev. Lett.*, vol. 4, no. 5, pp. 228–230, Mar. 1960.
- [46] T. Moriya, “Anisotropic Superexchange Interaction and Weak Ferromagnetism,” *Phys. Rev.*, vol. 120, no. 1, pp. 91–98, Oct. 1960.
- [47] F. Keffer, “Moriya Interaction and the Problem of the Spin Arrangements in βMnS ,” *Phys. Rev.*, vol. 126, no. 3, pp. 896–900, May 1962.
- [48] T. Thio, T. R. Thurston, N. W. Preyer, P. J. Picone, M. A. Kastner, H. P. Jenssen, D. R. Gabbe, C. Y. Chen, R. J. Birgeneau, and A. Aharony, “Antisymmetric exchange and its influence on the magnetic structure and conductivity of La_2CuO_4 ,” *Phys. Rev. B*, vol. 38, no. 1, pp. 905–908, Jul. 1988.
- [49] S.-W. Cheong, J. D. Thompson, and Z. Fisk, “Metamagnetism in La_2CuO_4 ,” *Phys. Rev. B*, vol. 39, no. 7, pp. 4395–4398, Mar. 1989.
- [50] S.-W. Cheong and M. Mostovoy, “Multiferroics: a magnetic twist for ferroelectricity,” *Nat. Mater.*, vol. 6, no. 1, pp. 13–20, Jan. 2007.
- [51] D. Pesin and L. Balents, “Mott physics and band topology in materials with strong spin–orbit interaction,” *Nat. Phys.*, vol. 6, no. 5, pp. 376–381, May 2010.
- [52] B.-J. Yang and Y. B. Kim, “Topological insulators and metal-insulator transition in the pyrochlore iridates,” *Phys. Rev. B*, vol. 82, no. 8, p. 085111, Aug. 2010.
- [53] X. Wan, A. M. Turner, A. Vishwanath, and S. Y. Savrasov, “Topological semimetal and Fermi-arc surface states in the electronic structure of pyrochlore iridates,” *Phys. Rev. B*, vol. 83, no. 20, p. 205101, May 2011.
- [54] Y. Gao, T. Zhou, H. Huang, and Q.-H. Wang, “Possible superconductivity in Sr_2IrO_4 probed by quasiparticle interference,” *Sci. Rep.*, vol. 5, Mar. 2015.
- [55] H. Watanabe, T. Shirakawa, and S. Yunoki, “Monte Carlo Study of an Unconventional Superconducting Phase in Iridium Oxide $J_{\text{eff}}=1/2$ Mott Insulators Induced by Carrier Doping,” *Phys. Rev. Lett.*, vol. 110, no. 2, p. 027002, Jan.

2013.

- [56] Y. Yang, W.-S. Wang, J.-G. Liu, H. Chen, J.-H. Dai, and Q.-H. Wang, “Superconductivity in doped Sr₂IrO₄: A functional renormalization group study,” *Phys. Rev. B*, vol. 89, no. 9, p. 094518, Mar. 2014.
- [57] Y. Krockenberger, K. Mogare, M. Reehuis, M. Tovar, M. Jansen, G. Vaitheeswaran, V. Kanchana, F. Bultmark, A. Delin, F. Wilhelm, A. Rogalev, A. Winkler, and L. Alff, “Sr₂CrOsO₆: End point of a spin-polarized metal-insulator transition by 5*d* band filling,” *Phys. Rev. B*, vol. 75, no. 2, p. 020404, Jan. 2007.
- [58] K. Fujiwara, Y. Fukuma, J. Matsuno, H. Idzuchi, Y. Niimi, Y. Otani, and H. Takagi, “5*d* iridium oxide as a material for spin-current detection,” *Nat. Commun.*, vol. 4, Dec. 2013.
- [59] Y. G. Shi, Y. F. Guo, S. Yu, M. Arai, A. A. Belik, A. Sato, K. Yamaura, E. Takayama-Muromachi, H. F. Tian, H. X. Yang, J. Q. Li, T. Varga, J. F. Mitchell, and S. Okamoto, “Continuous metal-insulator transition of the antiferromagnetic perovskite NaOsO₃,” *Phys. Rev. B*, vol. 80, no. 16, p. 161104, Oct. 2009.
- [60] Y. Shi, Y. Guo, Y. Shirako, W. Yi, X. Wang, A. A. Belik, Y. Matsushita, H. L. Feng, Y. Tsujimoto, M. Arai, N. Wang, M. Akaogi, and K. Yamaura, “High-Pressure Synthesis of 5*d* Cubic Perovskite BaOsO₃ at 17 GPa: Ferromagnetic Evolution over 3*d* to 5*d* Series,” *J. Am. Chem. Soc.*, vol. 135, no. 44, pp. 16507–16516, Nov. 2013.
- [61] A. A. Aczel, D. E. Bugaris, L. Li, J.-Q. Yan, C. de la Cruz, H.-C. zur Loye, and S. E. Nagler, “Frustration by competing interactions in the highly distorted double perovskites La₂NaB'O₆ (B'=Ru, Os),” *Phys. Rev. B*, vol. 87, no. 1, p. 014435, Jan. 2013.

Chapter 2. Experimental methods

$5d$ oxides could be prepared by using the high pressure method [1]. In particular, osmium oxides were better to synthesized through high pressure method, because of avoiding toxic OsO_4 production exposed to human being. High pressure synthesis could significantly reduce the reaction time, in case the toxic substance was exposed to environment. For iridium oxides, high valence state Ir^{5+} and Ir^{6+} were usually obtained in high pressure experiment. The first iridium(VI) oxide was stabilized in an octahedral site of the perovskite lattice $\text{Ba}_2\text{CaIrO}_6$ in 1992 [2].

The aim of this chapter was to introduce the reader to the techniques employed in the research of $5d$ oxides of this thesis. All the samples reported in this thesis were synthesized by using high pressure and high temperature method. Their crystallography was characterized by X-ray diffraction (XRD) and synchrotron XRD. The magnetic properties and electrical properties were measured by magnetic property measurement system (MPMS) and physical property measurement system (PPMS), respectively.

2.1 Sample synthesis: high-pressure method

P.W. Bridgman laid the cornerstone for the high pressure physics and solid state chemistry [3]. The opposed anvil geometry was investigated to synthesis of diamond under the belt press by Bundy [4], which contributed to the development of the belt-type [5] and toroidal anvil instruments [6]. In addition, the piston cylinder apparatus had the larger experimental volumes but limited working pressure. These instruments were used to synthesis of new materials and help researchers to explore the unknown regions of the phase diagram which is not accessible at ambient pressure. In particular, there were a lot of advantages by using the high pressure method. Firstly, the presence of high non-metal partial pressures, *i.e.* high oxygen partial pressure, could be used to stabilize cations with extraordinary high oxidation states [7]. Secondly, dense packing of ions

could be often obtained by high pressure method. Finally, high pressure favors symmetric coordination environments [8]. For example, PbSnO_3 with cubic perovskite structure could only be synthesized using high pressure, however, ambient pressure synthesis leads to a mixture of orthorhombic PbO and SnO_2 [9].

The flat-belt (FB) type high pressure apparatus was installed in National Institute for Materials Science (NIMS), Tsukuba, Japan before 30 years [10]. It could achieve the pressure ranging from 3 GPa to 8 GPa and the highest temperature of 1800 °C. The out looking of the apparatus was shown in insert picture of **Fig. 2.1**. In this type of FB-type apparatus had two anvils, where one was fixed to upper part and the other could move up and down manipulated by control panel. Between the upper and bottom anvils, there were some rubber rings for improving tightness. For each run, the displacement between anvils decreased with pressing, which were estimated using different sensors. The press load was controlled by using an auxiliary small plunger pump. The cooling water was supplied before the heating. Graphite heaters were attached to anvils. We could monitor the heating progress via electronic current. After holding at target temperature for a while, the sample was quenched before the pressure releasing.

In this work, stoichiometric amounts of powder were mixed using a mortar in an Ar-filled glove box. The mixture was sealed in a Pt capsule and statically and isotropically compressed in a belt-type high-pressure apparatus (Kobe Steel, Ltd.). We used a pyrophyllite cell [11] to produce a quasihydrostatic condition at the pressure in a manner. The assemble way of sample cell followed the instruction showed in **Fig. 2.1**. The Pt capsule was heated by means of an internal graphite sleeve at certain temperature for certain time, while maintaining the high-pressure conditions. The samples were subsequently quenched at ambient temperature before releasing the pressure. The preparation condition in this thesis, the heating temperature is 1500 °C under 6 GPa for 1 hour.

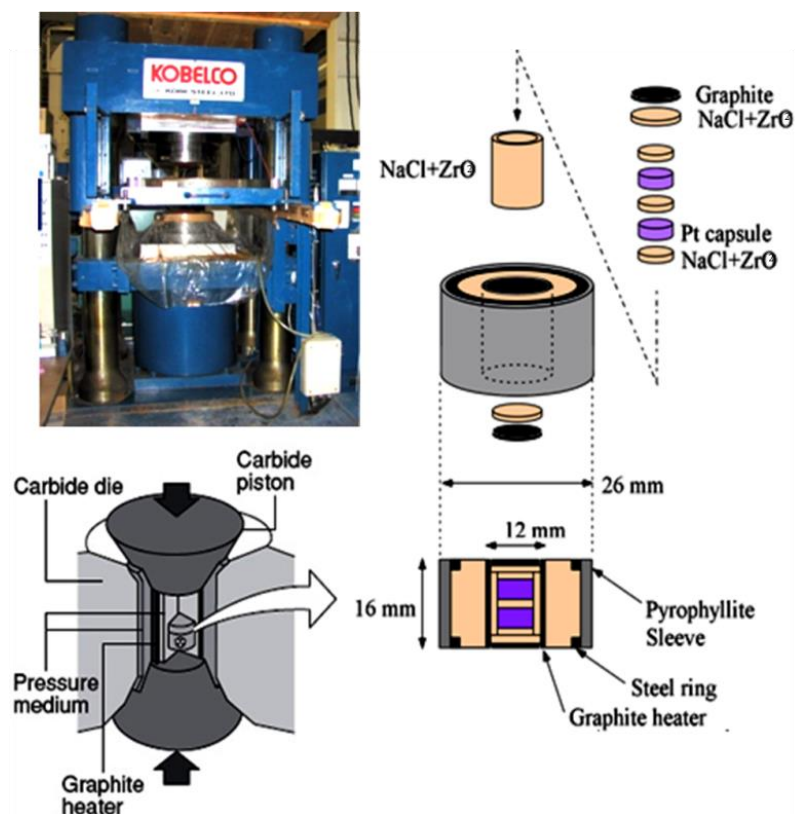


Figure 2.1. Picture of high pressure apparatus set at National Institute for Materials Science (NIMS), and the illustrations of the capsule and sample container.

2.2 X-ray diffraction

2.2.1 Powder X-ray diffraction

Diffraction methods were a fundamental tool for the crystallographic study. The X-ray diffraction (XRD) was used for studying *5d* oxides in this thesis. Photons of the incident X-ray beam interacted with the cloud of electrons surrounding the nucleus. The overlapping of the interaction was proportional to the atomic number Z [12]. Therefore, it was not possible to determine the accurate structures.

The experimental facility used in X-ray diffraction in this thesis was Rigaku RINT 2200. The used wavelength was that $\text{Cu K}\alpha$ being 1.54 \AA . Diffraction patterns were analyzed by Match! (TETRAGON analyse + technik) and JADE (MDI, Materials Data Inc.)

2.2.2 Synchrotron X-ray diffraction

Synchrotron radiation from the specific type of particle accelerator was observed in 1947 for first time. The special properties of synchrotron radiation derived from the relativistic movement of the charged particles along bending trajectories with a large radius of curvature. Synchrotron X-ray Diffraction (SXR) was a very powerful experimental technique used to analyze unknown materials in a short time. Synchrotron diffraction had several advantages. Data resolution was very high and X-rays generated by a synchrotron facility were at least 5 orders of magnitude more intense than the best X-ray laboratory source. Therefore, the diffraction pattern of SXR could show a fingerprint of the samples, including the information of space group, lattice parameters and coordinate. In addition, the preferred orientation could be reduced largely.

We did SXR measurement in Spring-8, located in Harima Science Park City, Hyogo Prefecture, Japan. The SXR data were collected by using the large Debye-Scherrer camera in BL15XU synchrotron-based X-ray diffraction facility [13]. The SXR diffraction data presented in this thesis have been analyzed by the Rietveld method using the RIETAN-FP computer program [14], [15]. For the successful Rietveld refinement with RIETAN-FP computer program, some data had to be known before the beginning of the procedure. We referred to the space groups and lattice parameters which were obtained from Match! and JADE based on X-ray refinement data. After that, we looked for the parent compounds with similar space groups and lattice parameter in ICSD database. The templates of the parent compounds were used in the refinement with RIETAN-FP. The refinement model including inter atomic distances, bond angles, sites occupancies and structure defects could be got finally.



Figure 2.2 The picture of the SPing8 site and a photo taken in front of BL15XU beamline setup.

2.2.3 Rietveld program: RIETAN

The FORTRAN program named RIETAN-FP was used for structure refinement in this work. The whole pattern fitting was based on the Maximum entropy method (MEM). RIETAN-FP offered a state-of-the-art structure refinement technique alternative to the classical Rietveld method: MEM-based Pattern Fitting (MPF). The MPF technology collaborative with RIETAN-FP could overcome the limitations of the conventional Rietveld analysis. The whole pattern fitting and MEM analysis were alternately repeated in an iterative process called REMEDY cycles. During the REMEDY cycles, the total number of the electrons could be fixed via the input of the user. Consequently, crystal structures were virtually represented not by structure parameters but by 3D electron densities within a unit cell.

Some reliability indices were used to measure the agreement between observed and calculated intensities. These numerical criteria were usually done in R values. The most significant reliability index was R_{wp} (R -weight pattern) that is defined as:

$$R_{wp} = \left\{ \frac{\sum_{i=1}^N w_i [y_i - f_i(x)]^2}{\sum_{i=1}^N w_i y_i^2} \right\}^{1/2},$$

where y_i was the observed intensity at step i , $f_i(x)$ the calculated intensity, and w_i the weight. R_p (R -pattern) defined as

$$R_p = \frac{\sum_{i=1}^N |y_i - f_i(x)|}{\sum_{i=1}^N y_i}.$$

A variation of R_p was R_R (R -Rietveld) defined by Rietveld as

$$R_R = \frac{\sum_{i=1}^N |y_i - f_i(x)|}{\sum_{i=1}^N |y_i - y_b(2\theta_i)|},$$

where both R_{wp} and R_p were influenced largely by the intensity of the diffraction lines and background. It was obvious that R_{wp} , for example, would be decreased with the background level. Empirically, it could not be expected to judge the relative quality of Rietveld refinements carried out by different data sets. For judging the quality of the fitting, the final R_{wp} value should be compared to the expected R_{wp} , R_e (R -expected), which was derived from the statistical error associated with the measured intensities,

$$R_e = \left[\frac{(N-n)}{\sum_{i=1}^N w_i y_i^2} \right]^{\frac{1}{2}}.$$

Thus, $S = R_{wp}/R_e$ was used as the goodness-of-fit indicator. When $S \leq 1.3$, the result of the refinement was usually acceptable.

2.3 Magnetic properties measurement



Figure 2.3. Image of the MPMS-7T system at NIMS Namiki-site.

The magnetization measurement facility located at NIMS Namiki-site was a Quantum Design Magnetic Property Measurement System (MPMS) magnetometer (as shown in **Fig. 2.3**), which was operated with a superconducting quantum interference device (SQUID) coil. The working temperature range was between 2 K and 400 K.

Liquid Helium was used to adjust the chamber temperature. The maximum applied magnetic field was up to ± 70 kOe.

A large part of this work during the examination of the properties of the $5d$ oxides was dedicated to the magnetic properties. The magnetic properties of all the samples in this thesis were measured by using MPMS-7T system (Quantum Design). Low temperature measurements (5-375 K) were performed with solid sample. The solid pieces were fixed in the certain position of plastic straw for avoiding movement. After the sample was put into the chamber, the temperature dependent magnetic susceptibilities (χ) were measured under both field cooling (FC) and zero field cooling (ZFC) conditions under a variety of magnetic fields. The field dependence isothermal magnetizations were measured between +70 kOe and -70 kOe at different temperatures.

2.4 Electrical properties measurement

A variety of physical properties could be performed by a Quantum Design Physical Properties Measurement System (PPMS) shown in the left panel of **Fig. 2.4**, *e.g.* resistivity, Hall coefficient and heat capacity.

In the investigation of the electrical properties, the most suitable were the four contacts arrangement of the electrodes for the semiconducting bulk samples and measuring low resistivity of good conductors. In this thesis, the electrical resistivity (ρ) of all the samples was measured by using PPMS-9T (Quantum Design). In the right panel of **Fig. 2.4**, the sketch of one of possible geometries of the measurement was presented. The obtained resistivity value came from sample and contacts. The contacts had been done using silver paste. The silver paste was a solution of mixed silver particles in two component epoxy. The connection between sample and contacts was Pt wire. Both of the silver paste and Pt wires were of low resistance, which could be neglected in the resistivity calculation. The resistivity of the materials was then given by

$$\rho = \frac{V_{2,3}}{I_{1,4}},$$

with $I_{1,4}$ being the current passing through the contacts 1 and 4, and $V_{2,3}$ being the voltage between the contacts 2 and 3. The conductance was calculated from formula

$$\sigma = \frac{V_{2,3}}{I_{1,4}} \frac{d}{a \times b},$$

where d was the distance between the contacts 2 and 3, a and b were the length and width of the sample as shown in **Fig. 2.4**.

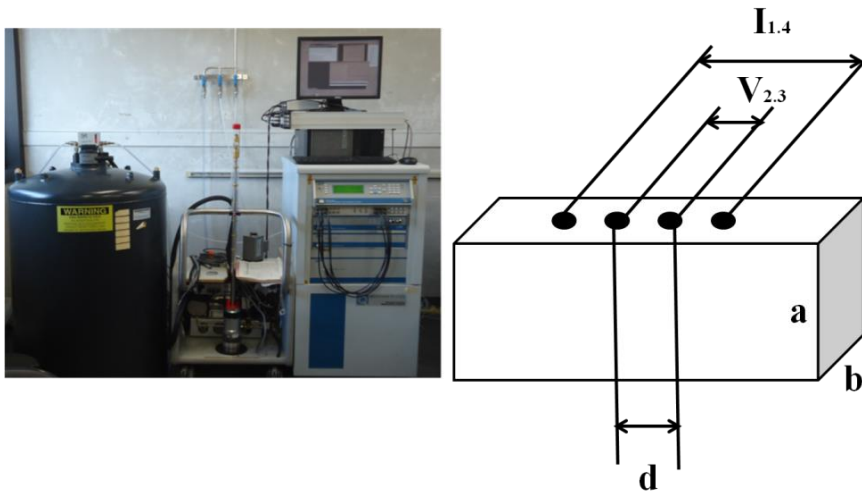


Figure 2.4. The image of the PPMS-9T system at NIMS Namiki-site. And the schematic of the four point resistivity measurement for a bulk sample.

2.5 Heat capacity measurement

Heat capacity was a measurable physical quantity amount to the change of the heat in the object system due to temperature rising. In addition to electrical property measurement, PPMS was designed to measure heat capacity. The measurements of heat capacity (C_p) could be made between 2 K and 300 K without magnetic field in the thesis. The sample with mass below 10 mg was stuck to sample holder via Apiezon N grease. The sample chamber was pumped down to 0.01 mTorr to minimize the thermal contact with the environment. The specific heat capacity was the heat capacity per mole.

References in chapter 2

- [1] J. B. Goodenough, J. A. Kafalas, and J. M. Longo, *High-pressure Synthesis Preparation Methods in Solid State Chemistry*. New York and London: Academic Press, Inc., 1972.
- [2] G. Demazeau, D.-Y. Jung, J.-P. Sanchez, E. Colineau, A. Blaise, and L. Fournes, "Iridium(VI) stabilized in a perovskite-type lattice: $\text{Ba}_2\text{CaIrO}_6$," *Solid State Commun.*, vol. 85, no. 6, pp. 479–484, Feb. 1993.
- [3] P. W. Bridgman, "Recent Work in the Field of High Pressures," *Rev. Mod. Phys.*, vol. 18, no. 1, pp. 1–93, Jan. 1946.
- [4] F. P. Bundy, "Designing tapered anvil apparatus for achieving higher pressures," *Rev. Sci. Instrum.*, vol. 48, no. 6, pp. 591–596, Jun. 1977.
- [5] H. T. Hall, "Ultra-High-Pressure, High-Temperature Apparatus: the 'Belt,'" *Rev. Sci. Instrum.*, vol. 31, no. 2, pp. 125–131, Feb. 1960.
- [6] L. G. Khvostantsev, V. N. Slesarev, and V. V. Brazhkin, "Toroid type high-pressure device: history and prospects," *High Press. Res.*, vol. 24, no. 3, pp. 371–383, Sep. 2004.
- [7] H. D. Hochheimer, *Frontiers of High Pressure Research II: Application of High Pressure to Low-Dimensional Novel Electronic Materials*. Springer Science & Business Media, 2001.
- [8] E. V. Boldyreva, "High-pressure-induced structural changes in molecular crystals preserving the space group symmetry: anisotropic distortion/isosymmetric polymorphism," *Cryst. Eng.*, vol. 6, no. 4, pp. 235–254, Dec. 2003.
- [9] F. Sugawara, Y. Syono, and S. Akimoto, "High pressure synthesis of a new perovskite PbSnO_3 ," *Mater. Res. Bull.*, vol. 3, no. 6, pp. 529–532, Jun. 1968.
- [10] O. Fukunaga, Y. S. Ko, M. Konoue, N. Ohashi, and T. Tsurumi, "Pressure and temperature control in flat-belt type high pressure apparatus for reproducible diamond synthesis," *Diam. Relat. Mater.*, vol. 8, no. 11, pp. 2036–2042, Nov. 1999.

- [11]J. Fernández-Sanjulián, E. Morán, and M. Á. Alario-Franco, “Synthesis, stability range and characterization of Pr₂Cu₂O₅,” *High Press. Res.*, vol. 30, no. 1, pp. 159–166, Mar. 2010.
- [12]J. M. Cowley, *Diffraction Physics*. Elsevier, 1995.
- [13]M. Tanaka, Y. Katsuya, and A. Yamamoto, “A new large radius imaging plate camera for high-resolution and high-throughput synchrotron x-ray powder diffraction by multiexposure method,” *Rev. Sci. Instrum.*, vol. 79, no. 7, p. 075106, Jul. 2008.
- [14]F. Izumi and K. Momma, “Three-Dimensional Visualization in Powder Diffraction,” *Solid State Phenom.*, vol. 130, pp. 15–20, 2007.
- [15]F. Izumi, H. Asano, H. Murata, and N. Watanabe, “Rietveld analysis of powder patterns obtained by TOF neutron diffraction using cold neutron sources,” *J. Appl. Crystallogr.*, vol. 20, no. 5, pp. 411–418, Oct. 1987.

Chapter 3. Crystal structure, and magnetic properties of KSbO₃-type 5*d* oxides K_{0.84}OsO₃ and Bi_{2.93}Os₃O₁₁

3.1 KSbO₃-type family overview

Crystalline KSbO₃-type [1] or comparable-type solid-state oxides were attractive for their possible applications in ionically conductive and electrocatalytic materials [2]–[5]. This prospect might be related to the presence of tunnel motifs in the crystal structure of these oxides [6]. Furthermore, structurally related La₄Ru₆O₁₉ has received considerable attention because of its role in novel electronic transport in non-Fermi-liquids [7], [8]. The KSbO₃-type family of solid-state oxides was currently an emergent subject in the field of inorganic chemistry. They could be used to develop advanced technologies for energy-related applications and to help understand correlated electron properties.

The KSbO₃-type family of oxides consists of several compositional variants have been synthesized and characterized by the similar tunnel motifs, such as the following:

- *AMO*₃: KSbO₃ [1], KIrO₃ [9], BaOsO₃ [10], KBiO₃ [4], [11], AgBiO₃ [12];
- *A₃M₃O₁₁*: La₃Ir₃O₁₁ [13], Bi₃Ru₃O₁₁ [3], La₃Ru₃O₁₁ [7], [14], Bi₃Os₃O₁₁ [15], [16], Bi₃Mn_{1.9}Te_{1.1}O₁₁ [17], Bi₃Re₃O₁₁ [18], Bi₃CrSb₂O₁₁ [19], Bi₂La*M*Sb₂O₁₁ (*M* = Cr, Mn, Fe) [19], NaBi₂Sb₃O₁₁ [20];
- *A₂M₃O₉*: Sr₂Re₃O₉ [18];
- *A₄M₆O₁₉*: La₄Re₆O₁₉ [18], Pb₆Re₆O₁₉ [18], Ba₄Os₆O₁₈Cl [21], La₄Os₆O₁₉ [21], Sr₄Ru₆ClO₁₈ [22], and La₄Ru₆O₁₉ [7], [8].

Most of these examples were synthesized at ambient pressure, whilst high-pressure heating has led to successful syntheses of additional compounds, which include NaOsO₃ [15], Bi₃Mn₃O₁₁ [17], [23], [24], Bi₃Ge₃O_{10.5} [25], Ba₂Ir₃O₉ [26], and Bi₃Cr_{2.91}O₁₁ [27].

Our recent studies have focused on the synthesis of solid-state osmium oxides in order to develop 5*d* electronic properties and 5*d* materials for possible advancements in

the field of spintronics and related scientific devices [28]–[31]. During our attempted syntheses of compositionally new osmium oxides under high-pressure and high-temperature conditions, an additional oxide $\text{K}_{0.84}\text{OsO}_3$ was synthesized (at 6 GPa). The polycrystalline compounds $\text{K}_{0.84}\text{OsO}_3$ was studied by using synchrotron X-ray diffraction and magnetic and charge transport measurements. The refined crystal structure indicated that the crystalline oxide has a KSbO_3 -type structure and shares a tunnel structural motif with a related Os oxide $\text{Bi}_{2.93}\text{Os}_3\text{O}_{11}$ [15], [16]. Herein, we report the synthesis, crystal structure, and primary electrical and magnetic properties of the newly synthesized KSbO_3 -type oxide $\text{K}_{0.84}\text{OsO}_3$ and compare those with the properties of the structurally comparable oxide $\text{Bi}_{2.93}\text{Os}_3\text{O}_{11}$.

3.2 Experimental details

Polycrystalline $\text{K}_{0.84}\text{OsO}_3$ was synthesized by a solid-state reaction method in a belt-type high-pressure and high-temperature apparatus (Kobe Steel, Ltd, Japan), in which a pyrophyllite cell was used to produce a quasi-hydrostatic environment at an elevated pressure [32]. The starting materials Os (99.95%, Heraeus Materials Technology) and KO_2 (O_2 -45.6%, yellow powder, Sigma-Aldrich Co.) were mixed at a molar ratio of 1:2 in a glove box under argon. The mixture was sealed in a platinum capsule, followed by heating in a compressed pyrophyllite cell at 1500 °C for 1 h. The capsule pressure was maintained at 6 GPa during the heating process. The capsule was then quenched to ambient temperature within a minute by cutting off the electric power supply before releasing the pressure. The final product was a dense pellet of part of it was ground in an agate mortar and pestle. The powder was then rinsed in an ultrasonic water bath multiple times to remove any residue. The high-pressure method is helpful in reducing the risk of human exposure to possible presence of toxic OsO_4 during the synthesis.

Polycrystalline $\text{Bi}_{2.93}\text{Os}_3\text{O}_{11}$ was similarly prepared using fine powders of Bi_2O_3 (99.999%, Kojundo Chem. Lab. Co., Japan) and OsO_2 (Os-83%, Alfa Aesar) in the

high-pressure apparatus. A small amount of an oxygen source (KClO_4 , 99.5%, Kishida Chem. Co.) was added to a stoichiometric mixture of the starting materials. The elevated pressure was maintained at 6 GPa during the heating process at 1700 °C for 1 h. Residues in the final product (including KCl) were removed in a water bath.

The final products were characterized by synchrotron X-ray diffraction (SXR) using a large Debye-Scherrer camera at the beam line BL15XU in the SPring-8 synchrotron radiation facility, Japan [33]. The diffraction profiles were collected at room temperature between 2θ of 3° and 81° at 0.003° intervals using a monochromatized beam ($\lambda = 0.65298 \text{ \AA}$ or 0.40025 \AA). The wavelength was confirmed by measurements of a standard material (CeO_2). Each powder was placed into a Lindenmann glass capillary (inner diameter: 0.1 mm) and rotated during the measurements. The SXR profiles were analyzed by a Rietveld method using the program RIETAN-FP [34].

The dc magnetic susceptibility (χ) of the compound was measured in the Magnetic Property Measurement System (MPMS, Quantum Design) between 2 K and 395 K in an applied magnetic field of 10 kOe. Each powdered compound was loosely gathered in a sample holder and cooled to the temperature limit. The magnetic field was then applied to the holder. The holder was gradually warmed to 395 K (zero-field cooling, ZFC), followed by cooling in the field (field cooling, FC). The isothermal magnetization of the compounds was also measured in the apparatus with a magnetic field range between -70 and 70 kOe at 5 K. The specific heat C_p of a piece of the physically compressed bulk material was measured in the Physical Property Measurement System (PPMS, Quantum Design) between 2 K and 300 K. In the apparatus, the electrical resistivity (ρ) of a pellet piece was measured by a 4-terminal method using platinum wires and a silver paste.

The K content of polycrystalline $\text{K}_{0.84}\text{OsO}_3$ was determined by inductively coupled plasma spectrometry. Water-rinsed fine powder was used in the analysis and the average K content was found to be 0.837(7) in accordance with the formula unit.

First-principles calculations of the electronic state of the stoichiometric hosts KO_3 and $\text{Bi}_3\text{Os}_3\text{O}_{11}$ were performed by a generalized gradient approximation [35] of the

density functional theory. The WIEN2k program [36] was used, which was based on the full-potential augmented plane-wave method. The muffin-tin radii were chosen to be 2.4 atomic unit (*a.u.*) for K, 2.2 for Bi, 1.9 for Os, and 1.6 for O atoms. The spin-orbit interaction was included as a perturbation to the scalar-relativistic equations. The cut-off wave vector K was fixed at $RK = 8$, where R is the smallest muffin-tin radius (i.e. 1.6 *a.u.*). The Brillouin zone integration was approximated by the tetrahedron method with 294 k points in an irreducible zone for KOsO_3 and 76 k points for $\text{Bi}_3\text{Os}_3\text{O}_{11}$. We assumed that K atoms occupy the K1 site for KOsO_3 and Bi atoms occupy Bi1 (8*e*) and Bi2 (4*b*) sites for $\text{Bi}_3\text{Os}_3\text{O}_{11}$ to avoid fractional occupation.

3.3 Crystal structure

The crystal structure of $\text{K}_{0.84}\text{OsO}_3$ was characterized well by a cubic model with a space group of $Im\bar{3}$, similar to KBiO_3 and AgBiO_3 [4], [11], [12]. **Fig. 3.1** shows the SXRD pattern for $\text{K}_{0.84}\text{OsO}_3$ at room temperature. Rietveld analysis conducted on the pattern with the cubic model resulted in a well-refined profile with R indices below 7%. The refined cubic lattice parameter was $a = 9.47164(1) \text{ \AA}$, which is smaller than the corresponding cubic parameters of KBiO_3 [10.0194(6) \AA] and AgBiO_3 [9.7852(2) \AA]. The smaller ionic radius (0.575 \AA) of Os(V) in an octahedral environment than that of Bi(V) (0.76 \AA) may account for this observation [37]. We concluded that a reasonable fit was established; the final structural parameters, including the refined atomic coordinates, are listed in **Table.3.1**. Although the true chemical composition was slightly under-stoichiometric ($\text{K}_{0.84}\text{OsO}_3$), we analyzed the pattern without considering the small amount of K deficiencies that we were unable to refine. However, the thermal parameters for all atoms remained within a reasonable level regardless of the K deficiencies. The small amount of deficiencies may have been distributed almost equally over the three crystallographic K sites, minimizing impact on the analysis.

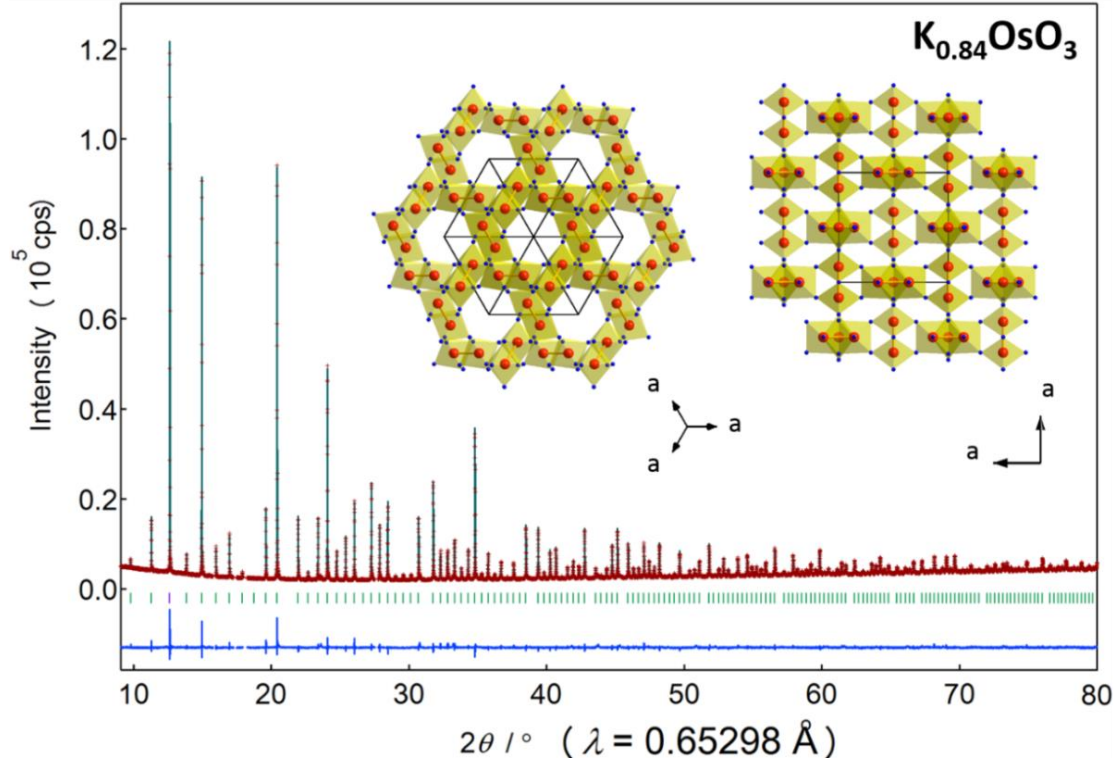


Figure 3.1. Rietveld analysis of the SXRD pattern for $\text{K}_{0.84}\text{OsO}_3$ at room temperature. Markers and solid lines show the observed and calculated profiles, respectively, and the difference is shown at the bottom of the figure. The expected Bragg reflections are marked by the small bars; and the reflections analyzed under partial profile relaxation are marked in purple color [34]. The proposed crystal structure is presented in the inset, in which Os and O atoms are drawn as large red and small blue balls, respectively. K atoms are not shown for clarity.

Table 3.1. Structural parameters of $\text{K}_{0.84}\text{OsO}_3$.

Atom	Site	g	x	y	z	B (\AA^2)
K1	16f	0.5	0.3429(2)	$= x$	$= x$	1.65(9)
K2	16f	0.213	0.2818(5)	$= x$	$= x$	1.4(2)
K3	2a	0.296	0	0	0	1.4(4)
Os	12e	1	0.5	0.14047(3)	0	0.237(4)
O1	12d	1	0.3482(7)	0	0	1.6(1)
O2	24g	1	0.3597(5)	0.2935(4)	0	0.74(7)

Note. The space group is $Im\bar{3}$ (no. 204), $a = 9.47164(1)$ \AA , $Z = 12$, $V = 849.718(2)$ \AA^3 , and $d_{\text{cal}} = 6.50$ g/cm^3 . R indices were $R_{\text{wp}} = 3.55\%$, $R_{\text{p}} = 2.47\%$, $R_{\text{B}} = 6.58\%$, and $R_{\text{F}} = 5.57\%$. The bond distances of Os–O in the OsO_6 octahedra were $d(\text{Os-O1}) = 1.972(6)$ \AA ($\times 2$), $d(\text{Os-O2}) = 1.954(6)$ \AA ($\times 2$), and $d(\text{Os-O2}) = 1.966(6)$ \AA ($\times 2$). $\text{BVS}(\text{Os}) = +4.63$, in which $\text{BVS} = \sum_{i=1}^N v_i$, $v_i = \exp[(R_0 - d_i)/B]$, N is the coordination number, $B = 0.37$ and $R_0(\text{Os}^{5+}) = 1.868$ (BVS, bond valence sum) [38].

The refined crystal structure was illustrated in the inset of **Fig.3.1**. The structural view indicated that an Os atom occupies the center of the octahedron. The view clearly showed a characteristic tunnel motif as was observed for other KSbO_3 -type and related oxides. In the octahedra, each edge or corner was shared by neighboring octahedra, causing the shortest Os–Os distance to be $2.6610(4)$ Å. The distance was 8.7% longer than the bonded Ru–Ru distance of $\text{La}_4\text{Ru}_6\text{O}_{19}$ (2.448 Å) and 12.5% shorter than the non-bonded Ru–Ru distance of $\text{La}_3\text{Ru}_3\text{O}_{11}$ [7], [8]. The distances might suggest that Os–Os bonding has formed. It could be noted that the ionic size of Os is slightly larger than that of Ru [37]; however, the ionic size difference was unlikely to affect the observation.

Fig. 3.2 showed the SXRD pattern for $\text{Bi}_{2.93}\text{Os}_3\text{O}_{11}$ measured at room temperature (as well as the refined pattern). In the refinement, $\text{Bi}_{2.93}\text{Os}_3\text{O}_{11}$ was assumed to be isostructural to $\text{Bi}_3\text{Mn}_3\text{O}_{11}$ [24]; fractional atomic coordinates for $\text{Bi}_3\text{Mn}_3\text{O}_{11}$ were tested in early refinements. The Bi1 atom was found to be disordered as in $\text{Bi}_3\text{Mn}_3\text{O}_{11}$ [24] and $\text{Bi}_3\text{GaSb}_2\text{O}_{11}$ [39]. Eventually, a refinement with an occupation factor (g) of $1/3$ for Bi1 and 1 for Bi2 resulted in a negative thermal parameter (B) for O1; however, the $B(\text{O1})$ was positive when we allowed the refinement of $g(\text{Bi1})$ and $g(\text{Bi2})$. A small amount of vacancies was therefore suggested at these sites; the refined composition was $\text{Bi}_{2.93}\text{Os}_3\text{O}_{11}$. The under-stoichiometric composition might be connected to the presence of a small amount of impurities in the compound. We also noted that splitting of Bi2 from the ideal $4b$ site $(0,0,0)$ to $8e$ site (x, x, x) resulted in slightly better R factors at $x = 0.0029(4)$. Note that the shortest Os–Os distance was $2.5653(3)$ Å, comparable with the Os–Os distance in $\text{K}_{0.84}\text{OsO}_3$.

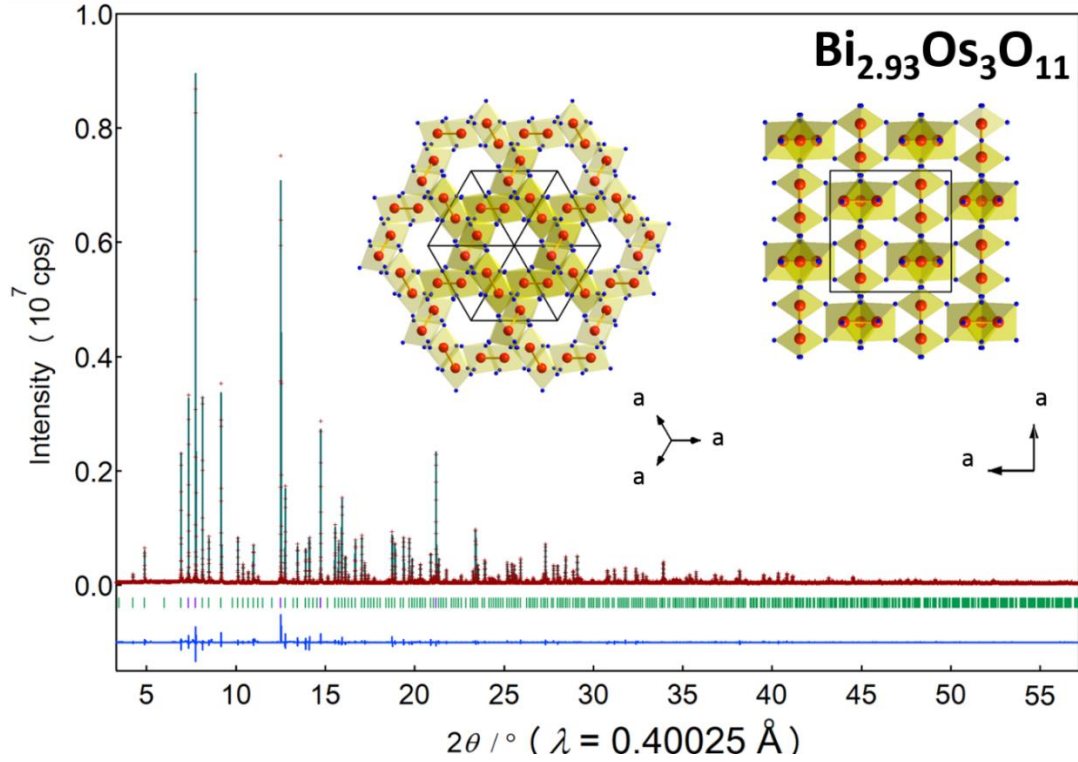


Figure 3.2. Rietveld analysis of the SXRD pattern for $\text{Bi}_{2.93}\text{Os}_3\text{O}_{11}$ at room temperature. Markers and solid lines show the observed and calculated profiles, respectively, and the difference is shown at the bottom. The expected Bragg reflections are marked by the small bars; and the reflections analyzed under partial profile relaxation are marked in purple color [34]. The proposed crystal structure is presented in the inset, in which Os and O atoms are drawn as large red and small blue balls, respectively. K atoms are not shown for clarity.

Table 3.2. Structural parameters of $\text{Bi}_{2.93}\text{Os}_3\text{O}_{11}$.

Atom	Site	g	x	Y	z	B (\AA^2)
Bi1	24h	0.3255(6)	0.3890(7)	0.3844(9)	0.3736(4)	0.39(2)
Bi2	8e	0.4887(9)	0.0029(4)	$= x$	$= x$	0.531(18)
Os	12g	1	0.38677(5)	0.75	0.25	0.161(4)
O1	8e	1	0.1501(5)	$= x$	$= x$	0.04(14)
O2	12f	1	0.5823(9)	0.25	0.25	0.36(14)
O3	24h	1	0.6018(6)	0.2426(5)	0.5343(6)	0.13(7)

Note. The space group is $Pn\bar{3}$ (no. 201) at origin choice 2, $Z = 4$, $a = 9.35993(2)$ \AA , and $V = 820.007(4)$ \AA^3 . R indices were $R_{\text{wp}} = 6.42\%$, $R_{\text{p}} = 4.03\%$, $R_{\text{B}} = 3.52\%$, and $R_{\text{F}} = 1.75\%$. The bond distances of Os–O in the OsO_6 octahedra were $d(\text{Os-O3}) = 1.991(4)$ \AA ($\times 2$), $d(\text{Os-O2}) = 1.991(5)$ \AA ($\times 2$), $d(\text{Os-O1}) = 1.994(4)$ \AA ($\times 2$). BVS(Os) were +3.37, +2.93, and +4.19, for which $\text{BVS} = \sum_{i=1}^N v_i$, $v_i = \exp[(R_0 - d_i)/B]$, N was the coordination number, $B = 0.37$, $R_0(\text{Os}^{5+}) = 1.868$ [38].

The OsO₆ framework of Bi_{2.93}Os₃O₁₁ was tunnel-like, similar to K_{0.84}OsO₃, as shown in the inset of **Fig. 3.2**. The Bi atoms were not shown in the structural views for clarity. When assuming an ionic picture of the compounds, the formal Os valence should be +5.16 for K_{0.84}OsO₃ and +4.33 for Bi_{2.93}Os₃O₁₁. This reflected the difference in the average Os–O bond distance of 1.964(8) Å and 1.992(1) Å for K_{0.84}OsO₃ and Bi_{2.93}Os₃O₁₁, respectively. It was also reasonable to expect that the Os–Os distance in K_{0.84}OsO₃ was longer than that of Bi_{2.93}Os₃O₁₁ owing to Coulomb repulsion between the positive charges; the observed Os–Os distance was indeed 3.7% longer than that of Bi_{2.93}Os₃O₁₁. Nevertheless, the bond valence sum (BVS) was +4.63 for K_{0.84}OsO₃ and +4.29 for Bi_{2.93}Os₃O₁₁. Although the BVS(Os) for Bi_{2.93}Os₃O₁₁ seemed to be comparable to that of the ionic picture of +4.33, the BVS(Os) for K_{0.84}OsO₃ was poorly estimated. The poor estimation might be because K_{0.84}OsO₃ is not purely ionic. The Os–Os bonding could possibly be more significant in K_{0.84}OsO₃ than in Bi_{2.93}Os₃O₁₁.

3.4 Electrical properties

The temperature dependence of ρ for a piece of polycrystalline K_{0.84}OsO₃ was measured (**Fig. 3.3**), and the metallic temperature-dependence was found over the studied temperature range. Although ρ (~0.025 Ω cm) at room temperature was approximately one order of magnitude higher than what was expected for a polycrystalline conducting oxide, the compound could still be characterized according to this type. In contrast, a piece of polycrystalline Bi_{2.93}Os₃O₁₁ showed a weak temperature dependence and a ρ of ~0.21 Ω cm at room temperature. However, this feature was not consistent with what is expected for a semiconducting oxide with an energy gap. Note that polycrystalline Bi₃Os₃O₁₁ synthesized without a high pressure process shows a ρ of ~0.001 Ω cm at room temperature [16], being remarkably lower than what was observed for the polycrystalline Bi_{2.93}Os₃O₁₁. The true conductivity of Bi_{2.93}Os₃O₁₁ was possibly masked by polycrystalline nature such as resistive grain boundaries and impurities. Additional

studies on single crystals of the oxides were necessary to reveal true nature of electric transport. Attempts to grow crystals of the oxides under high-pressure and high temperature conditions have been unsuccessful so far.

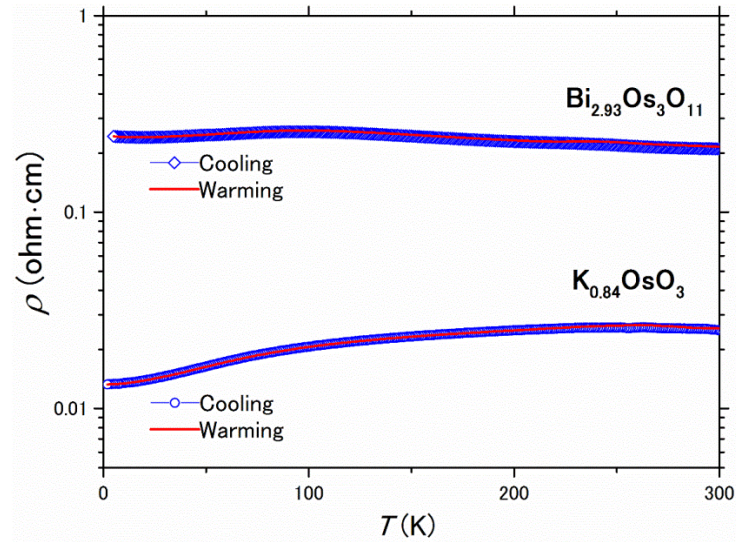


Figure 3.3. Temperature dependences of ρ of the polycrystalline $\text{K}_{0.84}\text{OsO}_3$ and $\text{Bi}_{2.93}\text{Os}_3\text{O}_{11}$.

3.5 Magnetic properties

The magnetic properties of polycrystalline oxides $\text{K}_{0.84}\text{OsO}_3$ and $\text{Bi}_{2.93}\text{Os}_3\text{O}_{11}$ were studied and compared. **Fig. 3.4** showed the temperature dependences of χ for the oxides, revealing weakly temperature-dependent paramagnetic features over the temperature range. Any possible magnetic transition was unlikely over the measurements. Although a broad and small bump was seen at approximately ~ 50 K for $\text{K}_{0.84}\text{OsO}_3$, any corresponding anomalies were not obvious in the ρ and C_p measurements (shown later). The inset showed the isothermal magnetizations of the oxides at low temperature (5 K) and only quasi-linear behaviors with trivial magnetizations were observed. Therefore, we tentatively assumed that the magnetic bump is likely impurity driven. The overall magnetic measurements suggested that the compounds are both paramagnetic at temperatures above 2 K. The temperature dependence of χ at the low temperature limit remained unconnected to any magnetic model and impurities.

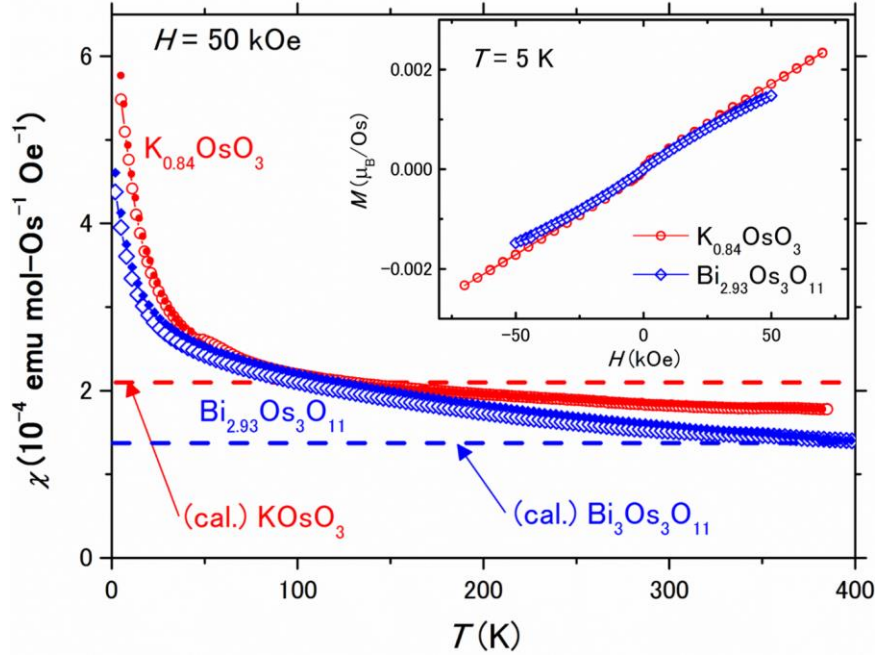


Figure 3.4. Temperature dependence of χ for polycrystalline $\text{K}_{0.84}\text{OsO}_3$ and $\text{Bi}_{2.93}\text{Os}_3\text{O}_{11}$ in a magnetic field of 50 kOe. Solid and open symbols represent data measured in FC and ZFC conditions, respectively. The dashed lines indicate the theoretically calculated χ for stoichiometric hosts KOsO_3 and $\text{Bi}_3\text{Os}_3\text{O}_{11}$ for comparison. The inset shows the isothermal magnetizations of the compounds at 5 K.

3.6 Heat capacity

Specific heat measurements for the oxides were conducted; their C_p vs. T curves were shown in **Figs. 3.5 (a) and (b)**. Over the temperature range, C_p varied monotonically and any indicative anomaly for a transition is unobvious. The C_p vs. T curve was analyzed by a linear combination of the Debye and Einstein model, as was conducted for related materials [40]. The analytical formula is

$$C_p(T) = n_D \times 9N_A k_B \left(\frac{T}{T_D}\right)^3 \int_0^{T_D/T} \frac{x^4 e^x}{(e^x - 1)^2} dx + n_E \times 3N_A k_B \left(\frac{T_E}{T}\right)^2 \frac{e^{T_E/T}}{(e^{T_E/T} - 1)^2},$$

where N_A was Avogadro's constant, and T_D and T_E were the Debye and Einstein temperatures, respectively. The scale factors, n_D and n_E , correspond to the number of vibrational modes per formula unit in the Debye and Einstein models, respectively. The fitting curves yielded the following: T_D of 628(7) K, T_E of 150(2) K, n_D of 2.88(3), and n_E

of 1.25(3) for $\text{K}_{0.84}\text{OsO}_3$; and T_D of 650(7) K, T_E of 110(2) K, n_D of 3.63(2), and n_E of 1.34(3) for $\text{Bi}_{2.93}\text{Os}_3\text{O}_{11}$. The Einstein term added to the Debye term increased the quality of fitting, suggesting a possibility that the phonon density of state (DOS) forms a rather complex structure over the whole temperature range. However, analysis on the C_p/T^3 vs. T plots (not shown) indicated that anomalous Einstein contributions, which were indicative of lattice rattling, were not obvious (unlike related oxides) [40]. Further analysis of the phonon modes was needed to clarify the phonon DOS structure of both the compounds.

The low-temperature measurements of the C_p/T vs. T^2 plot for each compound were analyzed by an approximated Debye model (**Figs. 3.5 (c) and (d)**), which was $C_p/T = \beta T^2 + \gamma$, where β and γ were a constant and the Sommerfeld coefficient, respectively. The fit of the plots yielded $\beta = 3.03(9) \times 10^{-4} \text{ J [one mole of osmium atoms (mol-Os)]}^{-1} \text{ K}^{-4}$ and $\gamma = 16.8(2) \text{ mJ mol-Os}^{-1} \text{ K}^{-2}$ for $\text{K}_{0.84}\text{OsO}_3$; and $\beta = 7.00(9) \times 10^{-4} \text{ J mol-Os}^{-1} \text{ K}^{-4}$ and $\gamma = 1.6(2) \text{ mJ mol-Os}^{-1} \text{ K}^{-2}$ for $\text{Bi}_{2.93}\text{Os}_3\text{O}_{11}$. The T_D for $\text{K}_{0.84}\text{OsO}_3$ and $\text{Bi}_{2.93}\text{Os}_3\text{O}_{11}$ were calculated from β of 315(4) K and 250(1) K, respectively. It appeared that the value of γ for $\text{Bi}_{2.93}\text{Os}_3\text{O}_{11}$ is nearly one tenth of that for $\text{K}_{0.84}\text{OsO}_3$; we therefore carefully investigated the electronic state of the compounds by a theoretical method.

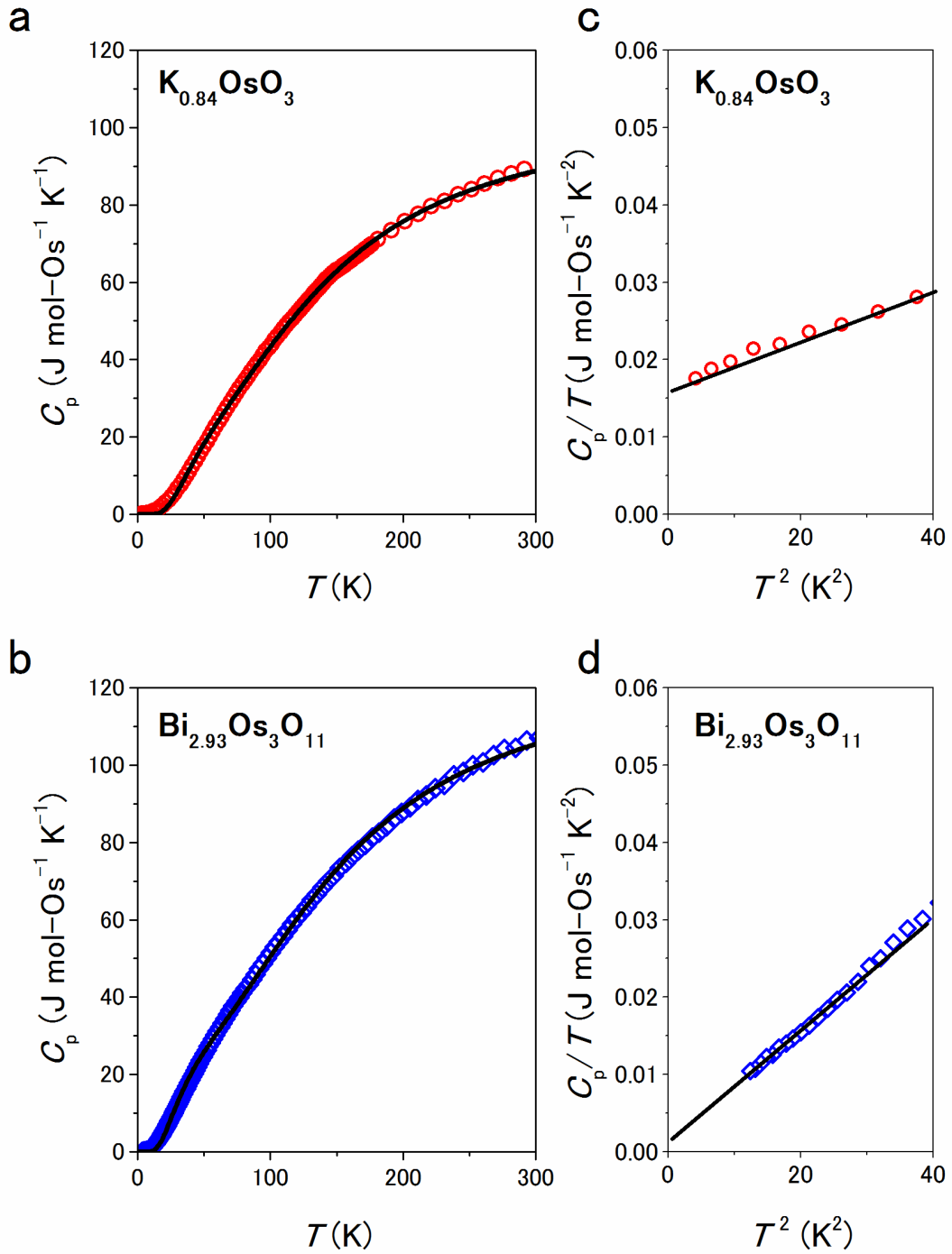


Figure 3.5. Temperature dependences of C_p of the polycrystalline (a) $K_{0.84}OsO_3$ and (b) $Bi_{2.93}Os_3O_{11}$. The solid line represents the fitting curve. A linear fit of the low-temperature measurements of the C_p/T vs. T^2 plot is shown for (c) $K_{0.84}OsO_3$ and (d) $Bi_{2.93}Os_3O_{11}$, respectively.

3.7 Theoretical calculation

Figs. 3.6 (a) and (b) showed the theoretically predicted electronic DOS structure for the stoichiometric hosts $\text{K}_{0.84}\text{OsO}_3$ and $\text{Bi}_{2.93}\text{Os}_3\text{O}_{11}$, respectively. The total DOS was found to consist of mainly Os and O contributions and little from K/Bi. Both compounds had a nontrivial electronic DOS at the Fermi level (E_F). Therefore, the hosts were expected to be metallic. The estimated γ for KOsO_3 from the DOS at E_F was $15.6 \text{ mJ mol-Os}^{-1} \text{ K}^{-2}$, which was nearly comparable to the observed γ for $\text{K}_{0.84}\text{OsO}_3$ [$16.8(2) \text{ mJ mol-Os}^{-1} \text{ K}^{-2}$]. However, the estimated γ for $\text{Bi}_{2.93}\text{Os}_3\text{O}_{11}$ was $9.7 \text{ mJ mol-Os}^{-1} \text{ K}^{-2}$, which was much larger than the observed γ for $\text{Bi}_{2.93}\text{Os}_3\text{O}_{11}$ [$1.6(2) \text{ mJ mol-Os}^{-1} \text{ K}^{-2}$]. This disagreement between the expected and observed γ for the compounds is possibly owing to a steep change of DOS in the vicinity of E_F with lowering the Bi stoichiometry. This phenomenon has been previously discussed for related Os oxides [41]. Although we needed to carefully investigate possible contributions from spin-polarization and spin-orbit interactions over the DOS structure, opening a full gap at E_F for $\text{Bi}_{2.93}\text{Os}_3\text{O}_{11}$ seemed unlikely.

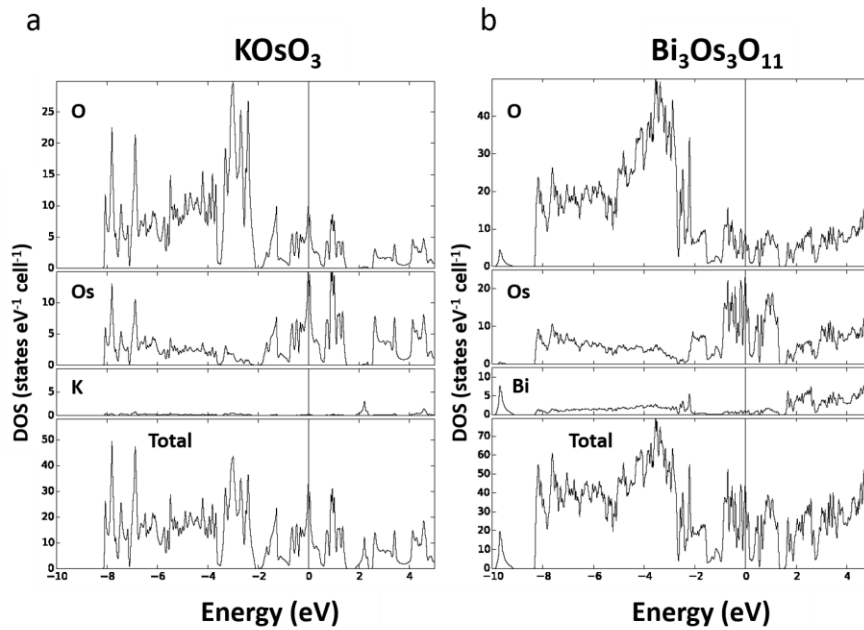


Figure 3.6. Electronic DOS of stoichiometric hosts of (a) $\text{K}_{0.84}\text{OsO}_3$ and (b) $\text{Bi}_{2.93}\text{Os}_3\text{O}_{11}$. The vertical line indicates the locations of E_F .

3.8 Conclusion

Materials with $5d$ electrons might show characteristic features owing to radially extended valence orbitals and large spin-orbit couplings of $5d$ electrons over $3d$ electrons. For example, a perovskite-type oxide, NaOsO_3 , showed a Slater-like transition [30], [31] and a LiNbO_3 -type oxide, LiOsO_3 , showed a ferroelectric-like transition in the metallic state [29]. The results led to the reasonable expectation that KO_3 , if synthesized, also showed characteristic features of $5d$ electrons. Nevertheless, KSbO_3 -type crystalline $\text{K}_{0.84}\text{OsO}_3$ showed only a weak temperature-dependent paramagnetic feature. In addition, KSbO_3 -type $\text{Bi}_{2.93}\text{Os}_3\text{O}_{11}$ was also synthesized under high-pressure and high-temperature conditions. The Os–O network in this system was found to form a similar tunnel motif to that of $\text{K}_{0.84}\text{OsO}_3$. Although the formal valence of Os decreased from +5.16 (K) to +4.40 (Bi), the observed magnetic and electronic properties did not change significantly.

In contrast to the remarkable $5d$ properties of related compounds NaOsO_3 [29], [30] and LiOsO_3 [29], $\text{K}_{0.84}\text{OsO}_3$ and $\text{Bi}_{2.93}\text{Os}_3\text{O}_{11}$ seemed to have less characteristic $5d$ properties above 2 K. Both compounds showed rather weak temperature-dependent paramagnetism and metallic transports. Disorders such as K/Bi vacancies and the polycrystalline nature of the compounds (including grain boundaries and impurities) could possibly complicate the observed $5d$ properties. Nevertheless, the magnetic and electronic properties were quite similar to what was observed for structurally relevant $5d$ oxides, including $\text{Bi}_3\text{Re}_3\text{O}_{11}$ ($\text{Re}^{4.33+}$; $5d^{2.66}$) [18] and $\text{Ba}_2\text{Ir}_3\text{O}_9$ ($\text{Ir}^{4.66+}$; $5d^{4.33}$) [26], regardless of the number of $5d$ electrons. The absence of a long-range magnetic order seemed to be common among the tunnel-like structures of $5d$ oxides. Further studies on high-quality single crystals of newly synthesized KSbO_3 -type material $\text{K}_{0.84}\text{OsO}_3$ might reveal the $5d$ characteristic features and help establish a comprehensive picture of the $5d$ electronic system.

References in chapter 3

- [1] J. B. Goodenough and J. A. kafalas, "Exploring the $A^+B^{5+}O_3$ compounds," *J. Solid State Chem.*, vol. 6, no. 4, pp. 493–501, Apr. 1973.
- [2] J. B. Goodenough and K.-S. Park, "The Li-Ion Rechargeable Battery: A Perspective," *J. Am. Chem. Soc.*, vol. 135, no. 4, pp. 1167–1176, Jan. 2013.
- [3] L. He, J. R. Anderson, H. F. Franzen, and D. C. Johnson, "Electrocatalysis of Anodic Oxygen-Transfer Reactions: $Bi_3Ru_3O_{11}$ Electrodes in Acidic Media," *Chem. Mater.*, vol. 9, no. 3, pp. 715–722, Mar. 1997.
- [4] T. N. Nguyen, D. M. Giaquinta, W. M. Davis, and H. C. zur Loye, "Electrosynthesis of $KBiO_3$ (potassium bismuth oxide): a potassium ion conductor with the $KSbO_3$ (potassium antimony oxide) tunnel structure," *Chem. Mater.*, vol. 5, no. 9, pp. 1273–1276, Sep. 1993.
- [5] D.-Y. Jung, P. Han, S. R. Wilson, and D. A. Payne, "Electrochemical synthesis of single-crystal $(Ba_{0.05}K_{0.95})BiO_{3.4}/6H_2O$ with the $KSbO_3$ structure," *Mater. Res. Bull.*, vol. 33, no. 8, pp. 1195–1205, Aug. 1998.
- [6] A. W. Sleight and R. J. Bouchard, "New cubic potassium antimony oxide derivative structure with interpenetrating networks. Crystal structure of bismuth gallium antimony oxide," *Inorg. Chem.*, vol. 12, no. 10, pp. 2314–2316, Oct. 1973.
- [7] P. Khalifah and R. J. Cava, "Metal-metal bonding in the $KSbO_3$ -type oxides $La_4Ru_6O_{19}$ and $La_3Ru_3O_{11}$ A mechanism for band gap formation in t_{2g} states," *Phys. Rev. B*, vol. 64, no. 8, p. 085111, Aug. 2001.
- [8] P. Khalifah, K. D. Nelson, R. Jin, Z. Q. Mao, Y. Liu, Q. Huang, X. P. A. Gao, A. P. Ramirez, and R. J. Cava, "Non-Fermi-liquid behaviour in $La_4Ru_6O_{19}$," *Nature*, vol. 411, no. 6838, pp. 669–671, Jun. 2001.
- [9] R. Hoppe and K. Claes, "Information on $KIrO_3$," *Journal of the less-common metals*, vol. 43, no. 1, pp. 129–142, 1975.
- [10] R. F. Sarkozy and B. L. Chamberland, "The preparation of several new ternary

- oxides of osmium,” *Mater. Res. Bull.*, vol. 8, no. 12, pp. 1351–1359, Dec. 1973.
- [11] S. Kodialam, V. C. Korthius, R.-D. Hoffmann, and A. W. Sleight, “Electrodeposition of potassium bismuthate: KBiO_3 ,” *Mater. Res. Bull.*, vol. 27, no. 12, pp. 1379–1384, Dec. 1992.
- [12] R. Sharma, T. K. Mandal, K. Ramesha, and J. Gopalakrishnan, “Synthesis and Characterization of AgBiO_3 with the Cubic KSbO_3 Structure.,” *ChemInform*, vol. 35, no. 13, p. no–no, Mar. 2004.
- [13] F. Abraham, J. Trehoux, D. Thomas, and F. E. Wagner, “Propriétés électriques, magnétiques et de résonance Mössbauer de $\text{La}_3\text{Ir}_3\text{O}_{11}$,” *J. Common Met.*, vol. 84, pp. 245–251, Mar. 1982.
- [14] F. A. Cotton and C. E. Rice, “The crystal structure of $\text{La}_3\text{Ru}_3\text{O}_{11}$: A new cubic KSbO_3 derivative oxide with no metal-metal bonding,” *J. Solid State Chem.*, vol. 25, no. 2, pp. 137–142, Jun. 1978.
- [15] A. W. Sleight, “New ternary oxides of Re, Os, Ir and Pt with cubic crystal structures,” *Mater. Res. Bull.*, vol. 9, no. 9, pp. 1177–1184, Sep. 1974.
- [16] T. Fujita, K. Tsuchida, Y. Yasui, Y. Kobayashi, and M. Sato, “Transport, thermal and magnetic properties of $\text{Bi}_3\text{Os}_3\text{O}_{11}$ and $\text{Bi}_3\text{Ru}_3\text{O}_{11}$,” *Phys. B Condens. Matter*, vol. 329–333, Part 2, pp. 743–744, May 2003.
- [17] M.-R. Li, M. Retuerto, Y. Bok Go, T. J. Emge, M. Croft, A. Ignatov, K. V. Ramanujachary, W. Dachraoui, J. Hadermann, M.-B. Tang, J.-T. Zhao, and M. Greenblatt, “Synthesis, crystal structure, and properties of KSbO_3 -type $\text{Bi}_3\text{Mn}_{1.9}\text{Te}_{1.1}\text{O}_{11}$,” *J. Solid State Chem.*, vol. 197, pp. 543–549, Jan. 2013.
- [18] H. Suzuki, H. Ozawa, and H. Sato, “Anomalous Electric Conductions in KSbO_3 -Type Metallic Rhenium Oxides,” *J. Phys. Soc. Jpn.*, vol. 76, no. 4, p. 044805, Apr. 2007.
- [19] K. Ramesha, A. S. Prakash, M. Sathiya, G. Madras, and A. K. Shukla, “Synthesis of new $(\text{Bi}, \text{La})_3\text{MSb}_2\text{O}_{11}$ phases ($\text{M} = \text{Cr}, \text{Mn}, \text{Fe}$) with KSbO_3 -type structure and their magnetic and photocatalytic properties,” *Bull. Mater. Sci.*, vol. 34, no. 2, pp.

271–277, Aug. 2011.

- [20] J.-C. Champarnaud-Mesjard, B. Frit, A. Aftati, and M. El Farissi, “ChemInform Abstract: $\text{NaBi}_2\text{Sb}_3\text{O}_{11}$: An Ordered Structure Related to the Cubic KSbO_3 Type.,” *ChemInform*, vol. 27, no. 14, p. no–no, Aug. 2010.
- [21] J. R. Plaisier, R. A. G. de Graaff, and D. J. W. Ijdo, “Structure determination of $\text{Ba}_4\text{Os}_6\text{O}_{18}\text{Cl}$,” *Mater. Res. Bull.*, vol. 31, no. 3, pp. 279–282, Mar. 1996.
- [22] P. Roussel, L. Palatinus, F. Belva, S. Daviero-Minaud, O. Mentre, and M. Huve, “ $\text{Sr}_4\text{Ru}_6\text{ClO}_{18}$, a new $\text{Ru}^{4+/5+}$ oxy-chloride, solved by precession electron diffraction: Electric and magnetic behavior,” *J. Solid State Chem.*, vol. 212, pp. 99–106, Apr. 2014.
- [23] A. A. Belik and E. Takayama-Muromachi, “Effects of Oxygen Content on $\text{Bi}_3\text{Mn}_3\text{O}_{11+\delta}$: From 45 K Antiferromagnetism to Room-Temperature True Ferromagnetism,” *J. Am. Chem. Soc.*, vol. 132, no. 35, pp. 12426–12432, Sep. 2010.
- [24] A. A. Belik and E. Takayama-Muromachi, “ $\text{Bi}_3\text{Mn}_3\text{O}_{11}$: A New KSbO_3 -Type Random Ferrimagnet with High TC,” *J. Am. Chem. Soc.*, vol. 131, no. 27, pp. 9504–9505, Jul. 2009.
- [25] J. Cheng, A. J. E. Rettie, M. R. Suchomel, H. Zhou, J. Yan, J. Song, L. G. Marshall, S. A. Larregola, J. Zhou, and J. B. Goodenough, “High-Pressure Synthesis, Structure, and Photoluminescence of a New KSbO_3 -Type Bismuth Germanate $\text{Bi}_3\text{Ge}_3\text{O}_{10.5}$,” *Inorg. Chem.*, vol. 52, no. 4, pp. 2138–2141, Feb. 2013.
- [26] Y. Kawamura and H. Sato, “ $\text{Ba}_2\text{Ir}_3\text{O}_9$: a new 5d mixed-valence metallic oxide with KSbO_3 -type structure,” *J. Alloys Compd.*, vol. 383, no. 1–2, pp. 209–212, Nov. 2004.
- [27] W. Yi, Y. Matsushita, A. Sato, K. Kosuda, M. Yoshitake, and A. A. Belik, “ $\text{Bi}_3\text{Cr}_{2.91}\text{O}_{11}$: A Ferromagnetic Insulator from $\text{Cr}^{4+}/\text{Cr}^{5+}$ Mixing,” *Inorg. Chem.*, vol. 53, no. 16, pp. 8362–8366, Aug. 2014.
- [28] H. L. Feng, M. Arai, Y. Matsushita, Y. Tsujimoto, Y. Guo, C. I. Sathish, X. Wang, Y.-H. Yuan, M. Tanaka, and K. Yamaura, “High-Temperature Ferrimagnetism

- Driven by Lattice Distortion in Double Perovskite $\text{Ca}_2\text{FeOsO}_6$,” *J. Am. Chem. Soc.*, vol. 136, no. 9, pp. 3326–3329, Mar. 2014.
- [29] Y. Shi, Y. Guo, X. Wang, A. J. Princep, D. Khalyavin, P. Manuel, Y. Michiue, A. Sato, K. Tsuda, S. Yu, M. Arai, Y. Shirako, M. Akaogi, N. Wang, K. Yamaura, and A. T. Boothroyd, “A ferroelectric-like structural transition in a metal,” *Nat. Mater.*, vol. 12, no. 11, pp. 1024–1027, Nov. 2013.
- [30] S. Calder, V. O. Garlea, D. F. McMorrow, M. D. Lumsden, M. B. Stone, J. C. Lang, J.-W. Kim, J. A. Schlueter, Y. G. Shi, K. Yamaura, Y. S. Sun, Y. Tsujimoto, and A. D. Christianson, “Magnetically Driven Metal-Insulator Transition in NaOsO_3 ,” *Phys. Rev. Lett.*, vol. 108, no. 25, p. 257209, Jun. 2012.
- [31] Y. G. Shi, Y. F. Guo, S. Yu, M. Arai, A. A. Belik, A. Sato, K. Yamaura, E. Takayama-Muromachi, H. F. Tian, H. X. Yang, J. Q. Li, T. Varga, J. F. Mitchell, and S. Okamoto, “Continuous metal-insulator transition of the antiferromagnetic perovskite NaOsO_3 ,” *Phys. Rev. B*, vol. 80, no. 16, p. 161104, Oct. 2009.
- [32] Y. Kanke, M. Akaishi, S. Yamaoka, and T. Taniguchi, “Heater cell for materials synthesis and crystal growth in the large volume high pressure apparatus at 10 GPa,” *Rev. Sci. Instrum.*, vol. 73, no. 9, pp. 3268–3270, Sep. 2002.
- [33] M. Tanaka, Y. Katsuya, and A. Yamamoto, “A new large radius imaging plate camera for high-resolution and high-throughput synchrotron x-ray powder diffraction by multiexposure method,” *Rev. Sci. Instrum.*, vol. 79, no. 7, p. 075106, Jul. 2008.
- [34] F. Izumi and K. Momma, “Three-Dimensional Visualization in Powder Diffraction,” *Solid State Phenom.*, vol. 130, pp. 15–20, 2007.
- [35] J. P. Perdew, K. Burke, and M. Ernzerhof, “Generalized Gradient Approximation Made Simple,” *Phys. Rev. Lett.*, vol. 77, no. 18, pp. 3865–3868, Oct. 1996.
- [36] P. Blaha, K. Schwarz, G. K. H. Madsen, D. Kvasnicka, and J. Luitz, “WIEN2k, An Augmented Plane Wave+ Local Orbitals Program for Calculating Crystal Properties; Technische Universität Wien, Wien, 2001,” *There No Corresp. Rec. This*

- Ref.*, 2002.
- [37] R. D. Shannon, "Revised effective ionic radii and systematic studies of interatomic distances in halides and chalcogenides," *Acta Crystallogr. Sect. A*, vol. 32, no. 5, pp. 751–767, Sep. 1976.
- [38] J.-I. Yamaura, S. Yonezawa, Y. Muraoka, and Z. Hiroi, "Crystal structure of the pyrochlore oxide superconductor $\text{KO}_8\text{S}_2\text{O}_6$," *J. Solid State Chem.*, vol. 179, no. 1, pp. 336–340, Jan. 2006.
- [39] K., Ismunandar Brendan J. and B. A. Hunter, "Temperature dependent neutron powder diffraction study of $\text{Bi}_3(\text{GaSb}_2)\text{O}_{11}$," *Solid State Commun.*, vol. 108, no. 9, pp. 649–654, Nov. 1998.
- [40] M. Brühwiler, S. M. Kazakov, J. Karpinski, and B. Batlogg, "Mass enhancement, correlations, and strong-coupling superconductivity in the β -pyrochlores $\text{KO}_8\text{S}_2\text{O}_6$," *Phys. Rev. B*, vol. 73, no. 9, p. 094518, Mar. 2006.
- [41] Y. Shi, Y. Guo, Y. Shirako, W. Yi, X. Wang, A. A. Belik, Y. Matsushita, H. L. Feng, Y. Tsujimoto, M. Arai, N. Wang, M. Akaogi, and K. Yamaura, "High-Pressure Synthesis of 5d Cubic Perovskite BaOsO_3 at 17 GPa: Ferromagnetic Evolution over 3d to 5d Series," *J. Am. Chem. Soc.*, vol. 135, no. 44, pp. 16507–16516, Nov. 2013.

Chapter 4. Crystal structures, and magnetic properties of 5d double-perovskite oxides $\text{Ca}_2\text{MgOsO}_6$ and $\text{Sr}_2\text{MgOsO}_6$

4.1 Background knowledge

4.1.1 Double perovskite overview

Recently, double-perovskite oxides have attracted renewed attention, because they exhibited properties that may be useful for possible applications such as in, for example, multifunctional devices [1]. Generally, stoichiometric $A_2BB'O_6$, wherein A denoted an alkaline earth (or rare-earth) metal and B and B' were d-block elements (or other metals), crystallizes in a cubic, tetragonal, or monoclinic double-perovskite structure with interpenetrating B and B' face-centered cubic (FCC) sublattices. When B and B' were both magnetic, interactions between the FCC cells resulted in useful magnetic features such as high spin-polarization at ambient temperature in $\text{Sr}_2\text{FeMoO}_6$ [2], remarkable high-temperature (~ 725 K) ferrimagnetism in $\text{Sr}_2\text{CrOsO}_6$ [3], unusual competing spin structure in $\text{Sr}_2\text{FeOsO}_6$ [4], chemical-pressure-induced high-temperature ferrimagnetism in $\text{Ca}_2\text{FeOsO}_6$ [5], and the coexistence of two independent magnetic orders in $\text{Sr}_2\text{CoOsO}_6$ [6]–[8]. These properties might be useful for developing advanced multifunctional devices; however, further clarification of the responsible mechanism was necessary. At present, the role of 5d electrons and the impact of interactions between 5d(or 4d) and 3d electrons on the properties were emerging issues.

When B was nonmagnetic and B' is magnetic, or vice versa, a single magnetic FCC sublattice was formed. The double perovskites containing single magnetic sublattices might be useful for investigating the emerging issues. They all displayed only antiferromagnetic characters with moderate magnetic interactions, as the distances between the nearest-neighbor magnetic elements were much longer than 5 Å. Indeed, they showed long-range antiferromagnetic ordering at most 74 K or below (see **Table 4.1**). Some of them showed geometrically frustrated magnetic properties, probably

because the FCC sublattices formed an edge-shared tetrahedra (B'_4), in which B' atoms were mutually connected via antiferromagnetic bonds such as $-B'-O-O-B'-$ [9]. For example, the effect of geometrical frustration on magnetism has been argued for Sr_2BReO_6 ($B = Ca, Mg$) [9], [10], La_2LiReO_6 and Ba_2YReO_6 [11].

4.1.2 Double perovskite with a single magnetic sublattice

In this chapter, we synthesized double-perovskite oxides Ca_2MgOsO_6 and Sr_2MgOsO_6 , which have single magnetic sublattices, and we investigated their crystal structures and magnetic properties. The synthesis of Sr_2MgOsO_6 was initially reported by Sleight *et al.* in 1962 [12]; however, to the best of our knowledge, details of its magnetic properties were not known to date. Ca_2MgOsO_6 was a new compositional oxide. We found that the magnetic properties of Ca_2MgOsO_6 and Sr_2MgOsO_6 were very different, despite the fact that they were isoelectronic and have a similar structural basis. Sr_2MgOsO_6 showed an antiferromagnetic transition at ~ 110 K, while Ca_2MgOsO_6 showed a magnetic-glass transition at ~ 19 K and did not show any long-rang antiferromagnetic ordering above 2 K.

It appeared that the magnetic-glass state, probably reflecting the freezing of the magnetic frustration, transforms into an antiferromagnetically ordered state upon the substitution of Sr for Ca. The change in magnetic character was the most noticeable for double-perovskite oxides containing single magnetic sublattices, because the antiferromagnetic-transition temperature was the highest (**Table 4.1**). A first-principles density functional approach indicated that Ca_2MgOsO_6 and Sr_2MgOsO_6 were likely to be $5d$ antiferromagnetic Mott insulators with Coulomb correlations of approximately 1.8-3.0 eV. These compounds provided an opportunity for studying the antiferromagnetic nature of the sublattices of $5d$ magnetic double-perovskite oxides with regards to the possible use of such oxides in multifunctional devices.

In addition, Ba_2BReO_6 ($B = Mg, Zn, Cd, Ca, Sr, Ba, Sc$), Ba_2BOsO_6 ($B = Mg, Zn, Cd, Sr, Ba, Sc$), Sr_2BReO_6 ($B = Zn, Cd, Sr, Sc$), Sr_2BOsO_6 ($B = Li, Na, Ca, Sr, Sc$), Ca_2BReO_6 ($B = Mg, Cd, Ca, Sc$), Ca_2LiOsO_6 , and X_2MlIrO_6 ($X = Ba/Sr, M = Ca, Sr, Mg, Zn, La$) were probably synthesized, although the refined structure parameters and

detailed magnetic properties were not reported [12]–[16]. $\text{Ba}_2\text{Fe}^{2+}\text{MoO}_6$ and $\text{Ba}_2\text{Fe}^{2+}\text{WO}_6$ were synthesized and weak ferrimagnetic-like characters were observed; however, an impact from the magnetic impurities on the properties and relevance to the site-disorder were argued [13]. $\text{Ca}_2\text{Pd}^{2+}\text{WO}_6$ [14] and $\text{SrLaMRu}^{5+}\text{O}_6$ ($M = \text{Zn}, \text{Mg}$) [15] were synthesized; but no magnetic properties were reported. The d^0 and d^6 (low-spin state) compounds were not included. $T_{\text{N,f}}$ denotes either an ordering or freezing temperature of magnetism. μ_{eff} and θ_{W} were the effective magnetic moment and Weiss temperature of the Curie-Weiss law, respectively.

Table 4.1 Double perovskite oxide with a single magnetic sublattice.

d electron count, composition, space group	Lattice parameters	Magnetic parameters				Note	Ref.	
		$T_{\text{N,f}}$ (K)	θ_{W} (K)	$ \theta_{\text{W}}/T_{\text{N,f}} $	μ_{eff} (μ_{B})			
3d double-perovskite oxides								
d^3	$\text{La}_2\text{LiFe}^{5+}\text{O}_6$ <i>R-3c</i>	$a = 5.371$ $\alpha = 60.66$	10	-90	9	3.93	High-pressure heating, 900 °C	13
d^5	$\text{LaBaMn}^{2+}\text{NbO}_6$		6.5	-39	6.0			14
d^5	$\text{LaSrMn}^{2+}\text{NbO}_6$ <i>P2₁/n</i>	$a = 5.6918(7)$ $b = 5.7473(2)$ $c = 8.0701(8)$ $\beta = 90.050(4)$	8.5	-35.7	4.2	5.76	Solid-state reaction, 1275 °C	15
d^5	$\text{LaCaMn}^{2+}\text{NbO}_6$		9	-44.1	4.9			14
d^5	$\text{Ba}_2\text{Mn}^{2+}\text{WO}_6$ <i>Fm3m</i>	$a = 8.1985(3)$	45	-64.4	1.4	5.85	Solid-state reaction, 1250 °C	16
d^5	$\text{Sr}_2\text{Mn}^{2+}\text{WO}_6$ <i>P4₂/n</i>	$a = 8.0119(4)$ $c = 8.0141(8)$	13	-71.3	5.5	5.69	Solid-state reaction, 1340 °C	17
d^5	$\text{Ca}_2\text{Mn}^{2+}\text{WO}_6$ <i>P2₁/n</i>	$a = 5.4617(1)$ $b = 5.6545(1)$ $c = 7.8022(3)$	45	-61.8	1.4	4.72	Solid-state reaction, 1340 °C	18
d^5	$\text{Ba}_2\text{Mn}^{2+}\text{MoO}_6$ <i>Fm-3m</i>	$a = 8.1680(1)$	<10	-94	7.8	5.80	Solid-state reaction, 1400 °C	19
d^5	$\text{Sr}_2\text{Mn}^{2+}\text{MoO}_6$ <i>P4₂/n</i>	$a = 7.9575(5)$ $c = 7.9583(9)$	<10	-108	7.2	4.5	Solid-state reaction, 1400 °C	19
d^6	$\text{Sr}_2\text{Fe}^{2+}\text{WO}_6$ <i>P2₁/n</i>	$a = 5.6480(4)$ $b = 5.6088(4)$ $c = 7.9362(6)$ $\beta = 89.99(2)$	37	-21.3	0.6	6.58	Solid-state reaction, 1100 °C	20
d^7	$\text{Ba}_2\text{Co}^{2+}\text{WO}_6$ <i>Fm-3m</i>	$a = 8.103(0)$	18(1)	-41(2)	2.3	5.18(1)	Solid-state reaction, 1150 °C	21
d^7	$\text{Sr}_2\text{Co}^{2+}\text{WO}_6$ <i>I4/m</i>	$a = 5.5827(7)$ $c = 7.9774(0)$	24(1)	-57(2)	2.4	5.07(1)	Solid-state reaction, 1150 °C	21
d^7	$\text{Ca}_2\text{Co}^{2+}\text{WO}_6$ <i>P2₁/n</i>	$a = 5.4247(6)$ $b = 5.5786(0)$	33(1)	-68(2)	2.1	5.14(1)	Solid-state reaction, 1150 °C	21

d^7	LaCaCo ²⁺ NbO ₆ <i>P2₁/n</i>	$c = 7.7134(1)$ $\beta = 90.24(5)$ $a = 5.5509(1)$ $b = 5.6555(1)$ $c = 7.8909(1)$	17	-61(1)	3.6	5.65(3)	Flux method, 600 °C	14
d^7	Sr ₂ Co ²⁺ TeO ₆ <i>P2₁/n</i>	$\beta = 89.860(2)$ $a = 5.6417(2)$ $b = 5.6063(2)$ $c = 7.9234(2)$	15	-146(21)	9.7	5.48(2)	Solid-state reaction, 800 °C	22
d^7	La ₂ Co ²⁺ TiO ₆ <i>P2₁/n</i>	$\beta = 90.117(4)$ $a = 5.5621(7)$ $b = 5.5667(7)$ $c = 7.8502(8)$	25	-45	1.8	5.06	“Liquid mix” technique, 800-900 °C	23
d^8	Ba ₂ Ni ²⁺ WO ₆ <i>Fm-3m</i>	$\beta = 89.86(1)$ $a = 8.066(0)$	48	-120	2.5		floating-zone method, 1400 °C	24
d^8	Sr ₂ Ni ²⁺ WO ₆ <i>I4/m</i>	$a = 5.5557(1)$ $c = 7.9131(1)$	54	-175	3.2	3.05	Solid-state reaction, 1400 °C	25
d^8	Ca ₂ Ni ²⁺ WO ₆ <i>P2₁/n</i>	$a = 5.4061(2)$ $b = 5.5389(2)$ $c = 7.6895(3)$ $\beta = 90.232(2)$	52.5	-75(1)	1.4	2.85	Solid-state reaction, 1150 °C	26
d^8	La ₂ Ni ²⁺ TiO ₆ <i>P2₁/n</i>	$a = 5.5545(6)$ $b = 5.5512(5)$ $c = 7.8341(8)$ $\beta = 90.08(2)$	25	-60	2.4	3.12	“Liquid mix” technique, 800-900 °C	23

4d double-perovskite oxides

d^1	Ba ₂ YMoO ₆ <i>Fm-3m</i>	$a = 8.3920(7)$	<2	-45		1.42	Solid-state reaction, 1300 °C	27
d^1	La ₂ LiMoO ₆ <i>P2₁/n</i>	$a = 5.5939(2)$ $b = 5.6924(2)$ $c = 7.8803(2)$ $\beta = 90.260(3)$	<2	-219(1)		1.72	Solid-state reaction, 1100 °C	27
d^3	La ₂ LiRu ⁵⁺ O ₆ <i>P2₁/n</i>	$a = 5.5555(2)$ $b = 5.5977(2)$ $c = 7.8454(3)$ $\beta = 90.020(5)$	24	-185(5)	7.7	3.93	Solid-state reaction, 900 °C	28-29
d^3	La ₂ NaRu ⁵⁺ O ₆ <i>P2₁/n</i>	$a = 5.5903(3)$ $b = 5.9241(3)$ $c = 7.9990(3)$ $\beta = 90.495(2)$	16	-67	4.2	3.75	Acidic molten method, 600 °C	30
d^3	Sr ₂ LuRu ⁵⁺ O ₆ <i>P2₁/n</i>	$a = 5.7400(1)$ $b = 5.7375(1)$ $c = 8.1118(2)$ $\beta = 90.16(1)$	30(1)	-353(7)	12	3.9(1)	Solid-state reaction, 1350 °C	31
d^3	Ba ₂ YRu ⁵⁺ O ₆ <i>Fm-3m</i>	$a = 8.3356(1)$	36	-571(3)	16	4.64	Solid-state reaction, 1350 °C	28,31
d^3	Ba ₂ LuRu ⁵⁺ O ₆ <i>Fm-3m</i>	$a = 8.2720(4)$	35(1)	-630(9)	18	4.4(1)	Solid-state reaction, 1300 °C	31

5d double-perovskite oxides

d^1	Ba ₂ LiOs ⁷⁺ O ₆ <i>Fm-3m</i>	$a = 8.1046(2)$	8	-40.48	5.1	0.733	Molten fluxes hydroxide method, 600 °C	32
d^1	Ba ₂ NaOs ⁷⁺ O ₆ <i>Fm-3m</i>	$a = 8.2870(3)$	8	-32.45	4.1	0.677	Molten fluxes hydroxide method, 600 °C	32

d^1	$\text{Sr}_2\text{CaRe}^{6+}\text{O}_6$ $P2_1/n$	$a = 5.7582(3)$ $b = 5.8346(3)$ $c = 8.1787(4)$ $\beta = 90.245(3)$	14	-443	32	1.659(6)	Solid state reaction, 900 °C	9
d^1	$\text{Sr}_2\text{MgRe}^{6+}\text{O}_6$ $I4/m$	$a = 5.5670(1)$ $c = 7.9318(2)$	50	-426(58)	8.5	1.72(9)	Solid state reaction, 900 °C	10
d^2	$\text{Ca}_3\text{Os}^{6+}\text{O}_6$ $P2_1/n$	$a = 5.5403(3)$ $b = 5.8049(3)$ $c = 7.9761(4)$ $\beta = 90.020(2)$	50	-151	3.0	1.99	High-pressure flux method, 1400 °C	33
d^2	$\text{Ba}_2\text{CaOs}^{6+}\text{O}_6$ $Fm3m$	$a = 8.3619(6)$	50	-156.2(3)	3.1	1.64	Solid state reaction, 1000 °C	34-35
d^2	$\text{Sr}_2\text{MgOs}^{6+}\text{O}_6$ $I4/m$	$a = 5.56057(1)$ $c = 7.92119(2)$	110	-347.3(5)	3.2	1.867(4)	High-pressure solid state reaction, 1500 °C	This work
d^2	$\text{Ca}_2\text{MgOs}^{6+}\text{O}_6$ $P2_1/n$	$a = 5.40965(2)$ $b = 5.54033(2)$ $c = 7.69908(3)$ $\beta = 90.0481(4)$	12	-71.5(7)	6.0	1.874(4)	High-pressure solid state reaction, 1500 °C	This work
d^2	$\text{Ba}_2\text{YRe}^{5+}\text{O}_6$ $Fm-3m$	$a = 8.36278(2)$	50	-616(7)	12	2.105	Solid-state reaction, 1300 °C	11
d^2	$\text{La}_2\text{LiRe}^{5+}\text{O}_6$ $P2_1/n$	$a = 5.5826(2)$ $b = 5.6758(2)$ $c = 7.8859(3)$ $\beta = 90.240(4)$	50	-204(2)	4.1	1.97	Solid-state reaction, 900 °C	11
d^3	$\text{La}_2\text{NaOs}^{5+}\text{O}_6$ $P2_1/n$	$a = 5.6054(3)$ $b = 5.9445(3)$ $c = 8.0085(4)$ $\beta = 90.587(2)$	17	-74	4.4	3.26	Acidic molten method, 600 °C	36
d^3	$\text{Ba}_2\text{YOs}^{5+}\text{O}_6$ $Fm-3m$	$a = 8.3541(4)$	69	-772	11	4.15(1)	Solid-state reaction, 1400 °C	37
d^3	$\text{Sr}_2\text{ZnIr}^{6+}\text{O}_6$ $P2_1/n$	$a = 5.6216(1)$ $b = 5.5856(1)$ $c = 7.9052(2)$ $\beta = 89.990(1)$	46	-430	9.3	3.82	Citrate-nitrate method, 900 °C	38
d^3	$\text{Sr}_2\text{CaIr}^{6+}\text{O}_6$ $P2_1/n$	$a = 5.7668(2)$ $b = 5.8160(2)$ $c = 8.1766(3)$ $\beta = 89.721(1)$	58	-363(1)	6.3	3.43	Citrate-nitrate method, 950 °C in 200 bar oxygen pressure	39
d^3	$\text{Sr}_2\text{MgIr}^{6+}\text{O}_6$ $P2_1/n$	$a = 5.5909(8)$ $b = 5.5754(6)$ $c = 7.8839(8)$ $\beta = 89.906(1)$	74	-418(1)	5.6	2.12	Citrate-nitrate method, 800 °C in 200 bar oxygen pressure	40-41
d^3	$\text{Ba}_2\text{CaIr}^{6+}\text{O}_6$ $Fm-3m$	$a = 8.3567(3)$	55	-1250	23	5.98	Solid-state reaction, 950 °C	40-41
d^3	$\text{Ca}_2\text{InOsO}_6$ $P2_1/n$	$a = 5.4889(3)$ $b = 5.6785(1)$ $c = 7.8576(2)$ $\beta = 89.906(1)$	14	-77	5.5	3.19	High-pressure solid state reaction, 1400 °C	42
d^4	$\text{La}_2\text{LiIr}^{5+}\text{O}_6$ $Pmm2$	$a = 5.634(3)$ $b = 5.555(3)$ $c = 7.867(5)$	<4.2	~-20		1.42	High-oxygen pressure heating, 800 °C	43-44
d^5	$\text{La}_2\text{MgIr}^{4+}\text{O}_6$ $P2_1/n$	$a = 5.5856(7)$ $b = 5.6246(6)$ $c = 7.907(1)$ $\beta = 90.03(5)$	11.7	-24	8.3	1.71	Solid-state reaction, 1150 °C	44-46
d^5	$\text{La}_2\text{ZnIr}^{4+}\text{O}_6$ $P2_1/n$	$a = 5.5986(4)$ $b = 5.6869(4)$	<7.5	-3.1		1.42	Solid-state reaction, 1100 °C	44-46

$$c = 7.9405(6)$$
$$\beta = 89.99(5)$$

4.2 Experimental details

Polycrystalline $\text{Ca}_2\text{MgOsO}_6$ and $\text{Sr}_2\text{MgOsO}_6$ were synthesized via a solid-state reaction under high-pressure conditions from powders of AO_2 ($A = \text{Ca}, \text{Sr}$; laboratory-made) [16], Os (99.95%, Heraeus Materials Technology, Germany), MgO (99.99%, Kojundo Chemical Lab. Co., Ltd., Japan), and KClO_4 (> 99.5%, Kishida Chemical Co., Ltd., Japan). The powders were thoroughly mixed in a stoichiometric ratio ($\text{AO}_2 : \text{MgO} : \text{Os} : \text{KClO}_4 = 2:1:1:0.25$) and sealed in a Pt capsule. The procedure was conducted in an Ar-filled glove box. The capsule was statically and isotropically compressed to a pressure of 6 GPa using a belt-type high-pressure apparatus (Kobe Steel, Ltd., Japan), and subsequently heated at 1500 °C for 1 h. The pressure was maintained during heating. Subsequently, the capsule was quenched to ambient temperature within a minute and the pressure was gradually released over a few hours.

A polycrystalline, dense, and well-sintered pellet was finally obtained. A small piece of the pellet was cut out, finely ground, and washed with water to remove KCl residues. The fine and black powder was dried and subjected to an X-ray diffraction (XRD) study, using an X-ray diffractometer with Cu $K\alpha$ radiation. It was then studied by synchrotron X-ray diffraction (SXRD) at ambient temperature in the BL15XU beamline facility at SPring-8. The SXRD data were collected using a large Debye-Scherrer-type diffractometer [17] and the “MYTHEN” one-dimensional semiconductor X-ray detector [18]. The radiation wavelength was confirmed to be 0.65297 Å using a reference material, viz. CeO_2 . The SXRD pattern was analyzed with the Rietveld method using the “RIETAN-VENUS” software [19], [20].

Other pieces of the pellet were subjected to electrical resistivity (ρ) and specific heat (C_p) measurements. The ρ measurements were conducted at 120-300 K using a four-point method and with a DC gauge current of 0.1 mA, in a physical properties

measurement system from Quantum Design, Inc. Electrical contacts were prepared along the longitudinal direction of the piece by attaching Pt wires using a Ag paste. The temperature dependence of C_p was also measured using the apparatus, at 2–300 K, by a thermal relaxation method. The contribution of KCl to the raw C_p data was subtracted over the studied temperature range using the tabulated data and the mass ratio (0.03837 for 0.25KCl/Sr₂MgOsO₆ and 0.04771 for 0.25KCl/Ca₂MgOsO₆) [21].

The magnetic susceptibilities (χ) of Ca₂MgOsO₆ and Sr₂MgOsO₆ were measured using the powder samples in a magnetic properties measurement system from Quantum Design, Inc. The χ measurements were conducted on a small amount of the powdered compound under field cooling (FC) and zero-field cooling (ZFC) conditions at 2-390 K, using an applied magnetic field of 10 kOe. The magnetic-field dependence of the isothermal magnetization was measured between –50 kOe and +50 kOe at 5 K.

Electronic and magnetic structural calculations were conducted with the WIEN2k package, using a full-potential linearized augmented planewave method within the density functional theory [22]. The atomic sphere radii (R_{MT}) were fixed at 2.2, 2.5, 1.92, 1.91, and 1.56 Bohr for Ca, Sr, Mg, Os, and O, respectively. A set of 200k points was used for the calculations. The standard generalized-gradient approximation (GGA) exchange-correlation potential within the Perdew-Burke-Ernzerhof (PBE)-scheme[23] was used with Coulomb interactions (U) [24] of 3 and 4 eV for Os in Ca₂MgOsO₆ and Sr₂MgOsO₆, respectively.

4.3 Crystal structures

The powder XRD pattern in **Fig. 4.1** indicated that the crystal structure of Ca₂MgOsO₆ was well characterized by a monoclinic lattice with $a \approx 5.41$ Å, $b \approx 5.54$ Å, $c \approx 7.70$ Å, and $\beta \approx 90.0^\circ$, whereas that of Sr₂MgOsO₆ was characterized by a tetragonal lattice with $a \approx 5.57$ Å and $c \approx 7.93$ Å. The lattice parameters appeared to be comparable with those of the other double-perovskite oxides with Ca and Sr, respectively (see **Table 4.1**). Because the 011 peak near $2\theta = 20^\circ$ evidences that Mg and

Os were highly ordered, the possible space group of $Pbnm$, with $\sim\sqrt{2}a_p \times \sqrt{2}a_p \times 2a_p$ (a_p was the primitive perovskite lattice parameter), was excluded [25]. The lattice features hence implied that $\text{Ca}_2\text{MgOsO}_6$ and $\text{Sr}_2\text{MgOsO}_6$ had the space groups of $P2_1/n$ and $I4/m$, respectively.

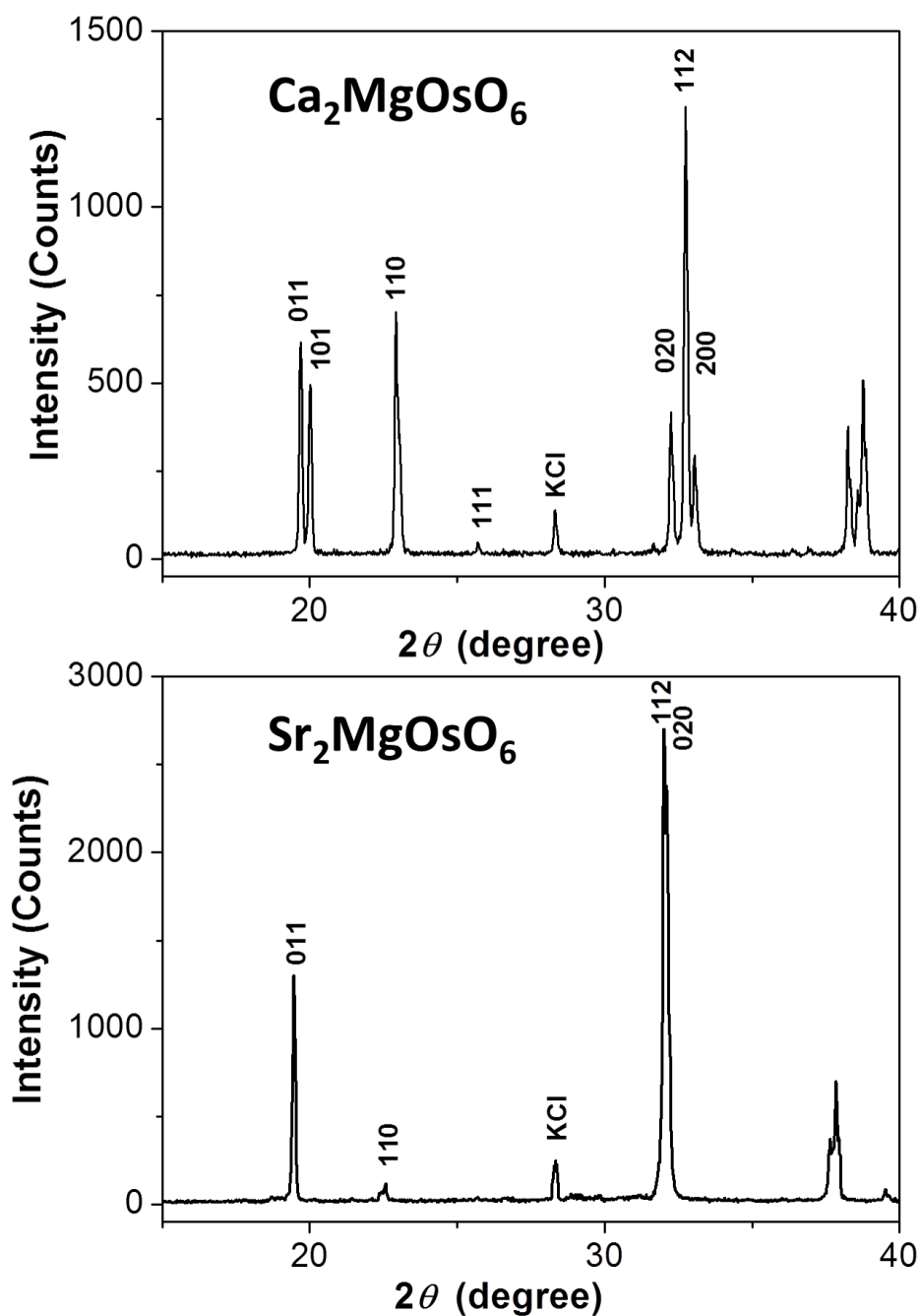


Figure 4.1 Powder XRD (Cu $K\alpha$) patterns for $\text{Ca}_2\text{MgOsO}_6$ and $\text{Sr}_2\text{MgOsO}_6$.

Crystal structure refinements for $\text{Ca}_2\text{MgOsO}_6$ and $\text{Sr}_2\text{MgOsO}_6$ were attempted with a monoclinic structure model ($P2_1/n$) for $\text{Ca}_2\text{MgOsO}_6$ and a tetragonal structure model ($I4/m$) for $\text{Sr}_2\text{MgOsO}_6$. The results of the Rietveld analyses of the SXRD patterns for $\text{Ca}_2\text{MgOsO}_6$ and $\text{Sr}_2\text{MgOsO}_6$ were shown in **Figs. 4.2(a)** and **(b)**. Eventually, reasonable results were well obtained for both; details are summarized in **Table 4.2**. The refined structures were depicted in **Figs. 4.3 (a)** and **(b)**.

During the refinements, a disorder model for Mg and Os atoms at the double-perovskite B' and B'' sites was tested. Mg and Os atoms were tentatively assumed to occupy the B' and B'' sites randomly. A reasonable result was, however, never achieved (see **Fig. 4.4** and **Table 4.3**). Therefore, we decided to refine the occupancies of Mg and Os atoms at the B' and B'' sites. Initially, the displacement parameters for all atoms were fixed at 0.5 \AA^2 at beginning; later, the displacement parameters and occupancies were refined simultaneously. The procedure was repeated until no further improvement was obtained. It appeared that the refinements for the Mg and Os occupancies substantially improved the overall refinement. A small degree of disorder of the arrangement of Mg and Os (~4%) was, however, found for $\text{Ca}_2\text{MgOsO}_6$. However, the mixing disorder was found to be minimal in $\text{Sr}_2\text{MgOsO}_6$. The finally refined structural solution indicated that, in $\text{Ca}_2\text{MgOsO}_6$ and $\text{Sr}_2\text{MgOsO}_6$, the degree of order of the Os and Mg arrangement was 96% or higher (see **Table 4.2**).

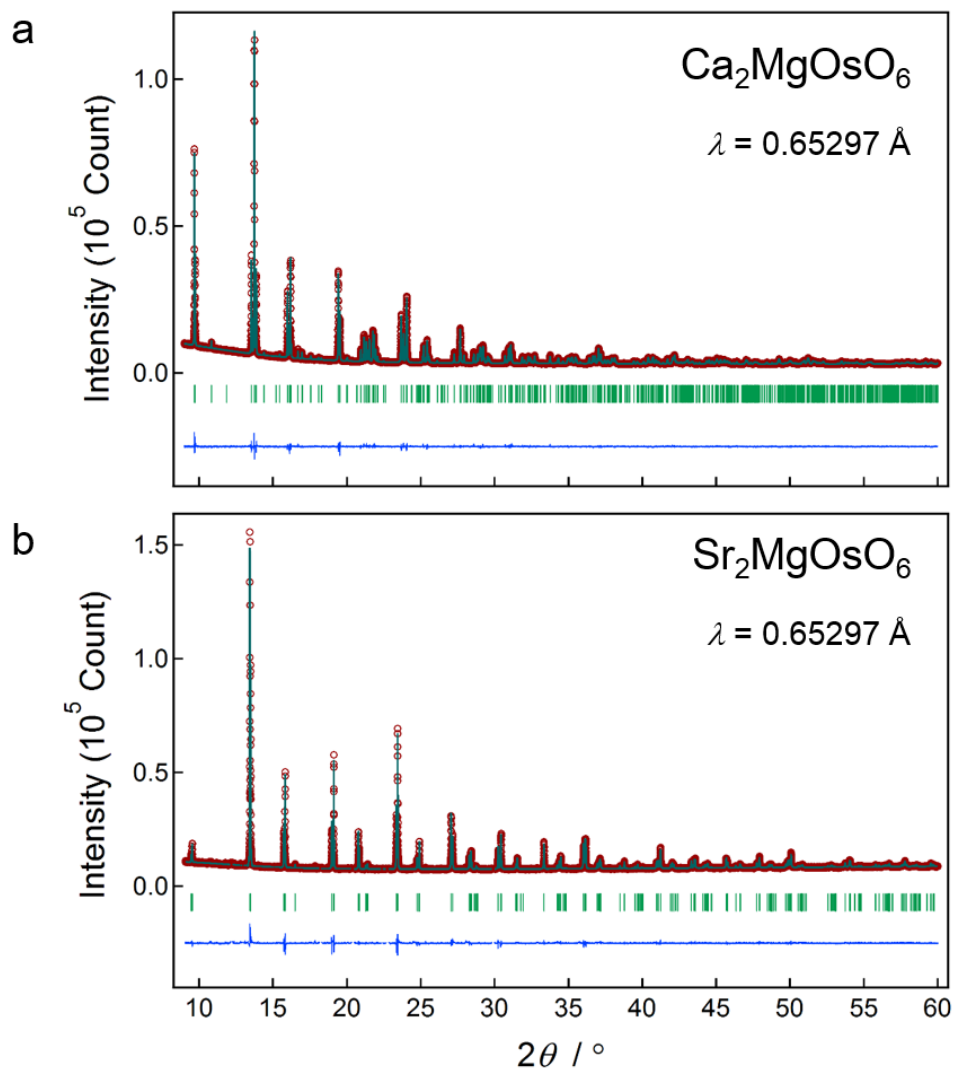


Figure 4.2 Rietveld analysis of the SXRD patterns for (a) $\text{Ca}_2\text{MgOsO}_6$ and (b) $\text{Sr}_2\text{MgOsO}_6$ at ambient temperature. Circles and solid lines showed the observed and calculated patterns, respectively, and the difference between the patterns was shown at the bottom of each figure. The expected Bragg reflections were marked by the small vertical bars.

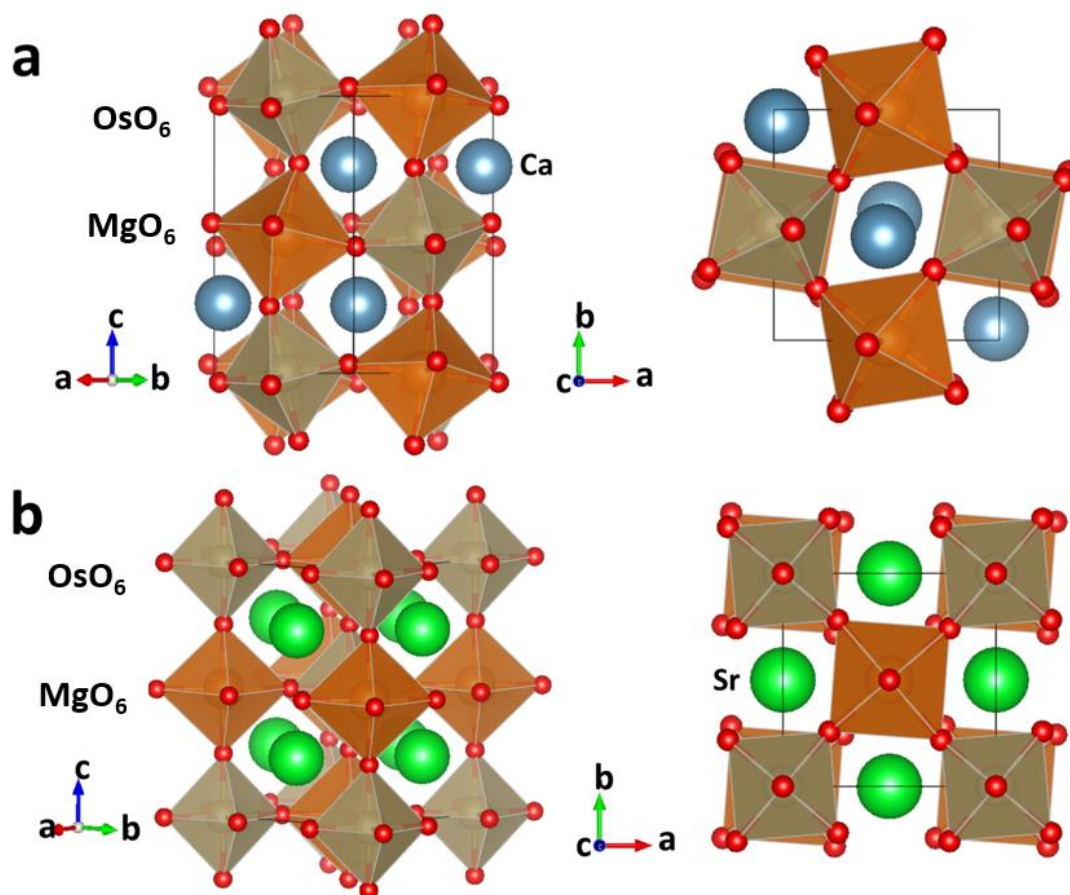


Figure 4.3 Proposed crystal structures of (a) $\text{Ca}_2\text{MgOsO}_6$ and (b) $\text{Sr}_2\text{MgOsO}_6$, in which OsO_6 and MgO_6 were drawn as octahedra (see labels in the figure). Ca and Sr atoms were drawn as large spheres as marked.

Table 4.2 Crystal structure parameters for $\text{Ca}_2\text{MgOsO}_6$ and $\text{Sr}_2\text{MgOsO}_6$ at ambient temperature.

Atom	Wyckoff Positions	Occupancy	x	y	z	$B (\text{\AA}^2)$
$\text{Ca}_2\text{MgOsO}_6$, Space group $P2_1/n$ (No. 14), $a = 5.40965(2) \text{ \AA}$, $b = 5.54033(2) \text{ \AA}$, $c = 7.69908(3) \text{ \AA}$, $\beta = 90.0481(4)^\circ$, $Z = 2$, $V = 230.75(1) \text{ \AA}^3$, and $d_{\text{cal}} = 5.622 \text{ g/cm}^3$. $R_{\text{wp}} = 2.486\%$, $R_p = 1.790\%$.						
Ca	$4e$	1	0.9857(6)	0.0492(2)	0.2532(1)	1.07(2)
Os1/Mg1	$2c$	0.96(1)/ 0.04	0.5	0	0.5	0.33(1)
Mg2/Os2	$2d$	0.96/ 0.04	0.5	0	0	0.16(1)
O1	$4e$	1	0.0851(6)	0.4801(10)	0.2419(5)	0.51(2)
O2	$4e$	1	0.7112(8)	0.3054(8)	0.0424(8)	0.63(1)
O3	$4e$	1	0.1910(9)	0.2279(8)	0.9671(10)	1.65(3)

Sr₂MgOsO₆, Space group *I4/m* (No. 87), $a = 5.56057(1)$ Å, $c = 7.92119(2)$ Å, $Z = 2$, $V = 244.92(1)$ Å³, and $d_{\text{cal}} = 6.586$ g/cm³. $R_{\text{wp}} = 2.249\%$, $R_{\text{p}} = 1.518\%$.

Sr	4 <i>d</i>	1	0.5	0	0.25	0.69(1)
Os	2 <i>a</i>	1	0	0	0	0.25(1)
Mg	2 <i>b</i>	1	0	0	0.5	0.19(1)
O1	8 <i>h</i>	1	0.2179(14)	0.2573(13)	0	1.52(1)
O2	4 <i>e</i>	1	0	0	0.2461(7)	1.49(2)

Table 4.3 Crystal structure parameters for Ca₂MgOsO₆ and Sr₂MgOsO₆ with a disorder model.

Atom	Wyckoff Positions	Occupancy	<i>x</i>	<i>y</i>	<i>z</i>	<i>B</i> (Å ²)
Ca ₂ MgOsO ₆ , Space group <i>P2₁/n</i> (No. 14), $a = 5.40958(10)$ Å, $b = 5.54031(10)$ Å, $c = 7.69909(14)$ Å, $\beta = 90.0474(19)$ °, $Z = 2$, and $V = 230.7475(74)$ Å ³ . Reliable factors: $R_{\text{wp}} = 11.012\%$, and $R_{\text{p}} = 5.909\%$.						
Ca	4 <i>e</i>	1	0.9678 (1)	0.0473(9)	0.2817(7)	1.0(fixed)
Os1/Mg1	2 <i>c</i>	0.5/ 0.5	0.5	0	0.5	0.5(fixed)
Mg2/Os2	2 <i>d</i>	0.5/ 0.5	0.5	0	0	0.5(fixed)
O1	4 <i>e</i>	1	0.0992(22)	0.4894(47)	0.2688(30)	1.0(fixed)
O2	4 <i>e</i>	1	0.7984(73)	0.2250(71)	0.0484(47)	1.0(fixed)
O3	4 <i>e</i>	1	0.1770(62)	0.2149(60)	0.9550(50)	1.0(fixed)
Sr ₂ MgOsO ₆ , Space group <i>I4/m</i> (No. 87), $a = 5.56065(4)$ Å, $c = 7.92136(7)$ Å, $Z = 2$, and $V = 244.9352(36)$ Å ³ . Reliable factors: $R_{\text{wp}} = 5.985\%$, and $R_{\text{p}} = 2.692\%$.						
Sr	4 <i>d</i>	1	0.5	0	0.25	0.5(fixed)
Os1/Mg1	2 <i>a</i>	0.5/ 0.5	0	0	0	0.5(fixed)
Mg2/Os2	2 <i>b</i>	0.5/ 0.5	0	0	0.5	0.5(fixed)
O1	8 <i>h</i>	1	0.1688(21)	0.2690(24)	0	1.0(fixed)
O2	4 <i>e</i>	1	0	0	0.2976(19)	1.0(fixed)

Pertinent bond lengths (*l*) of Ca₂MgOsO₆ and Sr₂MgOsO₆ were presented in **Table 4.4**; the average Mg–O distances were 2.07(3) Å and 2.05(3) Å for Ca₂MgOsO₆ and Sr₂MgOsO₆, respectively. The averages were comparable to those of A₂MgReO₆ (2.08 Å, 2.00 Å, and 2.06 Å for A = Ba, Sr, and Ca, respectively) [26], confirming that Mg was certainly divalent. Indeed, the bond-valence sums (BVSs) of Mg in Ca₂MgOsO₆ and Sr₂MgOsO₆ were 2.15 and 2.29, respectively [27], which were in reasonable agreement with the divalency of Mg. The divalent state was the most stable of the valence states observed for Mg in solid-state materials [28]. The Ca and Sr atoms were

also evaluated to be divalent by BVS calculations (see **Table 4.4**). Therefore, Os was reasonably assumed to be hexavalent, to satisfy the total charge valence of each compound. This assumption was effective when the compound was oxygen-stoichiometric and the Os–O bonds were fully ionic. To avoid the risk of exposure to the highly toxic OsO₄, we did not conduct a thermogravimetric analysis of the compounds for the measurement of oxygen stoichiometry.

Table 4.4 Selected bond lengths (*l*) and bond valence sums (BVSs)^a for Ca₂MgOsO₆ and Sr₂MgOsO₆.

Bond	<i>l</i> (Å)	
	Ca ₂ MgOsO ₆	Sr ₂ MgOsO ₆
Mg–O1	2.043(4) ×2	2.069(8) ×4
Mg–O2	2.068(5) ×2	2.011(6) ×2
Mg–O3	2.110(5) ×2	
BVS(Mg)	2.15	2.29
Ca(Sr)–O1	2.354(5), 2.449(6), 3.112(5), 3.200(6)	2.685(5) ×4 2.903(6) ×4
Ca(Sr)–O2	2.332(6), 2.618(6), 2.664(6), 3.425(6)	2.781(1) ×4
Ca(Sr)–O3	2.479(6), 2.604(7), 2.658(7), 3.296(6)	
BVS(Ca/Sr)	2.03	2.01
Os–O1	1.922(4) ×2	1.875(8) ×4
Os–O2	1.926(4) ×2	1.949(6) ×2
Os–O3	1.845(5) ×2	
BVS(Os)	6.49	6.45

Note. ^a BVS = $\sum_{i=1}^N v_i$, $v_i = \exp[(R_0 - d_i)/B]$, *N* is the coordination number, *B* = 0.37, $R_0(\text{Mg}^{2+}) = 1.693$, $R_0(\text{Ca}^{2+}) = 1.967$, $R_0(\text{Sr}^{2+}) = 2.118$, and $R_0(\text{Os}^{6+}) = 1.925$ [29].

The average Os–O bond lengths in Ca₂MgOsO₆ and Sr₂MgOsO₆ were the same (1.90(4) Å), which was comparable to the Os⁶⁺–O bond lengths in Sr₂NiOsO₆ (1.91 Å) and Ca₂NiOsO₆ (1.92 Å) [30]. The BVS of Os was, however, slightly overestimated: it was 6.49 and 6.45 for the Ca and Sr compounds, respectively. For comparison, the BVS of Os in Na₂Os⁶⁺O₄ was mentioned to be 6.07, with an average Os–O bond length of 1.94 Å [29]. This overestimation was possibly due to overbonding, which suggested that the Os–O bond was not fully ionic. Additionally, there was a difference between the

OsO₆ octahedra of Ca₂MgOsO₆ and Sr₂MgOsO₆, which was caused by crystallization of these materials in different space groups; the Ca compound had three different Os–O bonds in the octahedra whereas the Sr compound had two different Os–O bonds. Although, the average Os–O bond lengths were the same, the slight distortion of the octahedra might potentially alter the crystal field or the electronic ground state.

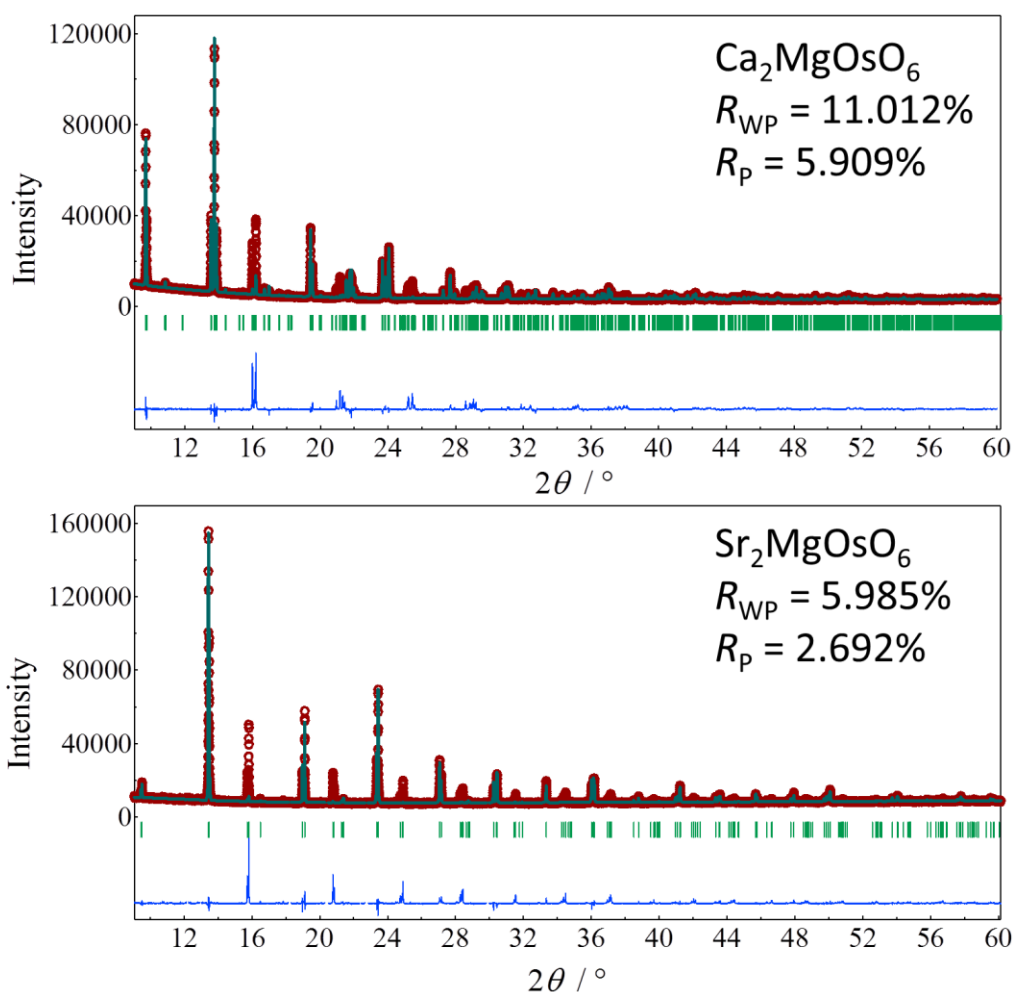


Figure 4.4 Rietveld analyses of the SXRD patterns for Ca₂MgOsO₆ and Sr₂MgOsO₆ with a disorder model.

In Ca₂MgOsO₆, the inter-octahedral Mg–O–Os angles were 151.6(2)°, 152.3(2)°, and 156.4(3)°. These angles were much different from that for a linear arrangement (180°), indicating that the octahedral connections were buckled to some extent in any direction. However, the inter-octahedral Mg–O–Os angles in Sr₂MgOsO₆ were 180° along the *c* axis and 171.0(4)° in the *ab* plane, as depicted in **Fig. 4.3(b)**. The degree of

buckling of the octahedral connections appeared to be drastically reduced by the substitution of Sr for Ca. The reduced degree of buckling might be related to the change in symmetry from monoclinic ($P2_1/n$ for Ca) to tetragonal ($I4/m$ for Sr). Note that the Glazer's notations were $a^-a^-c^+$ and $a^0a^0c^-$ for $\text{Ca}_2\text{MgOsO}_6$ and $\text{Sr}_2\text{MgOsO}_6$, respectively, where the superscripts indicated that the neighboring layers of octahedral showed no tilt (0°), rotate in the same direction (+), or rotate in opposite (-) directions [31].

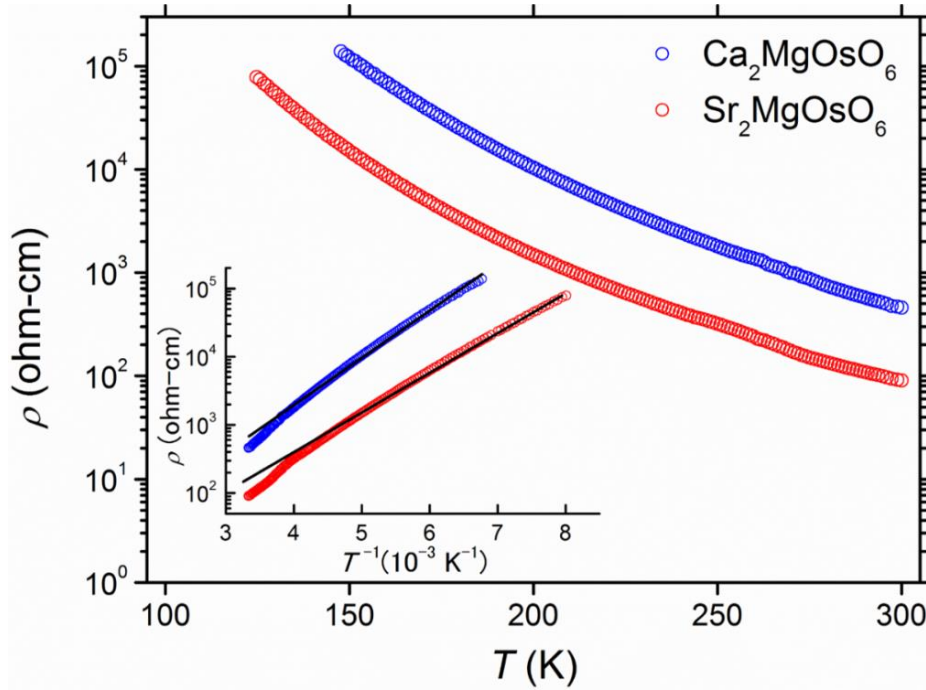


Figure 4.5 Temperature dependences of ρ of polycrystalline $\text{Ca}_2\text{MgOsO}_6$ and $\text{Sr}_2\text{MgOsO}_6$. The inset showed the Arrhenius plot of the data and the best-fit lines.

4.4 Electrical properties

The temperature dependences of ρ of the polycrystalline $\text{Ca}_2\text{MgOsO}_6$ and $\text{Sr}_2\text{MgOsO}_6$ clearly indicated semiconductor-like behaviors, as depicted in **Fig. 4.5**. The ρ values at room temperature were $\sim 90 \Omega\cdot\text{cm}$ and $\sim 450 \Omega\cdot\text{cm}$ for $\text{Ca}_2\text{MgOsO}_6$ and $\text{Sr}_2\text{MgOsO}_6$, respectively; these were more than three orders of magnitude greater than the expected value for a conducting polycrystalline oxide. In addition, ρ continuously increased upon cooling and exceeds the instrumental limit at temperatures of 120-150 K. The inset in **Fig. 4.5** exhibited the data in alternative plot, showing the roughly linear dependence. Fitting the Arrhenius equation to the plot (see the solid lines in the inset of

Fig. 4.5) yielded activation energies of 0.29(1) eV for $\text{Ca}_2\text{MgOsO}_6$ and 0.24(1) eV for $\text{Sr}_2\text{MgOsO}_6$, which were much smaller than those of related oxides $\text{Ca}_2\text{FeOsO}_6$ (~1.2 eV) [32] and $\text{Ba}_2\text{CuOsO}_6$ (~0.81 eV) [33]. A small amount of KCl residue in the samples might have an impact on the transport measurements to some extent; however, the insulating behavior was essential because of the absence of an electronic contribution to the low-temperature C_p , as shown later.

4.5 Magnetic properties

4.5.1 Susceptibility

The temperature dependence of χ of polycrystalline $\text{Ca}_2\text{MgOsO}_6$ and $\text{Sr}_2\text{MgOsO}_6$ was also measured (**Fig. 4.6(a)**). In the case of $\text{Ca}_2\text{MgOsO}_6$, χ monotonically increases upon cooling, without any anomaly, except for a cusp at 19 K. Below the cusp temperature, a thermal hysteresis develops on cooling, as could be seen by the difference between the ZFC and FC curves, suggesting the establishment of a magnetic-glass state or an antiferromagnetically ordered state. Because C_p measurements (shown later) did not reveal any transition entropy (ΔS) in the vicinity near 19 K, a long-range antiferromagnetic ordering was unlikely to be responsible for the observed cusp for $\text{Ca}_2\text{MgOsO}_6$.

In contrast, the temperature dependence of χ for $\text{Sr}_2\text{MgOsO}_6$ showed a solid transition at a temperature of ~110 K in both the ZFC and FC curves (inset of **Fig. 4.6(a)**), suggesting the establishment of a long-range antiferromagnetic ordering. Indeed, the C_p vs. T curve showed a broad peak near 110 K (shown later), supporting the antiferromagnetic ordering. To further characterize the magnetic nature of the compounds, the Curie–Weiss law was applied to the high-temperature part of the χ^{-1} vs. T plot of the FC curves, as shown in **Fig. 4.6(b)**. The temperature range used for the analysis was 200–385 K for $\text{Ca}_2\text{MgOsO}_6$ and 140–385 K for $\text{Sr}_2\text{MgOsO}_6$.

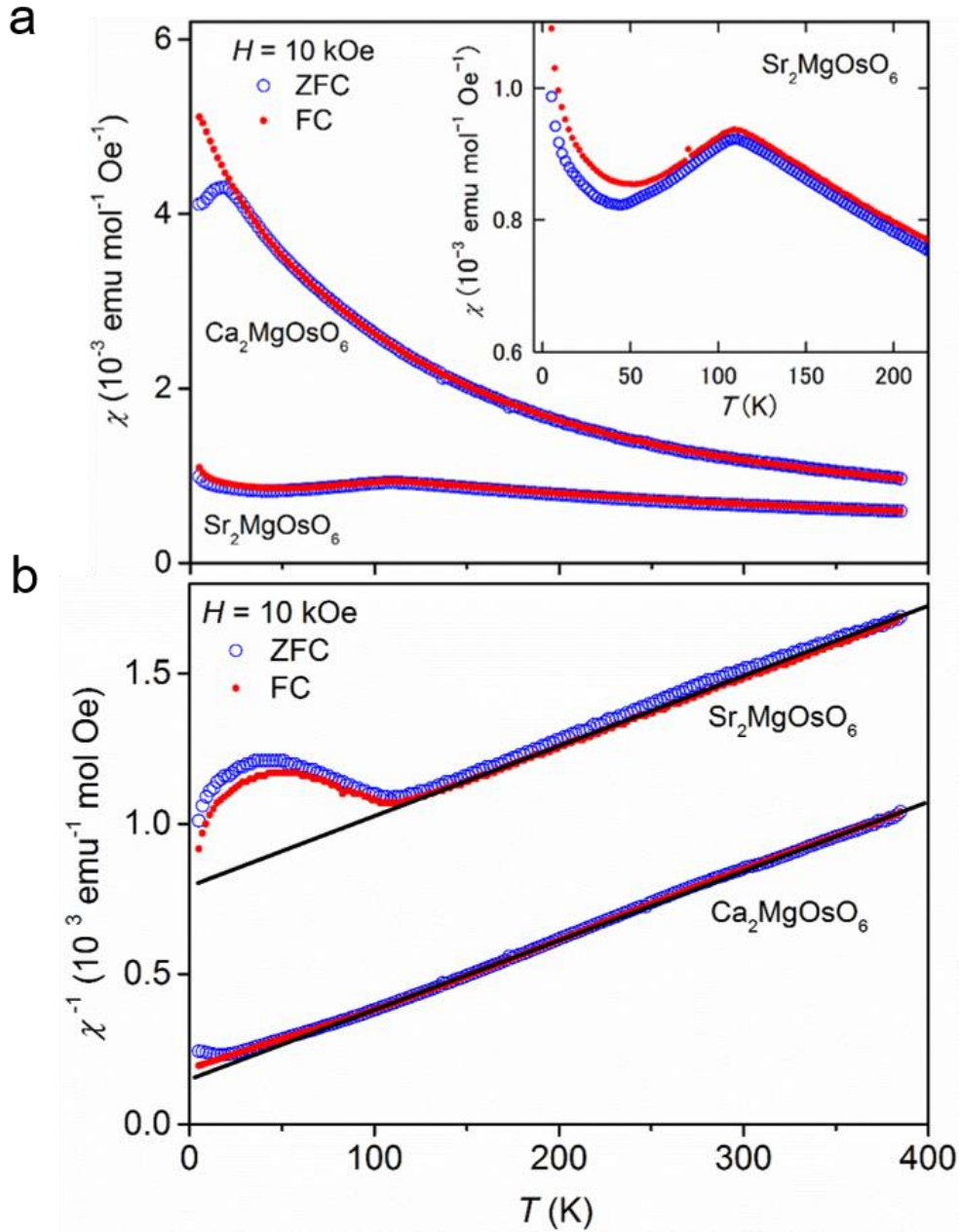


Figure 4.6 (a) Temperature dependence of χ of polycrystalline $\text{Ca}_2\text{MgOsO}_6$ and $\text{Sr}_2\text{MgOsO}_6$ measured in a magnetic field of 10 kOe. Solid and open symbols denote FC and ZFC processes, respectively. The inset showed an enlarged view of the plots for $\text{Sr}_2\text{MgOsO}_6$. (b) Reciprocal χ vs. temperature for the compounds, and fit lines of the Curie–Weiss law (solid lines).

By the linear least-squares fitting of the Curie–Weiss law to the data, using the expression $\chi(T) = N_A \mu_{\text{eff}}^2 / [3k_B(T - \Theta_W)]$ (where N_A was the Avogadro constant, k_B was the Boltzmann constant, Θ_W was the Weiss temperature, and μ_{eff} was the effective Bohr magneton), μ_{eff} and Θ_W were estimated to be $1.874(4) \mu_B$ and $-71.5(7) \text{ K}$, respectively,

for $\text{Ca}_2\text{MgOsO}_6$, and $1.867(4) \mu_{\text{B}}$ and $-347.3(5) \text{ K}$, respectively, for $\text{Sr}_2\text{MgOsO}_6$. Although both μ_{eff} values were comparable to those of the isoelectronic $\text{Ca}_3\text{Os}^{6+}\text{O}_6$ ($1.99 \mu_{\text{B}}$) and $\text{Ba}_2\text{CaOs}^{6+}\text{O}_6$ ($1.61 \mu_{\text{B}}$) [5], [34], they were much lower than the spin-only moment for Os^{6+} ($2.83 \mu_{\text{B}}$). This underestimation has been argued to be caused by the spin-orbit coupling (SOC) [34], [35].

Upon the substitution of Sr for Ca, the change in μ_{eff} was trivial, but Θ_{W} was remarkably enhanced by almost fivefold. Because Θ_{W} remained negative, antiferromagnetic correlations were predominant for both compounds. The enhancement of Θ_{W} therefore suggested that the antiferromagnetic correlation of $\text{Sr}_2\text{MgOsO}_6$ was much greater than that of $\text{Ca}_2\text{MgOsO}_6$; alternatively, the ferromagnetic correlation would be less dominant upon the Sr substitution. If the latter case was true, the low magnitude of Θ_{W} would result from a balance of the ferromagnetic and antiferromagnetic correlations.

4.5.2 Isothermal magnetization

The isothermal magnetization for both compounds was measured at 5 K, as shown in **Fig. 4.7**. A rather linear behavior without notable hysteresis was observed for $\text{Sr}_2\text{MgOsO}_6$, while a broad hysteresis and enhanced magnetization (more than three times larger than that for $\text{Sr}_2\text{MgOsO}_6$) were observed for $\text{Ca}_2\text{MgOsO}_6$. The observed behaviors were in accordance with the antiferromagnetic ordering and possible magnetic freezing for $\text{Sr}_2\text{MgOsO}_6$ and $\text{Ca}_2\text{MgOsO}_6$, respectively. Because there was no indication of magnetic saturation, the ferromagnetic correlation likely competed with the antiferromagnetic correlation in $\text{Ca}_2\text{MgOsO}_6$. The hysteresis loop for $\text{Ca}_2\text{MgOsO}_6$ was not perfectly symmetric (see the slight offset along the vertical axis), probably because the magnetic-field range was insufficient to cover the full hysteresis loop.

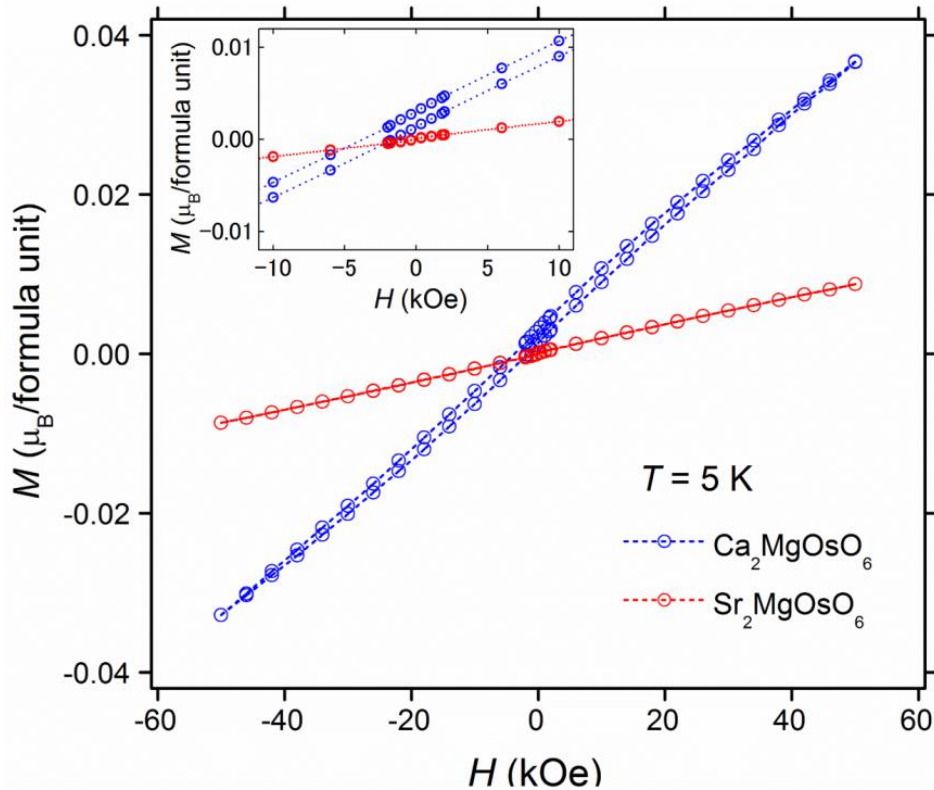


Figure 4.7 Isothermal magnetizations of the polycrystalline $\text{Ca}_2\text{MgOsO}_6$ and $\text{Sr}_2\text{MgOsO}_6$ at 5 K. The inset showed the zoomed-in details between -10 kOe to 10 kOe.

4.6 Heat capacity

The C_p of $\text{Ca}_2\text{MgOsO}_6$ and $\text{Sr}_2\text{MgOsO}_6$ were measured between 2 K and 300 K. Near the antiferromagnetic-transition temperature of ~ 110 K, a magnetic field of 70 kOe was applied; the data are plotted in **Figs. 4.8(a)** and **(b)**. In the measurements, there was no trace of a magnetic transition for $\text{Ca}_2\text{MgOsO}_6$, and only a monotonic decrease upon cooling to the low-temperature limit was observed. In contrast, a peak-like anomaly was detected near ~ 110 K for $\text{Sr}_2\text{MgOsO}_6$, as was expected for an antiferromagnetic transition. A magnetic field of 70 kOe was applied to $\text{Sr}_2\text{MgOsO}_6$, but it had little impact on the peak-like anomaly, possibly because it was too weak to alter the magnetic transition.

ΔS over the peak-like anomaly was roughly estimated by subtracting the phonon contributions (C_{fit}) from the total C_p (see the dotted curve in **Fig. 4.8(b)**, as discussed later). The integration of $(C_p - C_{\text{fit}})/T$ was approximately $0.41 R$, where R was the

universal gas constant. Therefore, ΔS corresponded to 37% of the spin-only magnetic entropy of $R \ln(3)$ for Os^{6+} (t_{2g}^2). The underestimation was possibly because the SOC of Os^{6+} had a substantial impact on the magnetism, being connected to the smaller μ_{eff} in the χ - T measurement. In addition, the development of short-range magnetic ordering above the transition temperature must also be considered for further quantitative analysis.

A quantitative analysis of the C_p vs. T curve was conducted by applying the Debye model; however, it fit poorly to the data as indicated in the plot. We attempted to improve the quality of the fit by linearly adding the Einstein term to the Debye term, as follows:

$$C_{\text{fit}}(T) = n_{\text{D}} \times 9N_{\text{A}}k_{\text{B}} \left(\frac{T}{T_{\text{D}}} \right)^3 \int_0^{T_{\text{D}}/T} \frac{x^4 e^x}{(e^x - 1)^2} dx + n_{\text{E}} \times 3N_{\text{A}}k_{\text{B}} \left(\frac{T_{\text{E}}}{T} \right)^2 \frac{e^{T_{\text{E}}/T}}{(e^{T_{\text{E}}/T} - 1)^2},$$

where N_{A} was Avogadro's constant, and T_{D} and T_{E} were the Debye and Einstein temperatures, respectively. The scale factors, n_{D} and n_{E} , corresponded to the number of vibrational modes per formula unit in the Debye and Einstein terms, respectively. The overall quality of the fit was eventually improved, as indicated in the plot. The fitting procedure yielded the following results: $T_{\text{D}} = 659(5)$ K, $T_{\text{E}} = 167(3)$ K, $n_{\text{D}} = 7.00(4)$, and $n_{\text{E}} = 1.61(5)$ for $\text{Ca}_2\text{MgOsO}_6$; and $T_{\text{D}} = 785(22)$ K, $T_{\text{E}} = 166(4)$ K, $n_{\text{D}} = 6.60(10)$, and $n_{\text{E}} = 3.52(15)$ for $\text{Sr}_2\text{MgOsO}_6$. Although the Einstein term has been discussed to correspond to a local phonon mode such as “rattling” in clathrate [36] and beta-pyrochlore oxide [37], the C_p/T^3 vs. T plots (not shown) indicated no obvious anomalous local phonon contribution even at temperatures below 20 K. The phonon-mode distributions for both compounds needed to be clarified to reveal the complex nature of the lattices.

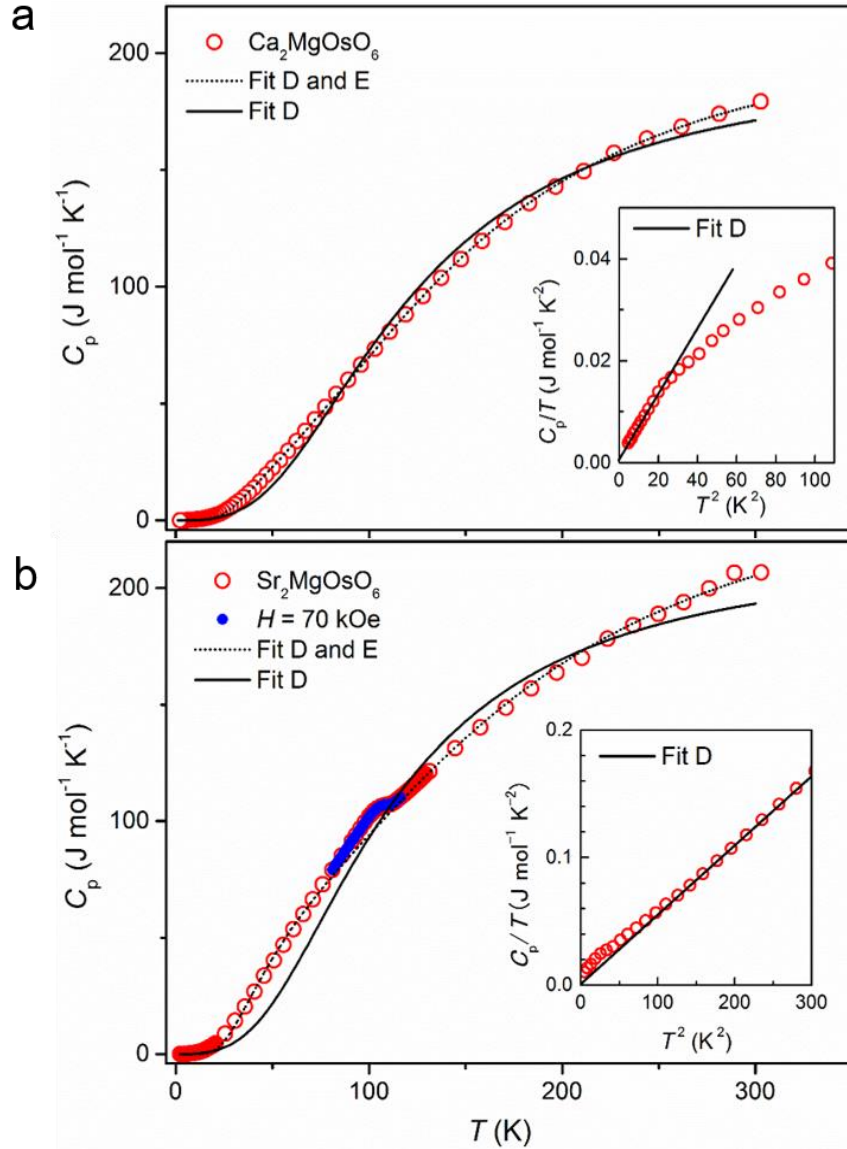


Figure 4.8 Temperature dependence of C_p of (a) $\text{Ca}_2\text{MgOsO}_6$ and (b) $\text{Sr}_2\text{MgOsO}_6$. The solid and dotted curves represent the fits of models to the data. Small solid circles represent the data measured in a magnetic field of 70 kOe. The insets show linear fits to the low-temperature part of the C_p/T vs. T^2 plots. The labels D and E indicate the Debye and Einstein models, respectively.

We analyzed the low-temperature part ($\ll T_D$) of C_p by applying the approximated Debye model $C_p \approx \gamma T + \beta T^3$, where γ was the electronic specific heat coefficient and β was a constant related to the Debye temperature T_D ($\sim \beta^{-1/3}$). When the approximation was accurate, the C_p/T vs T^2 plot must show a linear trend. Clear linearity was confirmed for the plot for $\text{Ca}_2\text{MgOsO}_6$; a fit of the model yielded γ and β values of $0.93(6) \text{ mJ mol}^{-1} \text{K}^{-2}$ and $6.44(5) \times 10^{-4} \text{ J mol}^{-1} \text{K}^{-4}$, respectively (see the inset of **Fig.**

4.8(a)). From the β value, T_D was calculated to be 311(1) K. The low-temperature C_p for $\text{Sr}_2\text{MgOsO}_6$ was analyzed in the same manner (see the inset of **Fig. 4.8(b)**), affording γ and β values of 0.1(5) $\text{mJ mol}^{-1} \text{K}^{-2}$ and $5.50(2) \times 10^{-4} \text{J mol}^{-1} \text{K}^{-4}$, respectively. T_D was calculated to be 328(5) K. Although the analysis seemed to be influenced to some extent by a possible magnetic contribution, the estimated γ for both compounds was fairly close to zero, suggesting a band-gap opening in the electronic state.

4.7 Discussions

In Table 4.1, the three largest absolute values of $\theta_W/T_{N,f}$ (> 16) were observed only for the lattice of cubic symmetry ($Fm-3m$), suggesting that an impact of geometrical frustration on the magnetic properties was significant in the cubic lattice than the tetragonal ($I4/m$) and monoclinic ($P2_1/n$) lattices. Consequences of geometrical frustration seemed to be insignificant in both tetragonal and monoclinic lattices. However, the tetragonal-phase $\text{Sr}_2\text{MgOsO}_6$ ($I4/m$) showed a long-range antiferromagnetic transition at ~ 110 K, whereas the monoclinic-phase $\text{Ca}_2\text{MgOsO}_6$ ($P2_1/n$) did not show any comparable magnetic ordering above 2 K (except for a magnetic cusp at 19 K). The remarkable change in magnetic properties was probably related more closely to the degree of local lattice distortion than to the degree of geometrical frustration.

The substitution of Sr for Ca seemed to improve the lattice environment toward stabilizing a long-range magnetic ordering. The average Os–O–Mg angle changed from 153.4° (Ca) to 175.5° (Sr), whereas the octahedra Os^{6+}O_6 were rather solid (the difference between the shortest and longest Os–O bond length were 4.4% for Ca and 4.0% for Sr). The degree of buckling of the octahedral connections might have a substantial impact on the changes in the magnetic states. This probably occurred via the enhancement of the extended superexchange interactions mediated by linkages such as $-\text{Os}(d^2)-\text{O}-\text{O}-\text{Os}(d^2)-$ and $-\text{Os}(d^2)-\text{O}-\text{Mg}(d^0)-\text{O}-\text{Os}(d^2)-$ [38], [39]. In order to clarify the local magnetic picture, the bond-angle dependence of the character and magnitude

of the enhanced superexchange interactions regarding the d^2 element require further investigations. Perhaps, if a buckling-free Os^{6+} sublattice-containing double perovskite was stabilized, it might show a transition temperature well above 110 K. Otherwise, the magnetic frustration might be enhanced by increasing the lattice symmetry, hence, the transition temperature might decrease to well below 110 K, as argued for $(\text{La},\text{A})\text{CoNbO}_6$ ($A = \text{Ca}, \text{Sr}, \text{Ba}$) [40]. These possibilities were left to future work.

4.8 Theoretical calculation

To shed more light on the electronic and magnetic states of $\text{Ca}_2\text{MgOsO}_6$ and $\text{Sr}_2\text{MgOsO}_6$, the spin-resolved total and partial electronic densities of states (DOSs) were calculated by a first-principles method. The total DOS structures, drawn in Figures **Figs. 4.9(a)** and **(b)**, indicated the insulating characters of the studied materials. In $\text{Ca}_2\text{MgOsO}_6$ and $\text{Sr}_2\text{MgOsO}_6$, each Os^{6+} ion was coordinated by six oxygens and thus had the $5d^2$ configuration, which provided charges as well as spins. The partial DOS structure (**Figs. 4.10(a)** and **(b)**) indicated that the Os-5d state was partially occupied in both the spin-up and spin-down channels. The valence and conduction bands of both $\text{Ca}_2\text{MgOsO}_6$ and $\text{Sr}_2\text{MgOsO}_6$ were found close to the Fermi level (E_F). Additionally, the O-2p state hybridized significantly with the Os-5d state, especially near E_F , while both the states remained almost independent below -1.5 eV. The band dispersion was shown in **Figs. 4.11(a)** and **(b)**. Both for the spin-up and spin-down channels, two occupied bands out of the six Os-5d- t_{2g} bands lied in the topmost valence region immediately below E_F , while the remaining four un-occupied bands lied in the conduction region, forming a gap between the valence and the conduction region. Thus, $\text{Ca}_2\text{MgOsO}_6$ and $\text{Sr}_2\text{MgOsO}_6$ were found to have indirect band gaps of 0.25 eV and 0.15 eV, respectively, formed by Os-5d states. This observation seemed to approximate the experimental determination of 0.29(1) eV and 0.24(1) eV for $\text{Ca}_2\text{MgOsO}_6$ and $\text{Sr}_2\text{MgOsO}_6$, respectively, although contributions from grain boundaries and any resistive impurities such as KCl remain undetermined.

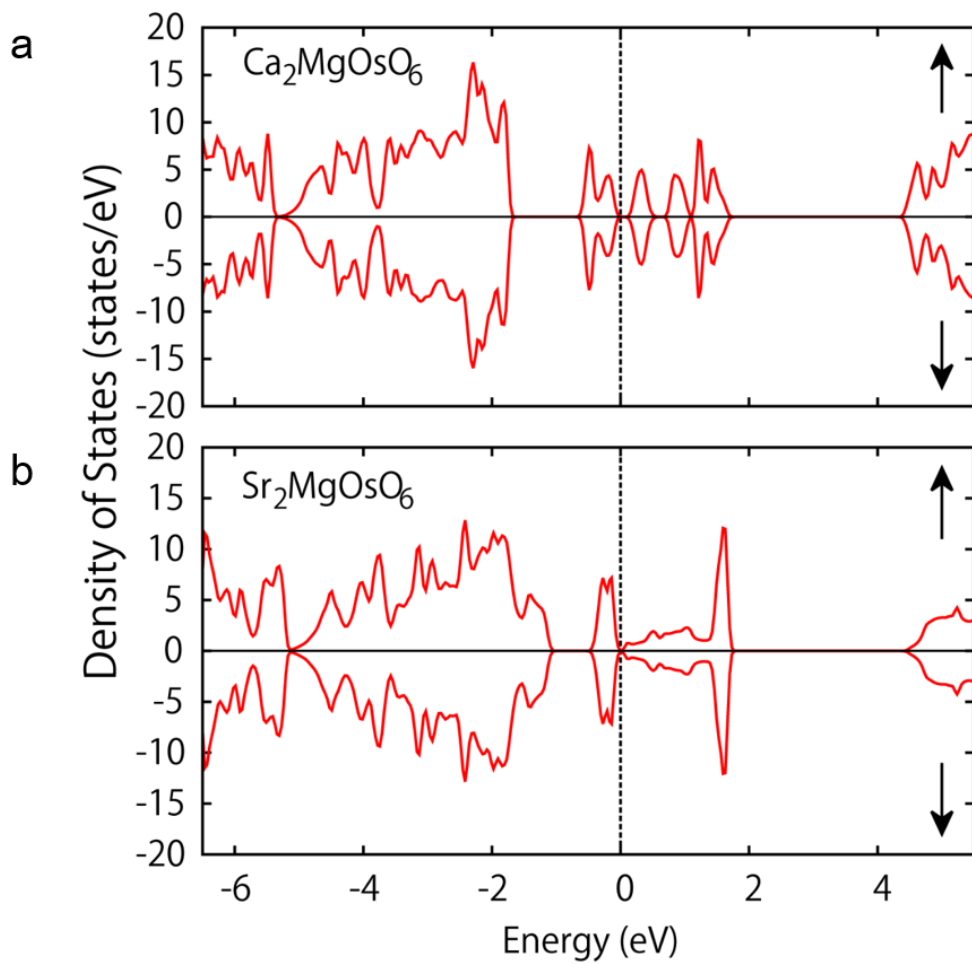


Figure 4.9 Total DOS obtained by the GGA+ U scheme for spin-up (\uparrow) and spin-down (\downarrow) channels of (a) $\text{Ca}_2\text{MgOsO}_6$ and (b) $\text{Sr}_2\text{MgOsO}_6$. The vertical dotted lines indicated E_F (set at zero).

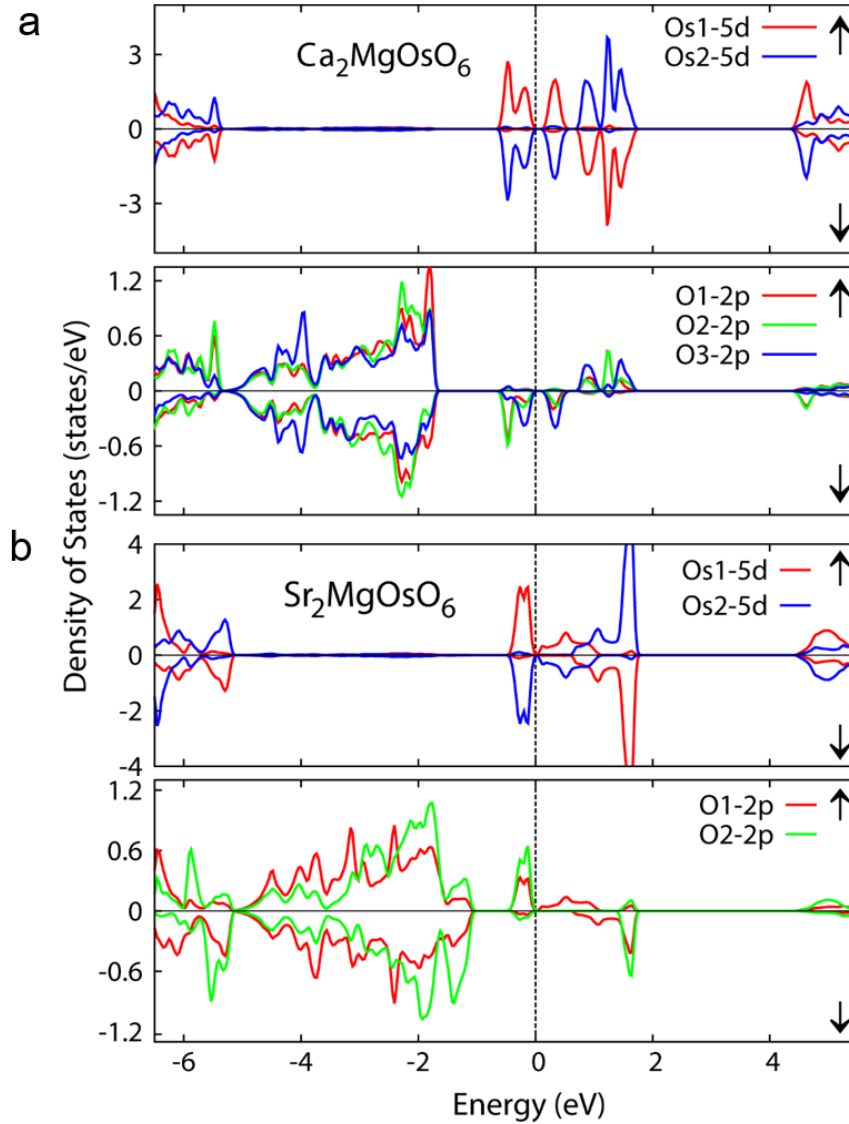


Figure 4.10 Partial DOS for Os-5d and O-2p states obtained by the GGA+ U scheme for spin-up (\uparrow) and spin-down (\downarrow) channels of (a) $\text{Ca}_2\text{MgOsO}_6$ and (b) $\text{Sr}_2\text{MgOsO}_6$. The vertical dotted lines indicated E_F (set at zero).

It was noted that the band gap opens only when U value is 1.8 eV or larger for $\text{Ca}_2\text{MgOsO}_6$ and 3.0 eV or larger for $\text{Sr}_2\text{MgOsO}_6$. $\text{Ca}_2\text{MgOsO}_6$ crystallized in a monoclinic structure with substantial buckling of the octahedral network, whereas $\text{Sr}_2\text{MgOsO}_6$ crystallized in a tetragonal structure with a small degree of buckling. The local lattice distortion might play an additional role in opening the gap, such that it required a lower U for $\text{Ca}_2\text{MgOsO}_6$ than for $\text{Sr}_2\text{MgOsO}_6$. Either way, U seemed to be comparable to the reported values for 5d oxides ($\sim 1\text{-}3$ eV). The magnitude of U suggested that the Mott mechanism possibly accounts for the gap opening for both

$\text{Ca}_2\text{MgOsO}_6$ and $\text{Sr}_2\text{MgOsO}_6$. At present, we focused on calculations within the GGA+ U scheme (SOC was not included), where the gap was predicted to open under the influence of strong correlations and the lattice distortion.

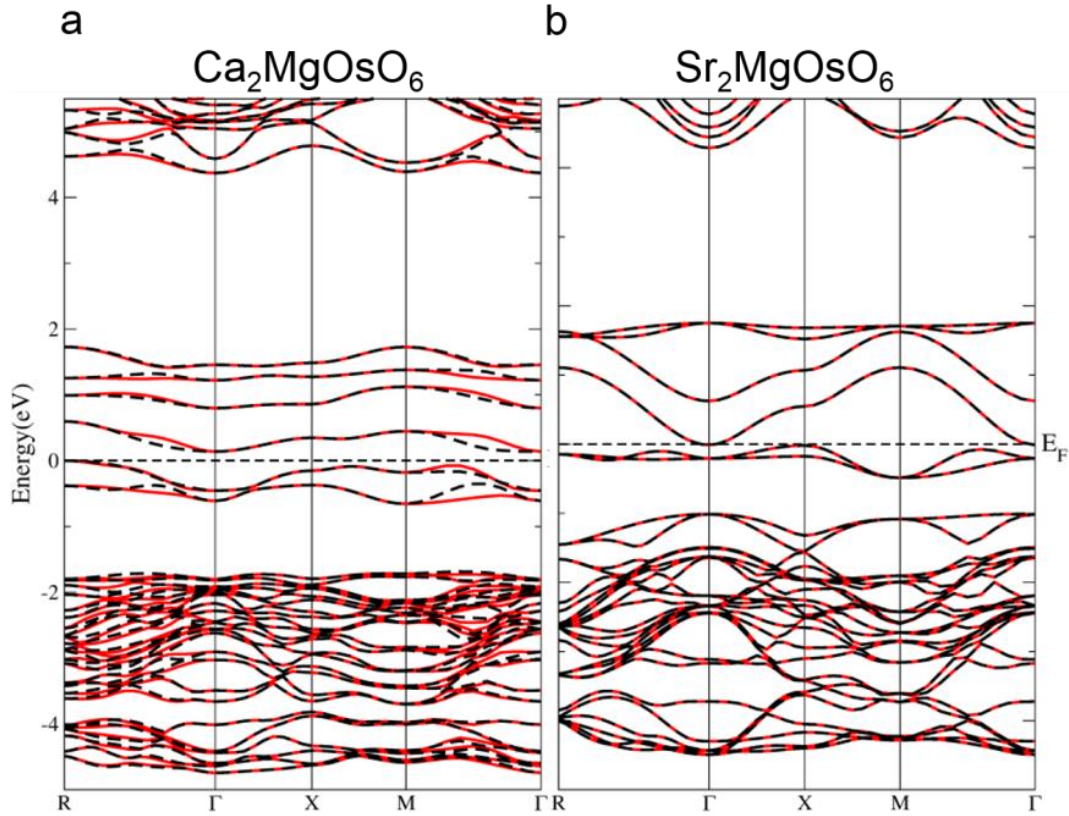


Figure 4.11 Band dispersion in a GGA+ U scheme for the spin-up (red) and spin-down (black) channels of (a) $\text{Ca}_2\text{MgOsO}_6$ and (b) $\text{Sr}_2\text{MgOsO}_6$.

We investigated the magnetic nature of $\text{Sr}_2\text{MgOsO}_6$ by first-principles density functional calculations based on an antiferromagnetic ground state. In the calculations, each Os atom was suggested to couple magnetically with neighboring Os atoms in the double-perovskite structure. Although each Os atom formally carried a magnetic moment of $2 \mu_B$ (a spin-only view), the first-principles results indicated that the moment was $\sim 1.1 \mu_B$ per Os. The difference was accounted for by the partial transfer of moment (approximately $0.3 \mu_B$) to three inequivalent oxygens via charge transfer between the Os and O atoms. The magnetic nature needed further experimental investigations such as neutron scattering to establish a solid picture of the magnetism of both compounds.

4. 9 Conclusion

$\text{Sr}_2\text{MgOsO}_6$ showed a long-range antiferromagnetic transition at ~ 110 K; by contrast, the isoelectronic $\text{Ca}_2\text{MgOsO}_6$ did not show any comparable magnetic ordering above 2 K, except for a magnetic cusp at 19 K. The remarkable change in magnetic properties was likely owing to local lattice distortion rather than to the impact of geometrical frustration. Additional theoretical studies were needed for revealing the origin of certain magnetic-state changes.

Based on the first-principles density functional approach, the double-perovskite oxides $\text{Ca}_2\text{MgOsO}_6$ and $\text{Sr}_2\text{MgOsO}_6$ were likely to be antiferromagnetic Mott insulators, wherein the electronic correlations ($U \sim 1.8\text{-}3.0$ eV) as well as the crystal field had major impacts on opening the gap. The indirect band gaps were predicted to be 0.25 eV and 0.15 eV for $\text{Ca}_2\text{MgOsO}_6$ and $\text{Sr}_2\text{MgOsO}_6$, respectively, approximating the experimental estimation. Without U , a charge gap never opened at E_F .

Recent studies on $5d$ oxides, such as Sr_2IrO_4 [41]–[43] and Na_2IrO_3 [44], [45], suggested the formation of a spin-orbit interaction-assisted Mott-insulating state; research on new materials focusing on the singular Mott state was in progress. However, it turned out that in a regular $5d$ perovskite oxide, the metallic state was more robust than the insulating state, largely because of the spatially extended nature of the $5d$ orbitals, as suggested for materials such as NaWO_3 [46], SrIrO_3 [47], and SrOsO_3 [48]. Therefore, $5d$ layered oxides should be targeted for the exploration of additional singular Mott-insulating states because, in general, the reduced lattice dimensions were expected to help in narrowing the $5d$ band, which assisted in opening a charge gap. The present results suggested that a double-perovskite oxide containing a single magnetic sublattice could also be helpful for exploring singular Mott states. Thus, the present compounds offered a valuable opportunity for investigating the basis of $5d$ electrons, not only toward the possible practical application of double-perovskite oxides in multifunctional devices, but also toward the synthesis of new singular Mott-insulating compounds.

References in chapter 4

- [1] E. Y. Tsymbal, E. R. A. Dagotto, C.-B. Eom, and R. Ramesh, Eds., *Multifunctional Oxide Heterostructures*. Oxford University Press, 2012.
- [2] K.-I. Kobayashi, T. Kimura, H. Sawada, K. Terakura, and Y. Tokura, “Room-temperature magnetoresistance in an oxide material with an ordered double-perovskite structure,” *Nature*, vol. 395, no. 6703, pp. 677–680, Oct. 1998.
- [3] Y. Krockenberger, K. Mogare, M. Reehuis, M. Tovar, M. Jansen, G. Vaitheeswaran, V. Kanchana, F. Bultmark, A. Delin, F. Wilhelm, A. Rogalev, A. Winkler, and L. Alff, “ $\text{Sr}_2\text{CrOsO}_6$: End point of a spin-polarized metal-insulator transition by $5d$ band filling,” *Phys. Rev. B*, vol. 75, no. 2, p. 020404, Jan. 2007.
- [4] A. K. Paul, M. Reehuis, V. Ksenofontov, B. Yan, A. Hoser, D. M. Többens, P. M. Abdala, P. Adler, M. Jansen, and C. Felser, “Lattice Instability and Competing Spin Structures in the Double Perovskite Insulator $\text{Sr}_2\text{FeOsO}_6$,” *Phys. Rev. Lett.*, vol. 111, no. 16, p. 167205, Oct. 2013.
- [5] H. L. Feng, Y. Shi, Y. Guo, J. Li, A. Sato, Y. Sun, X. Wang, S. Yu, C. I. Sathish, and K. Yamaura, “High-pressure crystal growth and electromagnetic properties of $5d$ double-perovskite Ca_3OsO_6 ,” *J. Solid State Chem.*, vol. 201, pp. 186–190, May 2013.
- [6] B. Yan, A. K. Paul, S. Kanungo, M. Reehuis, A. Hoser, D. M. Többens, W. Schnelle, R. C. Williams, T. Lancaster, F. Xiao, J. S. Mödler, S. J. Blundell, W. Hayes, C. Felser, and M. Jansen, “Lattice-Site-Specific Spin Dynamics in Double Perovskite $\text{Sr}_2\text{CoOsO}_6$,” *Phys. Rev. Lett.*, vol. 112, no. 14, p. 147202, Apr. 2014.
- [7] R. Morrow, R. Mishra, O. D. Restrepo, M. R. Ball, W. Windl, S. Wurmehl, U. Stockert, B. Büchner, and P. M. Woodward, “Independent Ordering of Two Interpenetrating Magnetic Sublattices in the Double Perovskite $\text{Sr}_2\text{CoOsO}_6$,” *J. Am. Chem. Soc.*, vol. 135, no. 50, pp. 18824–18830, Dec. 2013.
- [8] A. Kumar Paul, M. Reehuis, C. Felser, P. M. Abdala, and M. Jansen, “Synthesis, Crystal Structure, and Properties of the Ordered Double Perovskite $\text{Sr}_2\text{CoOsO}_6$,” *Z.*

- Für Anorg. Allg. Chem.*, vol. 639, no. 14, pp. 2421–2425, Nov. 2013.
- [9] C. R. Wiebe, J. E. Greedan, G. M. Luke, and J. S. Gardner, “Spin-glass behavior in the $S=1/2$ fcc ordered perovskite $\text{Sr}_2\text{CaReO}_6$,” *Phys. Rev. B*, vol. 65, no. 14, p. 144413, Mar. 2002.
- [10] C. R. Wiebe, J. E. Greedan, P. P. Kyriakou, G. M. Luke, J. S. Gardner, A. Fukaya, I. M. Gat-Malureanu, P. L. Russo, A. T. Savici, and Y. J. Uemura, “Frustration-driven spin freezing in the $S=12$ fcc perovskite $\text{Sr}_2\text{MgReO}_6$,” *Phys. Rev. B*, vol. 68, no. 13, p. 134410, Oct. 2003.
- [11] T. Aharen, J. E. Greedan, C. A. Bridges, A. A. Aczel, J. Rodriguez, G. MacDougall, G. M. Luke, V. K. Michaelis, S. Kroecker, C. R. Wiebe, H. Zhou, and L. M. D. Cranswick, “Structure and magnetic properties of the $S=1$ geometrically frustrated double perovskites $\text{La}_2\text{LiReO}_6$ and Ba_2YReO_6 ,” *Phys. Rev. B*, vol. 81, no. 6, p. 064436, Feb. 2010.
- [12] A. W. Sleight, J. Longo, and R. Ward, “Compounds of Osmium and Rhenium with the Ordered Perovskite Structure,” *Inorg. Chem.*, vol. 1, no. 2, pp. 245–250, May 1962.
- [13] N. Rammeh, K. G. Bramnik, H. Ehrenberg, B. Stahl, H. Fuess, and A. Cheikh-Rouhou, “Crystal structure and magnetic properties of Mo-substituted ‘ $\text{Ba}_2(\text{Fe,W})_2\text{O}_6$ ’ double-perovskites: a synchrotron diffraction, magnetization and Mössbauer study,” *J. Alloys Compd.*, vol. 363, no. 1–2, pp. 24–31, Jan. 2004.
- [14] Z. Fu and W. Li, “Phase transition, phase transition temperature and crystal structure of a new compound - Ca_2PdWO_6 ,” *Science in China*, vol. 39, no. 9, pp. 981–990, 1996.
- [15] E. Iturbe-Zabaló, J. M. Igartua, and M. Gateshki, “Symmetry-mode analysis of the phase transitions in SrLaZnRuO_6 and SrLaMgRuO_6 ordered double perovskites,” *J. Appl. Crystallogr.*, vol. 46, no. 4, pp. 1085–1093, Aug. 2013.
- [16] K. Yamaura, D. P. Young, and E. Takayama-Muromachi, “Ferromagnetic transition in the correlated $4d$ perovskites $\text{SrRu}_{1-x}\text{Rh}_x\text{O}_3$,” *Phys. Rev. B*, vol. 69, no. 2, p. 024410, Jan. 2004.

- [17] M. Tanaka, Y. Katsuya, and A. Yamamoto, "A new large radius imaging plate camera for high-resolution and high-throughput synchrotron x-ray powder diffraction by multiexposure method," *Rev. Sci. Instrum.*, vol. 79, no. 7, p. 075106, Jul. 2008.
- [18] M. Tanaka, Y. Katsuya, Y. Matsushita, and O. Sakata, "Development of a synchrotron powder diffractometer with a one-dimensional X-ray detector for analysis of advanced materials," *J. Ceram. Soc. Jpn.*, vol. 121, no. 1411, pp. 287–290, 2013.
- [19] K. Momma and F. Izumi, "VESTA : a three-dimensional visualization system for electronic and structural analysis," *J. Appl. Crystallogr.*, vol. 41, no. 3, pp. 653–658, Jun. 2008.
- [20] F. Izumi and K. Momma, "Three-Dimensional Visualization in Powder Diffraction," *Solid State Phenom.*, vol. 130, pp. 15–20, 2007.
- [21] Y. S. Touloukian and E. H. Buyco, "Thermophysical Properties of Matter - the TPRC Data Series. Volume 5. Specific Heat - Nonmetallic Solids," 1970.
- [22] P. K. . Blaha, G. K. . Madsen, D. Kvasnicka, and J. Luitz, *An Augmented Plane Wave + Local Orbitals Program for Calculating Crystal Properties*. Austria: Technische Universitat: Wien, 2001.
- [23] J. P. Perdew, K. Burke, and M. Ernzerhof, "Generalized Gradient Approximation Made Simple," *Phys. Rev. Lett.*, vol. 77, no. 18, pp. 3865–3868, Oct. 1996.
- [24] V. I. Anisimov, F. Aryasetiawan, and A. I. Lichtenstein, "First-principles calculations of the electronic structure and spectra of strongly correlated systems: the LDA+ U method," *J. Phys. Condens. Matter*, vol. 9, no. 4, p. 767, Jan. 1997.
- [25] M. T. Anderson, K. B. Greenwood, G. A. Taylor, and K. R. Poeppelmeier, "B-cation arrangements in double perovskites," *Prog. Solid State Chem.*, vol. 22, no. 3, pp. 197–233, 1993.
- [26] K. G. Bramnik, H. Ehrenberg, J. K. Dehn, and H. Fuess, "Preparation, crystal structure, and magnetic properties of double perovskites M_2MgReO_6 (M=Ca, Sr, Ba)," *Solid State Sci.*, vol. 5, no. 1, pp. 235–241, Jan. 2003.

- [27] I. D. Brown, “Recent Developments in the Methods and Applications of the Bond Valence Model,” *Chem. Rev.*, vol. 109, no. 12, pp. 6858–6919, Dec. 2009.
- [28] S. P. Green, C. Jones, and A. Stasch, “Stable Magnesium(I) Compounds with Mg-Mg Bonds,” *Science*, vol. 318, no. 5857, pp. 1754–1757, Dec. 2007.
- [29] Y. G. Shi, Y. F. Guo, S. Yu, M. Arai, A. A. Belik, A. Sato, K. Yamaura, E. Takayama-Muromachi, T. Varga, and J. F. Mitchell, “High-pressure crystal growth and magnetic and electrical properties of the quasi-one dimensional osmium oxide Na_2OsO_4 ,” *J. Solid State Chem.*, vol. 183, no. 2, pp. 402–407, Feb. 2010.
- [30] R. Macquart, S.-J. Kim, W. R. Gemmill, J. K. Stalick, Y. Lee, T. Vogt, and H.-C. zur Loye, “Synthesis, Structure, and Magnetic Properties of $\text{Sr}_2\text{NiOsO}_6$ and $\text{Ca}_2\text{NiOsO}_6$: Two New Osmium-Containing Double Perovskites,” *Inorg. Chem.*, vol. 44, no. 26, pp. 9676–9683, Dec. 2005.
- [31] A. M. Glazer, “The classification of tilted octahedra in perovskites,” *Acta Crystallogr. B*, vol. 28, no. 11, pp. 3384–3392, Nov. 1972.
- [32] H. L. Feng, M. Arai, Y. Matsushita, Y. Tsujimoto, Y. Guo, C. I. Sathish, X. Wang, Y.-H. Yuan, M. Tanaka, and K. Yamaura, “High-Temperature Ferrimagnetism Driven by Lattice Distortion in Double Perovskite $\text{Ca}_2\text{FeOsO}_6$,” *J. Am. Chem. Soc.*, vol. 136, no. 9, pp. 3326–3329, Mar. 2014.
- [33] H. L. Feng, M. Arai, Y. Matsushita, Y. Tsujimoto, Y. Yuan, C. I. Sathish, J. He, M. Tanaka, and K. Yamaura, “High-pressure synthesis, crystal structure and magnetic properties of double perovskite oxide $\text{Ba}_2\text{CuOsO}_6$,” *J. Solid State Chem.*, vol. 217, pp. 9–15, Sep. 2014.
- [34] C. M. Thompson, J. P. Carlo, R. Flacau, T. Aharen, I. A. Leahy, J. R. Pollicemi, T. J. S. Munsie, T. Medina, G. M. Luke, J. Munevar, S. Cheung, T. Goko, Y. J. Uemura, and J. E. Greedan, “Long-range magnetic order in the $5d^2$ double perovskite $\text{Ba}_2\text{CaOsO}_6$: comparison with spin-disordered Ba_2YReO_6 ,” *J. Phys. Condens. Matter*, vol. 26, no. 30, p. 306003, Jul. 2014.
- [35] H. Matsuura and K. Miyake, “Effect of Spin–Orbit Interaction on $(4d)^3$ - and

- (5d)³-Based Transition-Metal Oxides,” *J. Phys. Soc. Jpn.*, vol. 82, no. 7, p. 073703, Jun. 2013.
- [36] A. Prokofiev, A. Sidorenko, K. Hradil, M. Ikeda, R. Svagera, M. Waas, H. Winkler, K. Neumaier, and S. Paschen, “Thermopower enhancement by encapsulating cerium in clathrate cages,” *Nat. Mater.*, vol. 12, no. 12, pp. 1096–1101, Dec. 2013.
- [37] M. Brühwiler, S. M. Kazakov, J. Karpinski, and B. Batlogg, “Mass enhancement, correlations, and strong-coupling superconductivity in the β -pyrochlores KOs_2O_6 ,” *Phys. Rev. B*, vol. 73, no. 9, p. 094518, Mar. 2006.
- [38] Y. Shi, Y. Guo, S. Yu, M. Arai, A. Sato, A. A. Belik, K. Yamaura, and E. Takayama-Muromachi, “Crystal Growth and Structure and Magnetic Properties of the 5d Oxide $\text{Ca}_3\text{LiOsO}_6$: Extended Superexchange Magnetic Interaction in Oxide,” *J. Am. Chem. Soc.*, vol. 132, no. 24, pp. 8474–8483, Jun. 2010.
- [39] M.-H. Whangbo, H.-J. Koo, and D. Dai, “Spin exchange interactions and magnetic structures of extended magnetic solids with localized spins: theoretical descriptions on formal, quantitative and qualitative levels,” *J. Solid State Chem.*, vol. 176, no. 2, pp. 417–481, Dec. 2003.
- [40] J.-W. G. Bos and J. P. Attfield, “Magnetic frustration in $(\text{LaA})\text{CoNbO}_6$ (A=Ca, Sr, and Ba) double perovskite,” *Phys. Rev. B*, vol. 70, no. 17, p. 174434, Nov. 2004.
- [41] H. Watanabe, T. Shirakawa, and S. Yunoki, “Microscopic Study of a Spin-Orbit-Induced Mott Insulator in Ir Oxides,” *Phys. Rev. Lett.*, vol. 105, no. 21, p. 216410, Nov. 2010.
- [42] G. Jackeli and G. Khaliullin, “Mott Insulators in the Strong Spin-Orbit Coupling Limit: From Heisenberg to a Quantum Compass and Kitaev Models,” *Phys. Rev. Lett.*, vol. 102, no. 1, p. 017205, Jan. 2009.
- [43] B. J. Kim, H. Ohsumi, T. Komesu, S. Sakai, T. Morita, H. Takagi, and T. Arima, “Phase-Sensitive Observation of a Spin-Orbital Mott State in Sr_2IrO_4 ,” *Science*, vol. 323, no. 5919, pp. 1329–1332, Mar. 2009.
- [44] A. Shitade, H. Katsura, J. Kuneš, X.-L. Qi, S.-C. Zhang, and N. Nagaosa,

- “Quantum Spin Hall Effect in a Transition Metal Oxide Na_2IrO_3 ,” *Phys. Rev. Lett.*, vol. 102, no. 25, p. 256403, Jun. 2009.
- [45] Y. Singh and P. Gegenwart, “Antiferromagnetic Mott insulating state in single crystals of the honeycomb lattice material Na_2IrO_3 ,” *Phys. Rev. B*, vol. 82, no. 6, p. 064412, Aug. 2010.
- [46] A. Hjelm, C. G. Granqvist, and J. M. Wills, “Electronic structure and optical properties of WO_3 , LiWO_3 , NaWO_3 , HWO_3 , H_2WO_3 , and WO_3 ,” *Phys. Rev. B*, vol. 54, no. 4, pp. 2436–2445, Jul. 1996.
- [47] S. J. Moon, H. Jin, K. W. Kim, W. S. Choi, Y. S. Lee, J. Yu, G. Cao, A. Sumi, H. Funakubo, C. Bernhard, and T. W. Noh, “Dimensionality-Controlled Insulator-Metal Transition and Correlated Metallic State in $5d$ Transition Metal Oxides $\text{S}_{m+1}\text{Ir}_n\text{O}_{3n+1}$ ($n=1, 2$, and ∞),” *Phys. Rev. Lett.*, vol. 101, no. 22, p. 226402, Nov. 2008.
- [48] Y. Shi, Y. Guo, Y. Shirako, W. Yi, X. Wang, A. A. Belik, Y. Matsushita, H. L. Feng, Y. Tsujimoto, M. Arai, N. Wang, M. Akaogi, and K. Yamaura, “High-Pressure Synthesis of $5d$ Cubic Perovskite BaOsO_3 at 17 GPa: Ferromagnetic Evolution over $3d$ to $5d$ Series,” *J. Am. Chem. Soc.*, vol. 135, no. 44, pp. 16507–16516, Nov. 2013.

Chapter 5 Crystal structures, and magnetic properties of double-perovskite oxides $\text{Ca}_2\text{NiIrO}_6$

5.1 Iridium oxides containing Ir^{6+}

In recent years, the mixed oxides containing $5d$ transition metal elements have been drawing many attentions. Due to the increased spatial extent of $5d$ orbital, these materials presented unusual electronic structures and exhibited interesting electronic and magnetic properties [1]. Recently $5d^3$ perovskite LiOsO_3 has been manifested with the ferroelectric-like transition occurring in its metallic state [2]. Besides, $5d^3$ iridium-based perovskite or perovskite-like oxides have rarely been explored, albeit their remarkable physical properties. Among those oxidation states, Ir^{6+} -O bond was the strongest in an oxygen lattice, resulting in the low stability of Ir^{6+} ($[\text{Xe}]4f^{14}5d^3$). Demazeau *et al* reported the first Ir^{6+} contained double perovskite $\text{Sr}_2\text{CaIrO}_6$ and $\text{Sr}_2\text{MgIrO}_6$ [3], [4] The introduction of $3d$ magnetic cation in the B sublattice in a double perovskite could bring about new properties and interesting physical phenomena. In this work, we reported the first successful synthesis of $\text{Ca}_2\text{NiIrO}_6$ via the high pressure and high temperature method. Its crystallographic structure has been clarified with the synchrotron X-ray diffraction data; and its physical properties were revealed from the systematic magnetic, heat capacity and resistivity measurements.

5.2 Experimental details

Polycrystalline $\text{Ca}_2\text{NiIrO}_6$ was synthesized through the solid-state reaction between the powders of CaO (laboratory-made), NiO (laboratory-made), Ir (> 99.9%, Rare Metallic Co. LTD, Japan), and KClO_4 (> 99.5%, Kishida Chemical Laboratory Co., Japan) under high pressure conditions. The stoichiometric mixture of powders ($\text{CaO} : \text{NiO} : \text{Ir} : \text{KClO}_4 = 2:1:1:0.75$) was sealed in the Pt capsule, which was then set into a belt-type high pressure apparatus. The pressure was maintained at 6 GPa along with the heating at 1500 °C for 1 h. Subsequently, the capsule was quenched to ambient temperature within a minute and the pressure was gradually released over a few hours.

Firstly, the X-ray diffraction (XRD) with an X-ray diffractometer of Cu K α radiation was utilized for a brief investigation of the crystallographic structure of the synthesized Ca₂NiIrO₆. Then the more detailed study was carried out by using the synchrotron X-ray diffraction (SXRD) at ambient temperature with the BL15XU beamline facility at SPring-8. The SXRD data was collected with a large Debye-Scherrer-type diffractometer [5], and the “MYTHEN” one-dimensional semiconductor X-ray detector [6]. The radiation wavelength was confirmed to be 0.41003 Å with a reference material, viz. CeO₂. By using the “RIETAN-VENUS” software, the SXRD pattern was analyzed with the Rietveld method introduced in Refs. [7] and [8].

Magnetic susceptibility (χ) was measured in a Magnetic Property Measurement System (MPMS, Quantum Design, Inc). The χ measurements were conducted on a small amount of the powdered compound under field-cooling (FC) and zero-field cooling (ZFC) conditions at 2-375 K, using an applied magnetic field of 10 kOe. Isothermal magnetizations were measured between -70 kOe and 70 kOe, at varied temperatures of 10 K, 35 K and 100 K, respectively.

The electrical resistivity (ρ) measurements were conducted at 100 K - 300 K using a four-point method and with a DC gauge current of 0.1 mA, in a Physical Properties Measurement System (PPMS, Quantum Design, Inc). Electrical contacts were prepared along the longitudinal direction of the specimen by attaching Pt wires with Ag paste. The temperature dependence of specific heat (C_p) was also measured in the PPMS at 2-300 K with the thermal relaxation method. The contribution of KCl to the raw C_p data was subtracted over the studied temperature range using the tabulated data and the mass ratio (0.11418 for 0.75KCl/Ca₂NiOsO₆) [9].

5.3 Crystal structure

The powder XRD pattern in **Fig. 5.1** suggested a double perovskite type crystal structure for the Ca₂NiIrO₆ compound. As results of the monoclinic rock-salt ordered arrangement of Ni and Ir cations in B and B' double perovskite sites combined the tilting of the BO₆ and B'O₆ octahedra [10], the superstructure reflection of (011) peak appeared near $2\theta = 20^\circ$. Crystal structure of Ca₂NiIrO₆ was refined in space group $P2_1/n$. The unit-cell parameters are related

to a_0 (ideal cubic perovskite $a_0 \approx 3.82 \text{ \AA}$) as $a \approx \sqrt{2} a_0$, $b \approx \sqrt{2} a$, $c \approx 2 a_0$, and $\beta \approx 90^\circ$. The results of Rietveld analysis of the SXRD patterns were presented in **Fig. 5.2**. The detailed information was listed in **Table 5.2**. The refined structures are depicted in **Fig. 5.3**.

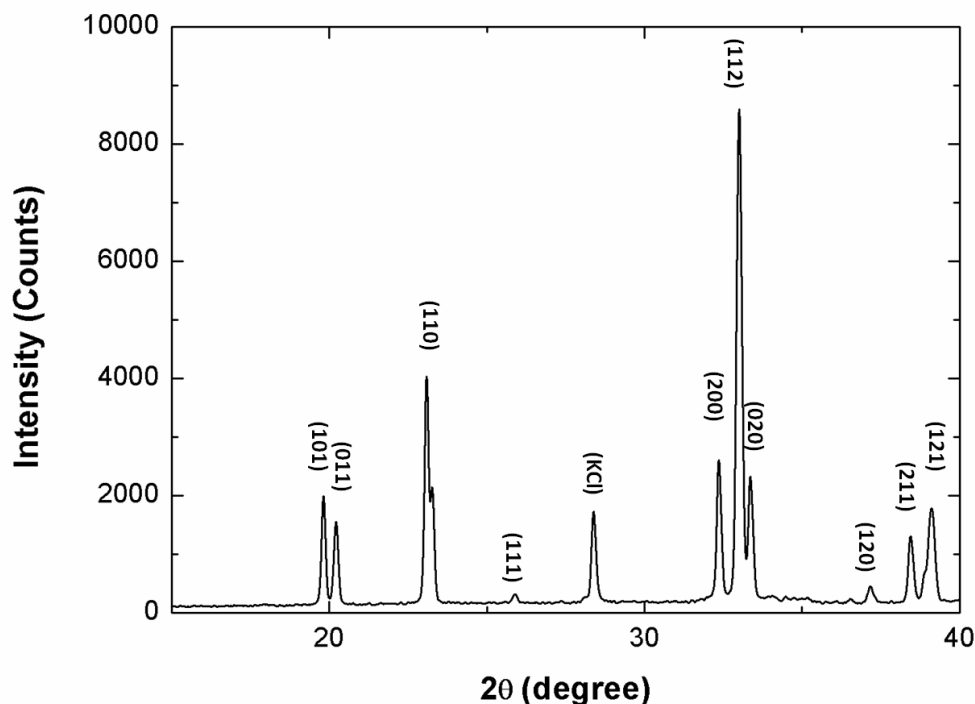


Figure 5.1 Powder XRD (Cu $K\alpha$) patterns for $\text{Ca}_2\text{NiIrO}_6$.

During the refinements, the fit of the SXRD profiles was strongly improved by allowing a small degree of disorder in the Ni vs Ir distribution. Ni and Ir atoms were tentatively assumed to occupy the B' and B'' sites randomly. Therefore, we decided to refine the occupancies of Ni and Ir atoms at the B' and B'' sites. Initially, the displacement parameters for all atoms were fixed at 0.5 \AA^2 ; later, the displacement parameters and occupancies were refined simultaneously. The procedure was repeated until no further improvement could be obtained. It resulted in the percentages of long-range ordering of Ni of 92% and Ir of 95%, respectively (see **Table 5.1**).

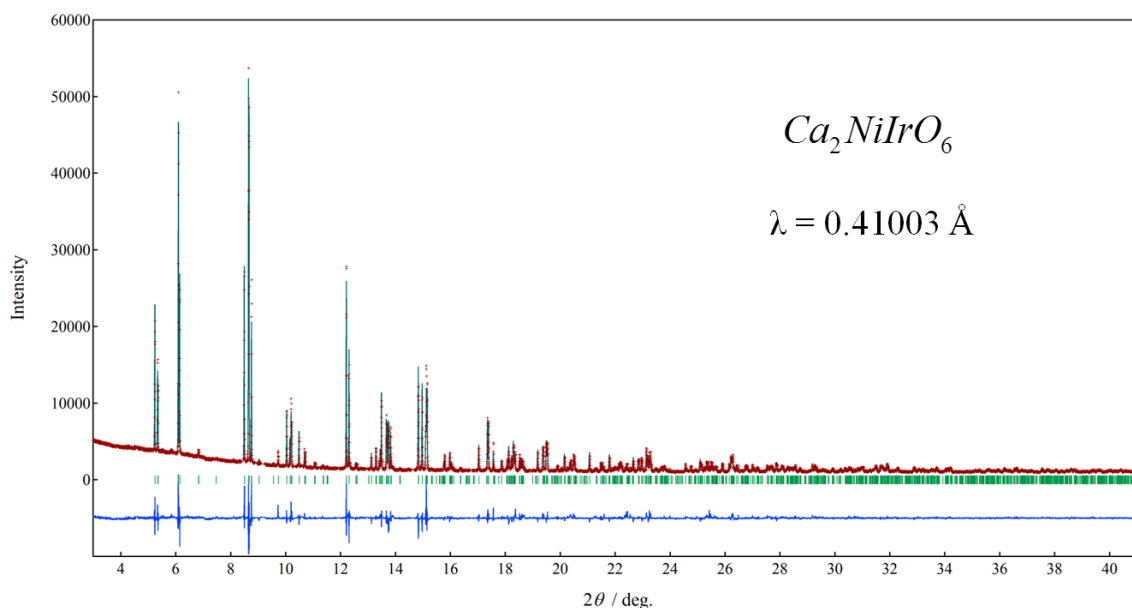


Figure 5.2 Riveted analysis of the SXRD patterns for $\text{Ca}_2\text{NiIrO}_6$ at ambient temperature. Circles and solid lines show the observed and calculated patterns, respectively, and the difference between the patterns is shown at the bottom of each figure. The expected Bragg reflections are marked by the small vertical bars.

Table 5.1 Structural parameters of $\text{Ca}_2\text{NiIrO}_6$ at room temperature.

Atom	Wyckoff Positions	Occupancy	x	y	z	$B(\text{\AA}^2)$
$\text{Ca}_2\text{NiIrO}_6$, Space group $P2_1/n$ (No. 14), $a = 5.3680(9) \text{ \AA}$, $b = 5.5343(1) \text{ \AA}$, $c = 7.6456(2) \text{ \AA}$, $\beta = 90.172(1)^\circ$, $Z = 2$, $V = 227.140(4) \text{ \AA}^3$, and $d_{\text{cal}} = 6.244 \text{ g/cm}^3$, $R_{\text{wp}} = 6.546\%$, $R_{\text{p}} = 4.431\%$						
Ca	4e	1	0.2602(0)	0.0546(1)	0.0084(2)	0.70(6)
Ni1/Ir1	2d	0.91(6)/0.08(4)	0.5	0	0.5	0.37(1)
Ir2/Ni2	2c	0.95(1)/0.04(9)	0	0	0.5	0.20(5)
O1	4e	1	0.1615(2)	0.4844(6)	0.9154(6)	0.26(6)
O2	4e	1	0.3401(5)	0.2923(4)	0.2906(6)	0.26(6)
O3	4e	1	0.7759(2)	0.2047(2)	0.8197(1)	0.26(6)

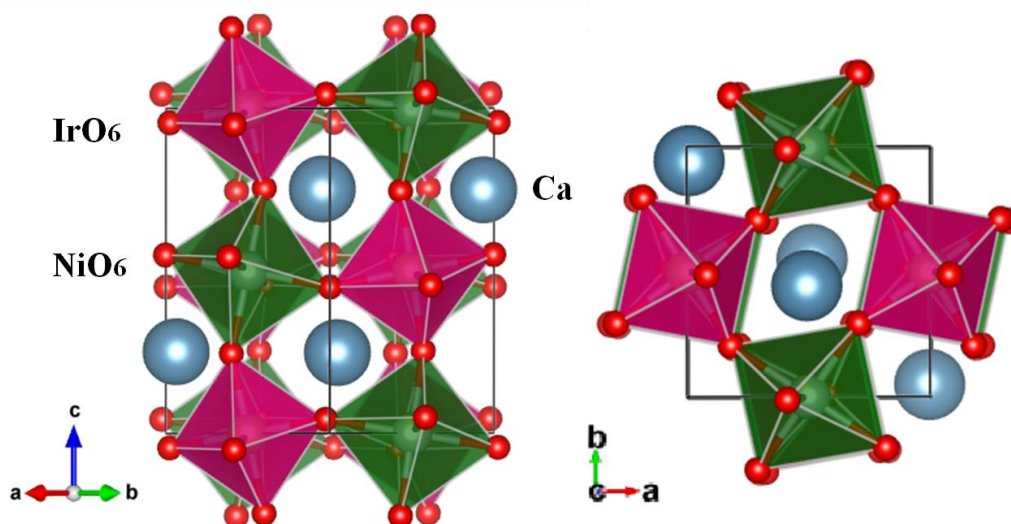


Figure 5.3 Proposed crystal structures of $\text{Ca}_2\text{NiIrO}_6$, in which IrO_6 and NiO_6 are drawn as octahedra (see labels in the figure). Ca atoms are drawn as large spheres as marked.

Pertinent bond lengths (l) of $\text{Ca}_2\text{NiIrO}_6$ were presented in **Table 5.2**; the average Ni–O distance was 2.028(3) Å. The average of $\langle\text{Ni-O}\rangle$ distances were comparable to those of Ni-containing perovskites (2.03 Å for Ni^{2+} in $\text{Sr}_2\text{Ni}(\text{Mo}, \text{Re}, \text{U}, \text{Os})\text{O}_6$ [11]–[14], 2.06 Å for Ni^{2+} in $\text{Ca}_2\text{NiOsO}_6$ [10], and 1.93–1.96 Å Ni^{3+} in RNiO_3 [15]), confirming the presence of both Ni^{2+} and Ni^{3+} cations. Indeed, the bond-valence sum (BVS) of Ni in $\text{Ca}_2\text{NiIrO}_6$ was 2.19, in a reasonable agreement with the mixture of Ni^{2+} and Ni^{3+} . The Ca atoms were also evaluated to be divalent by BVS calculations (see **Table 5.2**). Therefore, the reasonable assumptions of Ir cations were Ir^{6+} and Ir^{5+} , which satisfied the total charge valence of each compound. The typical lengths for octahedra were 1.95–1.99 Å for Ir^{5+} and 1.90–1.95 Å for Ir^{6+} , respectively [3], [16], [17]. The average $\langle\text{Ir-O}\rangle$ distance for $\text{Ca}_2\text{NiIrO}_6$ was 1.946(8) Å, which was similar to the previously reported values of the compounds containing Ir^{6+} . Moreover, $\text{Ca}_2\text{NiIrO}_6$ exhibited the larger average $\langle\text{Ni-O}\rangle$ bond length and the shorter average $\langle\text{Ir-O}\rangle$ bond length, compared with those in $\text{Sr}_2\text{NiIrO}_6$ (1.99 Å and 1.97 Å) with mixed states of Ir^{6+} and Ir^{5+} [15]. It strongly implied the higher percentage of composition of Ir^{6+} [18], which probably stemmed from the more disordered B-site atoms in $\text{Ca}_2\text{NiIrO}_6$.

In $\text{Ca}_2\text{NiIrO}_6$, the inter-octahedral Ni–O–Ir angles were 152.823(7)°, 151.138(0)°, and 147.838(1)°, respectively. These angles were very different from those in a linear arrangement (180°), indicating that the octahedral connections were buckled to some extent in any directions (**Fig. 5.3**). This corresponded to the $a^-a^-c^+$ Glazer’s notations, where the

superscripts indicated the neighboring layers of octahedral exhibiting the rotation in the same direction (+), or rotation in the opposite (–) directions [19]. The O–Ni–O bond angles were nearly 90°. The same situation was observed for O–Ir–O angles. It suggested that the Ni^{2+/3+} and Ir^{5+/6+} cations were located in a quasi-regular octahedral structure. This result was useful in the later investigation of magnetic properties, since the effective magnetic moment of Ir⁶⁺ can be treated as spin-only value when they were at the centre of ideal octahedra.

Table 5.2 Selected interatomic distances and angles in Ca₂NiIrO₆

Bond	Bond distance (Å)	Bond angle(°)
Ni-O1 (x2)	1.997(0)	Ni-O1-Ir =152.823(7)
Ni-O2 (x2)	2.005(3)	Ni-O2-Ir =151.138(0)
Ni-O3 (x2)	2.082(7)	Ni-O3-Ir =147.838(1)
<Ni-O>	2.028(3)	
BVS(Ni)	2.19(3)	O1-Ni-O2 =91.138(1)
Ca-O1 (x4)	3.117(0),3.194(9),2.308(3),2.431(1)	O1-Ni-O3=89.436(6)
Ca-O2 (x4)	2.530(7),3.404(8),2.364(0),2.692(4)	O3-Ni-O2 =93.008(8)
Ca-O3 (x4)	2.330(5),3.437(0),2.650(5),2.614(7)	O1-Ir-O2=91.663(5)
<Ca-O>	2.756(3)	O3-Ir-O1=90.845(4)
BVS(Ca)	2.11(5)	O3-Ir-O2=93.590(6)
Ir-O1 (x2)	1.935(8)	
Ir-O2 (x2)	1.975(4)	
Ir-O3 (x2)	1.929(1)	
<Ir-O>	1.946(8)	
BVS(Ir)	5.41(1)	

Note. B=0.37, R₀(Ni²⁺)=1.654, R₀(Ca²⁺)=1.967, R₀(Ir⁶⁺)=1.908

5.4 Magnetic properties

The temperature dependence of susceptibility (χ) of the polycrystalline Ca₂NiIrO₆ was plotted as **Fig. 5.4(a)**. The establishment of antiferromagnetic interaction at Néel temperature (T_N) was found at ~37 K. A divergence between ZFC and FC curves emerged at the temperatures below 37K; this was ascribed to the magnetic irreversibility, possibly originated from the magnetic frustration or canting of the spins (lattice disorder). Since C_p measurements (shown later) did not show any transition entropy (ΔS) in the vicinity near 37 K, the long-range antiferromagnetic ordering was unlikely to be responsible for the observed cusp in Ca₂NiIrO₆. Fitting the high-temperature χ ($215 \text{ K} \leq T \leq 350 \text{ K}$) to the Curie-Weiss law, $\chi(T) = N_A \mu_{\text{eff}}^2 / [3k_B(T - \Theta_W)]$ (where N_A is the Avogadro constant, k_B is the Boltzmann constant, Θ_W is

the Weiss temperature, and μ_{eff} is the effective Bohr magneton), results in values of the experimental paramagnetic moment $\mu_{\text{eff}} = 4.41\mu_B$ and Weiss temperature $\Theta_W = -352.5$ K. It verifies the presence of antiferromagnetic interactions in the compound. For $\text{Ca}_2\text{NiIrO}_6$, where both iridium and nickel served as magnetic cations, the theoretical effective magnetic moment could be estimated by using the relation $\mu_{\text{spin-only}} = (\mu_{\text{Ni(II)}}^2 + \mu_{\text{Ir(VI)}}^2)^{1/2} = (2.83^2 + 3.87^2)^{1/2} = 4.79\mu_B$. It showed a good agreement with the experimental result.

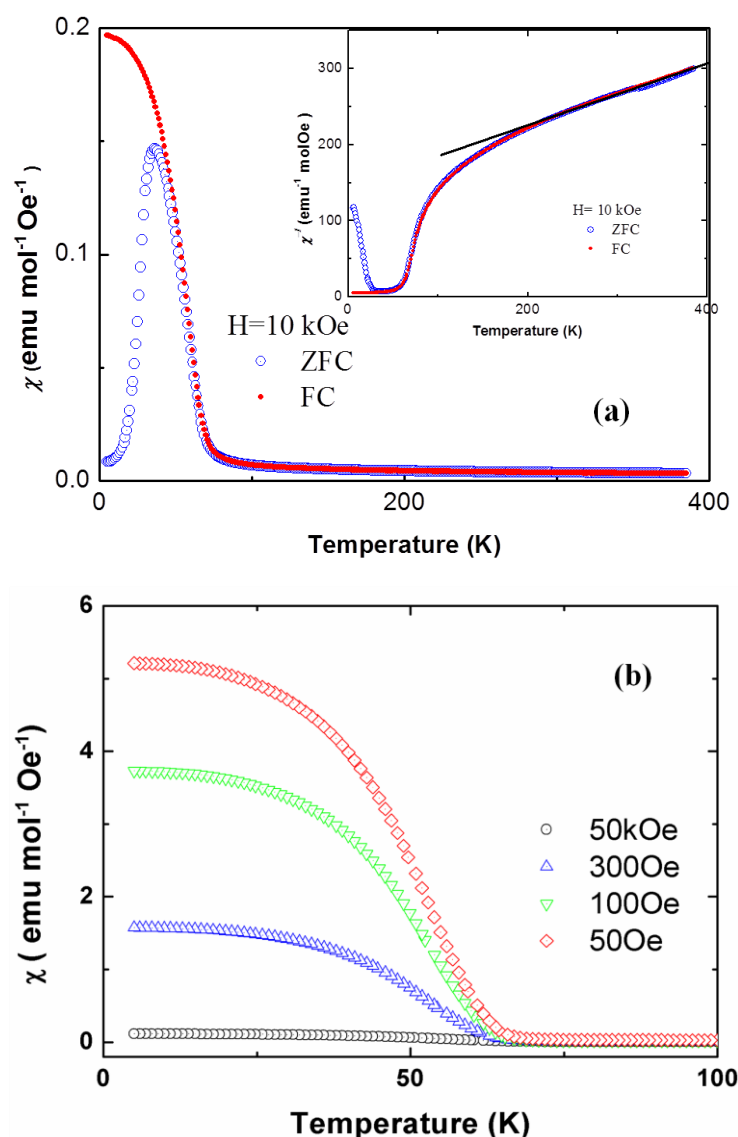


Figure 5.4 (a) Temperature dependence of χ of polycrystalline $\text{Ca}_2\text{NiIrO}_6$ measured in a magnetic field of 10 kOe. Solid and open symbols denote FC and ZFC processes, respectively. The inset shows reciprocal χ vs. temperature for the compounds, and fit lines of the Curie–Weiss law (solid line) above 215K. (b) Temperature dependence of χ at different fields

However, the susceptibility χ started growing with decreased temperatures at $T < 75\text{K}$, which very likely manifested the onset of a very weak ferromagnetic state originated from the spin canting of the antiferromagnetically coupled Ir^{6+} and Ni^{2+} ions. Furthermore, the high dependence of susceptibility χ on the magnetic field below 100 K, as shown in **Fig. 5.4(b)**, further echoed the spin canting.

For the deeper investigation of the magnetic properties of $\text{Ca}_2\text{NiIrO}_6$, magnetization (M) was measured as a function of magnetic field H at various temperatures. The M - H hysteresis loops emerged at 10 K and 35 K, respectively, indicating the weak ferromagnetic characteristics of $\text{Ca}_2\text{NiIrO}_6$ (**Fig. 5.5**). The remanence magnetization and coercive field also increased with decreased temperature, as the higher external field was needed to reverse the stronger magnetic moment at lower temperatures. The saturation magnetization was measured as low as $0.27\mu_{\text{B}}$, revealing the compound as a canted antiferromagnet with a net moment of $0.27\mu_{\text{B}}$. The slight asymmetry was found in these hysteresis loops. It was probably due to that the swept magnetic-field range was unable to cover the entire hysteresis loop. It was interesting to point out that the coercive field was much larger than these of the previously reported canted-antiferromagnetic compounds [14].

The divergence in the FC and ZFC curves at low temperatures suggested the existence of geometrical frustration or canting of the spins (lattice disorder) in the materials. Magnetic frustration was a general phenomenon in antiferromagnetic double perovskite, as a result of the competition between different magnetic interactions. A frustration index f_{frus} , defined as $f_{\text{frus}} = |\Theta_{\text{W}}|/T_{\text{N}}$, measured the degree of frustration in a magnetic materials. The f_{frus} of $\text{Ca}_2\text{NiIrO}_6$ was then calculated as ~ 9.5 . As known that most of geometrically frustrated materials exhibited $f_{\text{frus}} > 10$ [18], it verified the presence of strong magnetic frustration in this compound.

Additionally, we deemed that the local lattice distortion might also lead to the dramatic change of the magnetic properties of $\text{Ca}_2\text{NiIrO}_6$ other than the geometrical frustration. An antiferromagnetic compound $\text{Sr}_2\text{NiOsO}_6$ synthesized previously showed no lattice distortion in its crystal structure [14]. Compared with $\text{Sr}_2\text{NiIrO}_6$, the Ca atoms in $\text{Ca}_2\text{NiIrO}_6$ likely destroyed the lattice environment toward stabilizing a long-range magnetic ordering. The average Ir–O–Ni angle changed from 152.0° (Ca) to 165.6° (Sr), whereas the octahedra Ir^{6+}O_6

was rather solid (the difference between the shortest and longest Ir–O bond length was 2.4% for Ca and 1.8% for Sr) [18]. The degree of buckling of the octahedral connections may have a substantial impact on the changes of the magnetic states. Additional theoretical studies were necessary to reveal the origin of certain magnetic-state changes.

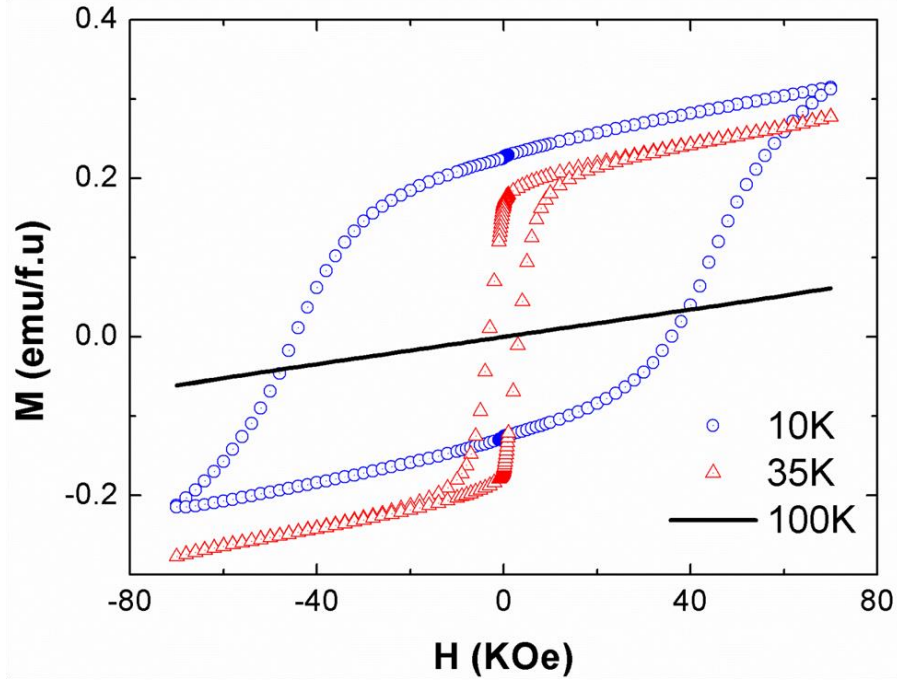


Figure 5.5 Isothermal magnetizations of the polycrystalline $\text{Ca}_2\text{NiIrO}_6$ at 5 K, 35K and 100K, respectively.

5.5 Heat capacity

The heat capacity C_p of $\text{Ca}_2\text{NiIrO}_6$ was measured between 2 K and 300 K; the data was plotted in **Figs. 5.6 (a) and (b)**. In the measurements, no magnetic transition was observed; as C_p monotonically decreased upon cooling to the low-temperature limit. A quantitative analysis of the C_p vs. T curve was conducted by applying the Debye model; however, it poorly fitted to the experimental data. We improved the fitting by adding the Einstein term into the Debye model

$$C_{\text{fit}}(T) = n_D \times 9N_A k_B \left(\frac{T}{T_D}\right)^3 \int_0^{T_D/T} \frac{x^4 e^x}{(e^x - 1)^2} dx + n_E \times 3N_A k_B \left(\frac{T_E}{T}\right)^2 \frac{e^{T_E/T}}{(e^{T_E/T} - 1)^2}$$

where N_A is Avogadro's constant, and T_D and T_E are the Debye and Einstein temperatures, respectively. The scale factors, n_D and n_E , denoted the number of vibrational modes per formula unit in the Debye and Einstein terms, respectively. The goodness of the fit was dramatically improved with the modified model. The fitting yielded the following parameters:

$T_D = 693(9)$ K, $T_E = 144(6)$ K, $n_D = 7.96(1)$ and $n_E = 3.42(7)$. Although the Einstein term was referred to a local phonon mode such as “rattling” in clathrate [20] and beta-pyrochlore oxide [21], the C_p/T^3 vs. T curve (see **Fig. 5.7**) indicated no obvious anomalous local phonon contribution even at temperatures below 20 K. The further investigations of phonon-mode distributions for both compounds were required to uncover the complex nature of the lattices.

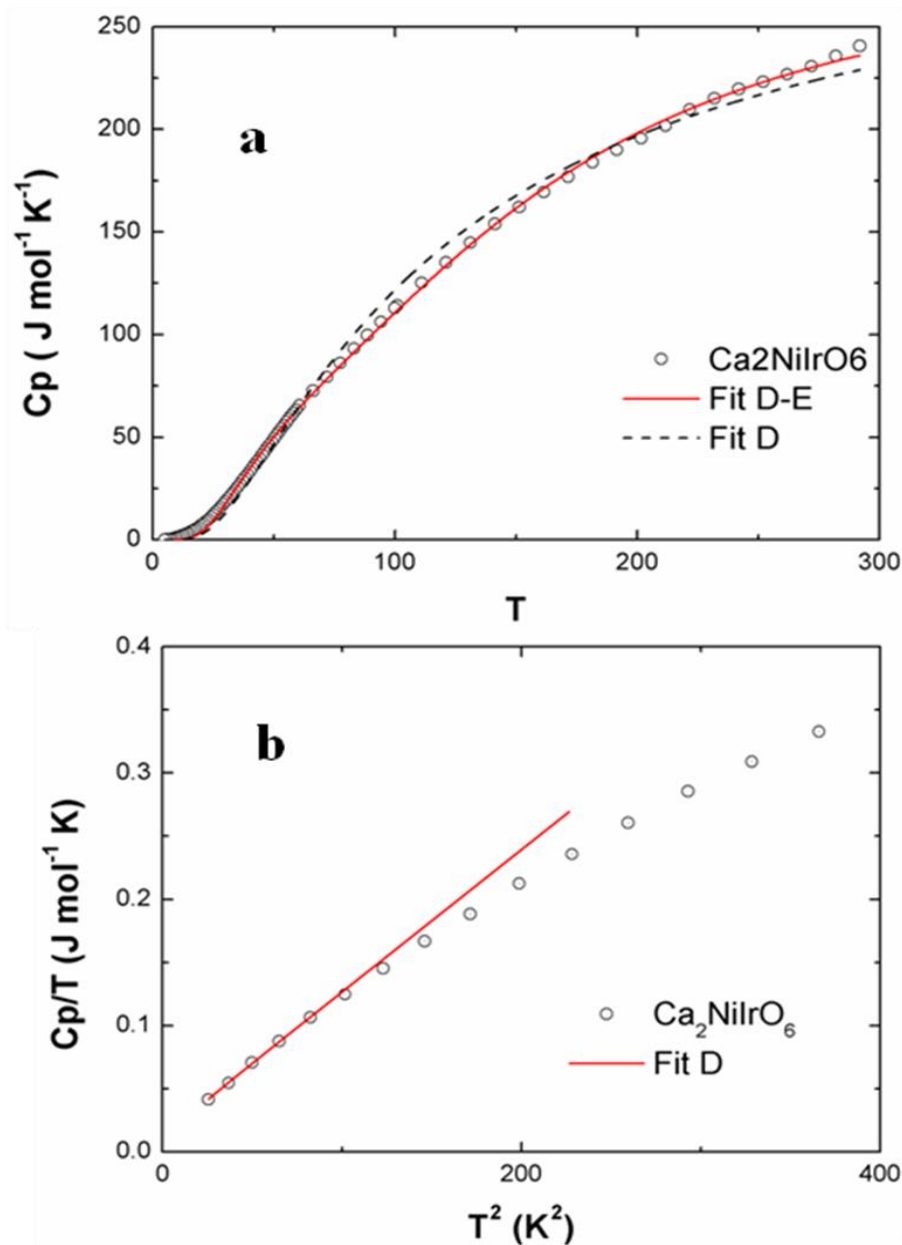


Figure 5.6 (a) Temperature dependence of C_p of $\text{Ca}_2\text{NiIrO}_6$. The solid and dotted curves represent the fits of models to the measured data. (b) The linear fits to the low-temperature part of the C_p/T vs. T^2 curve. The labels D and E indicate the Debye and Einstein models, respectively.

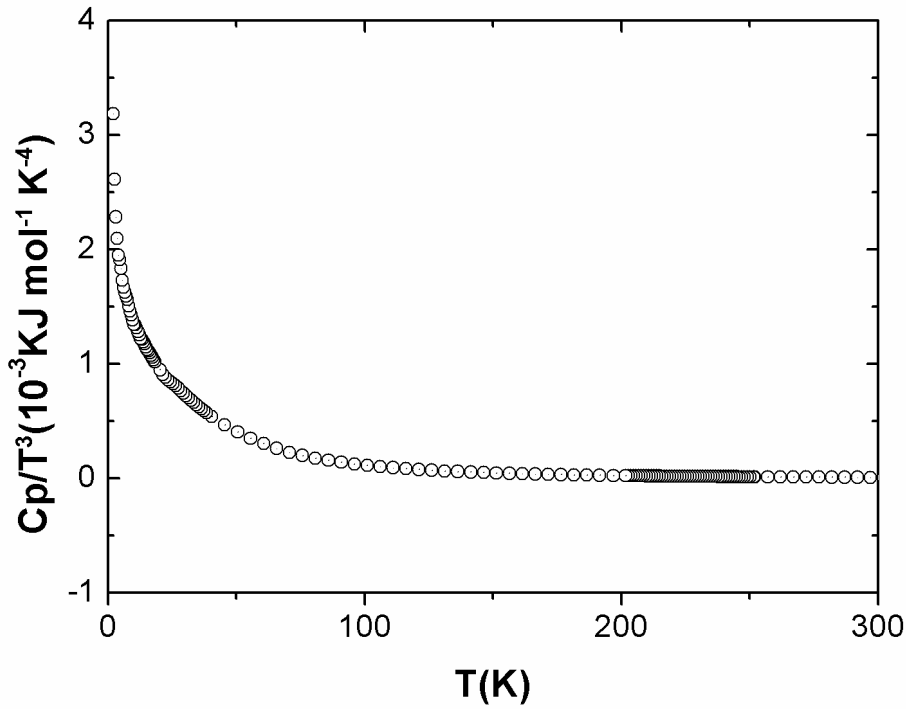


Fig 5.7 Specific heat of $\text{Ca}_2\text{NiIrO}_6$ plotted as C_p/T^3 as a function of temperature.

We analyzed the low-temperature regime ($\ll T_D$) of C_p by applying the approximated Debye model $C_p \approx \gamma T + \beta T^3$, where γ is the electronic specific heat coefficient and β is a constant related to the Debye temperature T_D ($\sim \beta^{-1/3}$). The fitted C_p/T vs. T^2 curve exhibited linearity, showing an accurate approximation. γ and β were fitted to be $6.55(7) \text{ mJ mol}^{-1} \text{ K}^{-2}$ and $1.58(1) \times 10^{-3} \text{ J mol}^{-1} \text{ K}^{-4}$, respectively (**Fig. 5.6 (b)**). With β , T_D was calculated to be $230(8) \text{ K}$. Although the analysis was influenced to some extent by a possible magnetic contribution, the estimation of γ of the compound was almost zero, suggesting a band-gap opening in the electronic state.

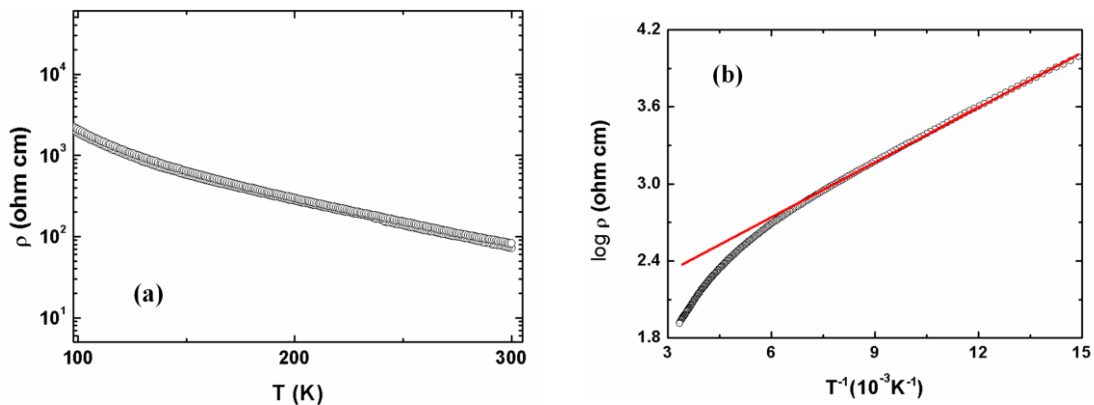


Figure 5.8 (a) Temperature dependence of ρ of polycrystalline $\text{Ca}_2\text{NiIrO}_6$. (b) The Arrhenius plot of the data and its best-fitted line.

5.6 Electronic properties

The temperature dependence of ρ of $\text{Ca}_2\text{NiIrO}_6$ clearly indicated the semiconductor-like behaviors, as depicted in **Fig. 5.8(a)**. The value of ρ at room temperature was $\sim 70 \text{ } \Omega\cdot\text{cm}$; It was three orders of magnitude larger than the expected resistivity of a conducting polycrystalline oxide. Additionally, ρ continuously increased upon cooling and exceeded the instrumental limit at temperatures of 100 K. **Fig. 5.8 (b)** presented the data as a function of the inverse temperature, where a rough linear dependence was identified. Then the fitting of Arrhenius equation to the data gave the activation energy of 0.025(3) eV, which was smaller than those of the similar oxides $\text{Sr}_2\text{FeIrO}_6$ ($\sim 58(1) \text{ eV}$) [16] and $\text{Sr}_2\text{CoIrO}_6$ ($\sim 0.05 \text{ eV}$) [22]. The insulating behavior essentially originated from the absence of an electronic contribution to the low-temperature C_p ; nevertheless, a small amount of KCl residue in the compound may contribute to the conduction slightly.

5.7 Conclusion

The polycrystalline powders of a new double perovskite iridate, $\text{Ca}_2\text{NiIrO}_6$ containing Ni^{2+} and Ir^{6+} have been synthesized. The crystal structure was uncovered by synchrotron powder diffraction. $\text{Ca}_2\text{NiIrO}_6$ exhibited a monoclinic symmetry ($P2_1/n$) and ordered in a canted antiferromagnetic state below 37 K. The dramatic change of its magnetic properties was mainly ascribed to the geometrical frustration and the local lattice distortion. Additional theoretical studies were required to find out the origin of the certain magnetic-state changes.

References in chapter 5

- [1] J. P. Clancy, N. Chen, C. Y. Kim, W. F. Chen, K. W. Plumb, B. C. Jeon, T. W. Noh, and Y.-J. Kim, “Spin-orbit coupling in iridium-based *5d* compounds probed by x-ray absorption spectroscopy,” *Phys. Rev. B*, vol. 86, no. 19, p. 195131, Nov. 2012.
- [2] Y. Shi, Y. Guo, X. Wang, A. J. Princep, D. Khalyavin, P. Manuel, Y. Michiue, A. Sato, K. Tsuda, S. Yu, M. Arai, Y. Shirako, M. Akaogi, N. Wang, K. Yamaura, and A. T. Boothroyd, “A ferroelectric-like structural transition in a metal,” *Nat. Mater.*, vol. 12, no. 11, pp. 1024–1027, Nov. 2013.
- [3] D.-Y. Jung and G. Demazeau, “High Oxygen Pressure and the Preparation of New Iridium (VI) Oxides with Perovskite Structure: $\text{Sr}_2\text{M}\text{IrO}_6$ ($\text{M} = \text{Ca}, \text{Mg}$),” *J. Solid State Chem.*, vol. 115, no. 2, pp. 447–455, Mar. 1995.
- [4] D.-Y. Jung, G. Demazeau, J. Etourneau, and M. A. Subramanian, “Preparation and characterization of new perovskites containing Ir(VI) and Ir(V) [$\text{BaM}_{0.5}\text{OIr}_{0.5}\text{O}_{2.75}$ and $\text{BaM}_{0.25}\text{Ir}_{0.75}\text{O}_3$ ($\text{M} = \text{Li}$ or Na)],” *Mater. Res. Bull.*, vol. 30, no. 1, pp. 113–123, Jan. 1995.
- [5] M. Tanaka, Y. Katsuya, and A. Yamamoto, “A new large radius imaging plate camera for high-resolution and high-throughput synchrotron x-ray powder diffraction by multiexposure method,” *Rev. Sci. Instrum.*, vol. 79, no. 7, p. 075106, Jul. 2008.
- [6] M. Tanaka, Y. Katsuya, Y. Matsushita, and O. Sakata, “Development of a synchrotron powder diffractometer with a one-dimensional X-ray detector for analysis of advanced materials,” *J. Ceram. Soc. Jpn.*, vol. 121, no. 1411, pp. 287–290, 2013.
- [7] K. Momma and F. Izumi, “VESTA: a three-dimensional visualization system for electronic and structural analysis,” *J. Appl. Crystallogr.*, vol. 41, no. 3, pp. 653–658, Jun. 2008.
- [8] F. Izumi and K. Momma, “Three-Dimensional Visualization in Powder Diffraction,” *Solid State Phenom.*, vol. 130, pp. 15–20, 2007.
- [9] Y. S. Touloukian and E. H. Buyco, “Thermophysical Properties of Matter - the TPRC Data Series. Volume 5. Specific Heat - Nonmetallic Solids,” 1970.

- [10] M. T. Anderson, K. B. Greenwood, G. A. Taylor, and K. R. Poeppelmeier, "B-cation arrangements in double perovskites," *Prog. Solid State Chem.*, vol. 22, no. 3, pp. 197–233, 1993.
- [11] M. J. Martínez-Lope, J. A. Alonso, and M. T. Casais, "Synthesis, Crystal and Magnetic Structure of the Double Perovskites A_2NiMoO_6 ($A = Sr, Ba$): A Neutron Diffraction Study," *Eur. J. Inorg. Chem.*, vol. 2003, no. 15, pp. 2839–2844, Aug. 2003.
- [12] M. Retuerto, M. J. Martínez-Lope, M. García-Hernández, M. T. Fernández-Díaz, and J. A. Alonso, "Crystal and Magnetic Structure of Sr_2MReO_6 ($M = Ni, Co, Zn$) Double Perovskites: A Neutron Diffraction Study," *Eur. J. Inorg. Chem.*, vol. 2008, no. 4, pp. 588–595, Feb. 2008.
- [13] R. M. Pinacca, M. C. Viola, J. C. Pedregosa, M. J. Martínez-Lope, R. E. Carbonio, and J. A. Alonso, "Preparation, crystal structure and magnetic behavior of new double perovskites $Sr_2B'UO_6$ with $B'=Mn, Fe, Ni, Zn$," *J. Solid State Chem.*, vol. 180, no. 5, pp. 1582–1589, May 2007.
- [14] R. Macquart, S.-J. Kim, W. R. Gemmill, J. K. Stalick, Y. Lee, T. Vogt, and H.-C. zur Loye, "Synthesis, Structure, and Magnetic Properties of Sr_2NiOsO_6 and Ca_2NiOsO_6 : Two New Osmium-Containing Double Perovskites," *Inorg. Chem.*, vol. 44, no. 26, pp. 9676–9683, Dec. 2005.
- [15] J. A. Alonso, M. J. Martínez-Lope, M. T. Casais, M. A. G. Aranda, and M. T. Fernández-Díaz, "Metal–Insulator Transitions, Structural and Microstructural Evolution of $RNiO_3$ ($R = Sm, Eu, Gd, Dy, Ho, Y$) Perovskites: Evidence for Room-Temperature Charge Disproportionation in Monoclinic $HoNiO_3$ and $YNiO_3$," *J. Am. Chem. Soc.*, vol. 121, no. 20, pp. 4754–4762, May 1999.
- [16] P. D. Battle, G. R. Blake, T. C. Gibb, and J. F. Vente, "Structural Chemistry and Electronic Properties of Sr_2FeIrO_6 ," *J. Solid State Chem.*, vol. 145, no. 2, pp. 541–548, Jul. 1999.
- [17] J.-H. Choy, D.-K. Kim, S.-H. Hwang, G. Demazeau, and D.-Y. Jung, "XANES and EXAFS Studies on the Ir-O Bond Covalency in Ionic Iridium Perovskites," *J. Am. Chem. Soc.*, vol. 117, no. 33, pp. 8557–8566, Aug. 1995.

- [18] P. Kayser, M. J. Martínez-Lope, J. A. Alonso, M. Retuerto, M. Croft, A. Ignatov, and M. T. Fernández-Díaz, “Crystal and Magnetic Structure of $\text{Sr}_2\text{M}\text{IrO}_6$ ($\text{M} = \text{Ca}, \text{Mg}$) Double Perovskites – A Neutron Diffraction Study,” *Eur. J. Inorg. Chem.*, vol. 2014, no. 1, pp. 178–185, Jan. 2014.
- [19] A. M. Glazer, “The classification of tilted octahedra in perovskites,” *Acta Crystallogr. B*, vol. 28, no. 11, pp. 3384–3392, Nov. 1972.
- [20] A. Prokofiev, A. Sidorenko, K. Hradil, M. Ikeda, R. Svagera, M. Waas, H. Winkler, K. Neumaier, and S. Paschen, “Thermopower enhancement by encapsulating cerium in clathrate cages,” *Nat. Mater.*, vol. 12, no. 12, pp. 1096–1101, Dec. 2013.
- [21] M. Brühwiler, S. M. Kazakov, J. Karpinski, and B. Batlogg, “Mass enhancement, correlations, and strong-coupling superconductivity in the β -pyrochlores KOs_2O_6 ,” *Phys. Rev. B*, vol. 73, no. 9, p. 094518, Mar. 2006.
- [22] N. Narayanan, D. Mikhailova, A. Senyshyn, D. M. Trots, R. Laskowski, P. Blaha, K. Schwarz, H. Fuess, and H. Ehrenberg, “Temperature and composition dependence of crystal structures and magnetic and electronic properties of the double perovskites $\text{La}_{2-x}\text{Sr}_x\text{CoIrO}_6$,” *Phys. Rev. B*, vol. 82, no. 2, p. 024403, Jul. 2010.

Chapter 6. General conclusion and future prospects

6.1 General conclusion

In the past few decades, the scientists enjoyed studying the abundant physics of electron correlation in transition metal oxides. During quite long period, *3d* TMOs have taken dominance for studying such strong correlations effects due to a large on-site Coulomb repulsion U (2-10 eV). However, the coulomb repulsions of cations in *5d* TMOs were determined to be less than 1 eV. Besides, *5d* orbitals were spatially much more external than 3d and 4d counterparts. Therefore, it could be excepted *5d* TMOs have a very strong spin orbital coupling, which can compete with other interactions like crystal field. *5d* TMOs' research exactly sparked a great interest of condensed matter physicist to the strong correlated field. In this work, I have concentrated on the crystallography, transport, magnetic and thermodynamic properties of structurally. I synthesized all the perovskite-related oxides by high pressure method, and then characterized them by using XRD, electrical resistivity, and magnetic susceptibility measurements.

So far, a lot of interesting properties have been found in AOsO_3 (A=alkali metals). For example, a perovskite-type oxide, NaOsO_3 , showed a Slater-like transition [1], [2]. Because there was rarely few of cases with Slater-like transition, the discovery of NaOsO_3 was a good example for studying Slater-like transition. The other example was a LiNbO_3 -type oxide, LiOsO_3 . It was the first time for finding a ferroelectric-like transition in the metallic state [3]. For completing a consummate work, KSbO_3 -type crystalline $\text{K}_{0.84}\text{OsO}_3$ was successfully synthesized by high pressure and high temperature method. In addition, $\text{Bi}_{2.93}\text{Os}_3\text{O}_{11}$ was also synthesized and characterized by XRD with KSbO_3 -type structure correctly. Although the formal valence of Os decreased from +5.16 (K) to +4.40 (Bi), both of them showed a weak temperature-dependent

paramagnetic feature and metallic transports. But the resistivity of $\text{Bi}_{2.93}\text{Os}_3\text{O}_{11}$ was temperature independent below 300 K. It was possible due to disorders such as Bi vacancies and the polycrystalline nature of the compounds (including grain boundaries and impurities).

In standard perovskite *5d* TMOs, the singular Mott state was always coexisted with strong spin orbital coupling. Thus, it was necessary to explore double perovskites with single magnetic sublattice for studying singular Mott state. $\text{Ca}_2\text{MgOsO}_6$ and $\text{Sr}_2\text{MgOsO}_6$ have been synthesized in the double perovskite structure. In particular, $\text{Sr}_2\text{MgOsO}_6$ showed a long-range antiferromagnetic transition at ~ 110 K, which the highest T_N among all of *3d*, *4d* and *5d* single magnetic sublattice compounds. But $\text{Ca}_2\text{MgOsO}_6$ did not show any comparable magnetic ordering above 2 K, except for a magnetic cusp at 19 K. The remarkable change in magnetic properties was likely owing to local lattice distortion rather than to the impact of geometrical frustration. Based on the first-principles density functional approach, the double-perovskite oxides $\text{Ca}_2\text{MgOsO}_6$ and $\text{Sr}_2\text{MgOsO}_6$ were likely to be antiferromagnetic Mott insulators, wherein the electronic correlations ($U \sim 1.8\text{-}3.0$ eV) as well as the crystal field had major impacts on opening the gap.

Double perovskites containing Ir^{6+} and Ir^{5+} with formula $\text{Ca}_2\text{NiIrO}_6$ has been synthesized via high pressure method for the first time. It was found that $\text{Ca}_2\text{NiIrO}_6$ crystallizes in a double-perovskite structure (space group $P21/n$) with lattice parameters $a = 5.3680(9)$ Å, $b = 5.5343(1)$ Å, $c = 7.6456(2)$ Å, $\beta = 90.172(1)^\circ$. Magnetic susceptibility measurement indicated that $\text{Ca}_2\text{NiIrO}_6$ orders in a canted antiferromagnetic state at about 37 K. Unusual big coercivity field were found in the hysteresis loop of $\text{Ca}_2\text{NiIrO}_6$ compared with other canted antiferromagnetic *5d* oxides. It was possible due to the anisotropic influence caused by the distortion of Ni/Ir.

6.2 Future prospects

There are still a lot of works to do for perfecting the conclusion got in this thesis. We need to conduct the theoretical calculation to testify the results we got for $\text{Ca}_2\text{NiIrO}_6$. My ongoing studies will be focused on the synthesis of $5d$ oxides, particularly the osmium and iridium oxides, for searching the notable physical phenomena.

$5d$ materials exhibit a great variety of interesting physical properties, many of which are considered to be the result of vigorous competitions between the spin-orbit coupling, Coulomb repulsion and other types of interaction. The properties reported so far include T_c unusual superconductivity, magnetically driven metal-insulator transition (MIT), high T_c ferrimagnetism, the ferroelectric-like transition in metal, geometrically frustrated magnetism, possible topological insulator states and strong magnetic instabilities [1]–[8]. The more exotic anticipated examples are a topological Mott insulator [9], [10]. Thus, the quest is far from complete and many more systems remain to be unveiled and studied. Except for these interesting physical studies, some $5d$ TMOs are the promising candidates for spintronics, memory devices and sensors, such as IrO_2 [11]. In overall, the area of $5d$ transition metal oxides, and osmium and iridium-based compounds in particular, still remains largely unexplored and promises a great deal of exciting discoveries.

References in chapter 6

- [1] S. Calder, V. O. Garlea, D. F. McMorrow, M. D. Lumsden, M. B. Stone, J. C. Lang, J.-W. Kim, J. A. Schlueter, Y. G. Shi, K. Yamaura, Y. S. Sun, Y. Tsujimoto, and A. D. Christianson, “Magnetically Driven Metal-Insulator Transition in NaOsO_3 ,” *Phys. Rev. Lett.*, vol. 108, no. 25, p. 257209, Jun. 2012.
- [2] Y. G. Shi, Y. F. Guo, S. Yu, M. Arai, A. A. Belik, A. Sato, K. Yamaura, E. Takayama-Muromachi, H. F. Tian, H. X. Yang, J. Q. Li, T. Varga, J. F. Mitchell, and S. Okamoto, “Continuous metal-insulator transition of the antiferromagnetic perovskite NaOsO_3 ,” *Phys. Rev. B*, vol. 80, no. 16, p. 161104, Oct. 2009.
- [3] Y. Shi, Y. Guo, X. Wang, A. J. Princep, D. Khalyavin, P. Manuel, Y. Michiue, A. Sato, K. Tsuda, S. Yu, M. Arai, Y. Shirako, M. Akaogi, N. Wang, K. Yamaura, and A. T. Boothroyd, “A ferroelectric-like structural transition in a metal,” *Nat. Mater.*, vol. 12, no. 11, pp. 1024–1027, Nov. 2013.
- [4] Y. Krockenberger, K. Mogare, M. Reehuis, M. Tovar, M. Jansen, G. Vaitheeswaran, V. Kanchana, F. Bultmark, A. Delin, F. Wilhelm, A. Rogalev, A. Winkler, and L. Alff, “ $\text{Sr}_2\text{CrOsO}_6$: End point of a spin-polarized metal-insulator transition by 5d band filling,” *Phys. Rev. B*, vol. 75, no. 2, p. 020404, Jan. 2007.
- [5] Y. Krockenberger, M. Reehuis, M. Tovar, K. Mogare, M. Jansen, and L. Alff, “A neutron scattering study of the crystal and magnetic structure of,” *J. Magn. Magn. Mater.*, vol. 310, no. 2, Part 2, pp. 1854–1856, Mar. 2007.
- [6] S. Yonezawa, Y. Muraoka, Y. Matsushita, and Z. Hiroi, “New Pyrochlore Oxide Superconductor RbOs_2O_6 ,” *J. Phys. Soc. Jpn.*, vol. 73, no. 4, pp. 819–821, Apr. 2004.
- [7] S. Yonezawa, Y. Muraoka, Y. Matsushita, and Z. Hiroi, “Superconductivity in a pyrochlore-related oxide KO_2O_6 ,” *J. Phys. Condens. Matter*, vol. 16, pp. L9–L12, Jan. 2004.
- [8] I. L. Vecchio, A. Perucchi, P. Di Pietro, O. Limaj, U. Schade, Y. Sun, M. Arai, K.

- Yamaura, and S. Lupi, “Infrared evidence of a Slater metal-insulator transition in NaOsO_3 ,” *Sci. Rep.*, vol. 3, Oct. 2013.
- [9] B.-J. Yang and Y. B. Kim, “Topological insulators and metal-insulator transition in the pyrochlore iridates,” *Phys. Rev. B*, vol. 82, no. 8, p. 085111, Aug. 2010.
- [10] D. Pesin and L. Balents, “Mott physics and band topology in materials with strong spin-orbit interaction,” *Nat. Phys.*, vol. 6, no. 5, pp. 376–381, May 2010.
- [11] K. Fujiwara, Y. Fukuma, J. Matsuno, H. Idzuchi, Y. Niimi, Y. Otani, and H. Takagi, “ $5d$ iridium oxide as a material for spin-current detection,” *Nat. Commun.*, vol. 4, Dec. 2013.

List of Publications

This dissertation is based on the following publications.

1. Peer-Reviewed Articles

- 1) **Y. Yuan**, H. L. Feng, M. P. Ghimire, Y. Matsushita, Y. Tsujimoto, J. He, M. Tanaka, Y. Katsuya and K. Yamaura, High-Pressure Synthesis, Crystal Structures, and Magnetic Properties of 5d Double-Perovskite Oxides $\text{Ca}_2\text{MgOsO}_6$ and $\text{Sr}_2\text{MgOsO}_6$, *Inorg. Chem.* **54** (7), 3422-3431 (2015)
- 2) **Y. Yuan**, H. L. Feng, Y. Shi, Y. Tsujimoto, A. A. Belik, Y. Matsushita, M. Arai, J. He, M. Tanaka and K. Yamaura, High-Pressure Synthesis Crystal Structure and Magnetic Properties of KSbO_3 -type 5d Oxides $\text{K}_{0.84}\text{OsO}_3$ and $\text{Bi}_{2.93}\text{Os}_3\text{O}_{11}$, *Sci. Tech. Adv. Mat.* **15** (6), 064901-1 (2014)

2. Presentations

- 1) **Y. Yuan et al.**, “High-Pressure Synthesis, Crystal Structures, and Magnetic Properties of 5d Double-Perovskite Oxides $\text{Ca}_2\text{MgOsO}_6$ and $\text{Sr}_2\text{MgOsO}_6$ ”. Physical Society of Japan Autumn Meeting, September 21st-24th, 2015, Waseda University Campus, Japan.
- 2) **Y. Yuan**, H. L. Feng, Y. Shi, Y. Tsujimoto, A. A. Belik, Y. Matsushita, M. Arai, J. He, M. Tanaka and K. Yamaura, “High Pressure Synthesis, Crystal Structure, and Magnetic Properties of the KO_3 ”, 2014 Mott Physics Beyond the Heisenberg Model, September 16th -18th, Oxford, UK
- 3) **Y. Yuan et al.**, “High-pressure synthesis crystal structure and magnetic properties of KSbO_3 -type 5d oxides $\text{K}_{0.84}\text{OsO}_3$ and $\text{Bi}_{2.93}\text{Os}_3\text{O}_{11}$ ”. Challenges in Advanced Chemistry of Asia 2013 Hokkaido University–Nanjing University Joint Symposium, October 11st-13nd, 2013, Anhui, China.

Publications not included in this dissertation

1. Peer-Reviewed Articles

- 1) J. Li, M. Ji, T. Schwarz, X. Ke, G. Van Tendeloo, J. Yuan, P. J. Pereira, Y. Huang, G. Zhang, H. L. Feng, **Y. Yuan**, T. Hatano, R. Kleiner, D. Koelle, L. F. Chibotaru, K.

- Yamaura, H.-B. Wang, P. Wu, E. T. Muromachi, J. Vanacken, and V. V. Moshchalkov, Local Destruction of Superconductivity by Nonmagnetic Impurities in Mesoscopic Iron-Based Superconductors, *Nature Communications* **6**, 7614 (2015)
- 2) J. Li, J. Yuan, J. Ge, M. Ji, H.-L. Feng, **Y. Yuan**, T. Hatano, J. Vanacken, K. Yamaura, H.-B. Wang, E. T. Muromachi and V. V. Moshchalkov, Depairing Current Density of $\text{Ba}_{0.5}\text{K}_{0.5}\text{Fe}_{1.95}\text{Co}_{0.05}\text{As}_2$ Microbridges with Nanoscale Thickness, *Physica C* **503**, 101-104 (2014)
- 3) J. Li, J. Yuan, M. Ji, G. Zhang, J. Ge, H. L. Feng, **Y. Yuan**, T. Hatano, W. Hu, K. Jin, T. Schwarz, R. Kleiner, D. Koelle, K. Yamaura, H.-B. Wang, P.-H. Wu, E. T. Muromachi, J. Vanacken, V. V. Moshchalkov, Impurity Effects on the Normal-State Transport Properties of $\text{Ba}_{0.5}\text{K}_{0.5}\text{Fe}_2\text{As}_2$ Superconductors, *Physical Review B* **90**, 024512 (2014)
- 4) H.-L. Feng, M. Arai, Y. Matsushita, Y. Tsujimoto, **Y. Yuan**, C. I. Sathish, J. He, M. Tanaka, K. Yamaural, High-Pressure Synthesis, Crystal Structure and Magnetic Properties of Double Perovskite Oxide $\text{Ba}_2\text{CuOsO}_6$, *Journal of Solid State Chemistry* **05**, 217 (2014)
- 5) H.-L. Feng, M. Arai, Y. Matsushita, Y. Tsujimoto, Y. Guo, C. I. Sathish, X. Wang, Y. Yuan, M. Tanaka, K. Yamaura, High-Temperature Ferrimagnetism Driven by Lattice Distortion in Double Perovskite $\text{Ca}_2\text{FeOsO}_6$, *Journal of the American Chemical Society* **136** (9), 33263329 (2014)
- 6) J. Li, J. Yuan, **Y. Yuan**, J. Ge, M. Li, H.-L. Feng, P. J. Pereira, A. Ishii, T. Hatano, A. V. Silhanek, L. F. Chibotaru, J. Vanacken, K. Yamaura, H.-B. Wang, E. T. Muromachi, V. V. Moshchalkov, Direct Observation of the Depairing Current Density in Single-Crystalline $\text{Ba}_{0.5}\text{K}_{0.5}\text{Fe}_2\text{As}_2$ Microbridge with Nanoscale Thickness, *Applied Physics Letters* **103**, 062603 (2012)

2. Presentations

- 1) **Y. Yuan** *et al.*, “Synthesis and Characterization of Whisker Crystals of Fe-Based Superconductor”. Physical Society of Japan Spring Meeting, March 25th-28th, 2013, Tokushima University Campus, Japan.

Acknowledgement

In retrospect, I am very delighted by what I have received throughout the past three years. I have been cultivated the ability to be a person and a scientist. The period of Ph.D. study is the most prized time in my life. I would like to express my heart-felt thankfulness to my research advisors Prof. Eiji Takayama-Muromachi and Prof. Kazunari Yamaura for their educational and financial support, guidance of my research direction and giving me a lot of helps to complete this dissertation work. I also want to thank Prof. Sadamu Takeda, Prof. Makato Wakeshima and Prof. Taro Nagahama for serving as my Ph.D. advisory committee members. I feel truly grateful for their immense professional support, valuable suggestions and thorough corrections to my dissertation.

I wish to acknowledge Dr. Yoshihiro Tsujimoto, Dr. Yoshitaka Matsushita and Dr. Masashi Miyakawa for their helps I received on the high pressure experiment, SXRD measurement and data refinement. I would like to say thanks to Dr. Masao Arai and Dr. Madhav Prasad Ghimire for their theoretical support. I received important trainings from Dr. Jun Li and Dr. Hai Feng on how to use the lab-facilities. Many thanks should also go to previous and present members in my research group: Dr. Youguo Shi, Dr. Yanfeng Guo, Dr. Shan Yu, Ms. Shizuko Miyashita, Dr. Xia Wang, Dr. C. I. Sathish, Mr Jianfeng He and Ms. Yu Su for their helps and supports.

Finally, my heartfelt gratitude is extended to my parents for their encouragement and to my husband, Jian Sun, for his love and support.